

# **Development of a Generally Applicable Machine Learning Potential with Accurate Long-Range Electrostatic Interactions**

Dissertation

for the award of the degree

“Doctor rerum naturalium” (Dr. rer. nat.)

of the Georg-August-Universität Göttingen

within the doctoral program Chemistry

of the Georg-August University School of Science (GAUSS)

submitted by

**Tsz Wai Ko**

from **Guangdong, China**

Göttingen, 2022

## **Thesis Committee**

Prof. Dr. Jörg Behler  
Theoretische Chemie  
Institut für Physikalische Chemie, Georg-August-Universität Göttingen

Prof. Dr. Ricardo A. Mata  
Computerchemie und Biochemie  
Institut für Physikalische Chemie, Georg-August-Universität Göttingen

Prof. Dr. Stefan Goedecker  
Computational Physics  
Department of Physics and Astronomy, University of Basel

## **Members of the Examination Board**

### **Reviewer:**

Prof. Dr. Jörg Behler  
Theoretische Chemie  
Institut für Physikalische Chemie, Georg-August-Universität Göttingen

### **Second Reviewer:**

Prof. Dr. Ricardo A. Mata  
Computerchemie und Biochemie  
Institut für Physikalische Chemie, Georg-August-Universität Göttingen

### **Additional Reviewer:**

Prof. Dr. Dominik Marx  
Lehrstuhl für Theoretische Chemie  
Ruhr-Universität Bochum

## **Further Members of the Examination Board**

Prof. Dr. Dietmar Stalke  
Institut für Anorganische Chemie, Georg-August-Universität Göttingen

Prof. Dr. Peter E. Blöchl  
Angewandte Theoretische Physik  
Institut für Theoretische Physik, Technische Universität Clausthal

Prof. Dr. Burkhard Geil  
Biophysikalische Chemie  
Institut für Physikalische Chemie, Georg-August-Universität Göttingen

Prof. Dr. Bert de Groot  
Computational Biomolecular Dynamics Group  
Max Planck Institute for Biophysical Chemistry

**Date of the oral examination: 23.06.2022**





# Publications

All results in this thesis have been published or are currently in preparation for publication.

## Published papers

(corresponding author=\*, equal contributions=#)

1. **T. W. Ko<sup>\*,#</sup>**, J. A. Finkler<sup>\*,#</sup>, S. Goedecker, and J. Behler. "A Fourth-Generation High-Dimensional Neural Network Potential with Accurate Electrostatics Including Non-Local Charge Transfer". *Nat. Commun.* **12**, 398 (2021)
2. **T. W. Ko<sup>#</sup>**, J. A. Finkler<sup>#</sup>, S. Goedecker<sup>\*</sup>, and J. Behler<sup>\*</sup>. "General-Purpose Machine Learning Potentials Capturing Nonlocal Charge Transfer". *Acc. Chem. Res.* **54**, 808 (2021)
3. E. Kocer<sup>#</sup>, **T. W. Ko<sup>#</sup>**, and J. Behler<sup>\*</sup>. "Neural Network Potentials: A Concise Overview of Methods". *Annu. Rev. Phys. Chem.* **73**, 163 (2022).

## Unpublished papers

1. **T. W. Ko<sup>\*</sup>**, J. A. Finkler, S. Goedecker, and J. Behler. "Accurate Fourth-Generation Machine Learning Potentials by Electrostatic Embedding". **In preparation**



# Acknowledgements

First and foremost, I would like to express the deepest gratitude to my advisor Prof. Dr. Jörg Behler for giving me a golden opportunity to conduct cutting-edge research in the development of machine learning potentials. My research could not have been successful without his enthusiastic encouragement and academic guidance. After finishing my major work, he gave me a great deal of freedom for exploring possible ideas to improve the developed method in the remaining time of my PhD. All these experiences are valuable for me to become an independent and innovative researcher in my academic career.

My sincere gratitude extends to my external advisor Prof. Dr. Stefan Goedecker for his inspiring guidance and advice. I learnt a lot from him on how to think outside the box to address the problems during my PhD studies. I would also like to thank Prof. Dr. Ricardo Mata for his useful comments and suggestions from different angles during thesis committee meetings. Besides, special thanks go to Jonas Finkler for great collaborations and implementations in Ewald Summation and charge equilibration scheme. I enjoyed every discussion we had about the possible improvements of the methods and implementations. Our project could not be completed without his contributions. I would also like to express my gratitude to Dr. Rainer Oswald for his technical support in terms of computers and clusters. I believe I could not finish all calculations very smoothly without his help.

Moreover, I would like to thank my master student Alexander Knoll and internship student Daniel Trzewik for spending their efforts and time into their master thesis and internship report, which gives me a lot of insights for the future development of my project and being a good mentor.

I would like to express my gratitude to the members of the examination board for taking their time to read my thesis and to attend my oral defense as examiners. I also thank Dr. Thorsten Teuteberg for sharing the LaTeX template of the PhD thesis that forms the basic structure of the current document.

Last but not least, I would like to acknowledge my warmest group mates and friends Dr. Martín Paleico, Sebastian Wille, Dilshana Rasheeda, Xaiza Aniban, Tlektés Zhanabekova, Martin Liebetrau, Alea Tokita, Moritz Schäfer and others for giving me wonderful personal life in Göttingen.

Final thanks go to my family and girlfriend Tina Ng who have given me endless support and encouragement. I could not finish this thesis without all of you.



# Abstract

Machine learning potentials (MLPs) have become an indispensable tool for large-scale atomistic simulations, due to their accuracy comparable with ab-initio methods at considerably reduced computational cost. The development of MLPs has attracted increasing attention and numerous relevant applications in materials science, physics and chemistry have been reported. Most MLPs up to date are based on the approximation of locality, meaning that only short-range atomic interactions are considered. The total energy of the system can be decomposed into a sum of environment-dependent atomic energies. This approximation works well for the majority of systems and allows the MLPs to describe systems containing thousands of atoms with very high accuracy by just training on configurations of small systems. Moreover, they can incorporate long-range electrostatic interactions by employing fixed charges or more flexible environment-dependent charges. Despite countless encouraging developments of MLPs, they are unable to describe non-local effects arising from long-range charge transfer and multiple charge states. This shortcoming prevents the study of many interesting phenomena such as chemical interactions involving protonation/deprotonation and biological processes. A new generation of MLPs such as charge equilibration via neural network technique (CENT) and Becke population neural network (BpopNN) is now beginning to emerge in an effort to address these long standing challenges. In this thesis, the limitations of conventional MLPs are overcome by introducing a fourth-generation high-dimensional neural network potential (4G-HDNNP), which combines accurate atomic energies with a charge equilibration scheme relying on environment dependent atomic electronegativities. 4G-HDNNP describes the correct global charge distribution of the system, resulting in a markedly improved potential energy surface. The capabilities of the method have been demonstrated for a set of benchmark systems that involves non-local charge transfer, where existing methods fail even at the qualitative level. Finally, an extension of the 4G-HDNNP, namely the electrostatically embedded 4G-HDNNP (ee4G-HDNNP), is proposed to further enhance the description of non-local effects, and the general transferability to different configurations that are not covered in the reference data set. The promising improvements of ee4G-HDNNP compared to the 4G-HDNNP have been shown on a large data set of both neutral and charged sodium chloride clusters with large structural diversity. This novel method is anticipated to become a reliable tool for the study of many complex biological and electrochemical problems, while existing ab-initio methods combined with modern computer technology are still computationally demanding for large-scale atomistic simulations.



# Abbreviations

<b>ACSF</b>	atom-centered symmetry function
<b>AIMNET</b>	atoms-in-molecules network
<b>ANN</b>	atomic neural network
<b>BFGS</b>	Broyden-Fletcher-Goldfarb-Shanno
<b>BOMD</b>	Born-Oppenheimer molecular dynamics
<b>BpopNN</b>	Becke population neural network
<b>CENT</b>	charge equilibration via neural network technique
<b>DFT</b>	density functional theory
<b>DTNN</b>	deep tensor neural network
<b>FFNN</b>	feed-forward neural network
<b>FHI-AIMS</b>	Fritz Haber Institute <i>ab initio</i> molecular simulation
<b>GAP</b>	Gaussian approximation potential
<b>GGA</b>	generalized gradient approximation
<b>HDNNP</b>	high-dimensional neural network potential
<b>KS</b>	Kohn-Sham
<b>LCAO</b>	linear combination of atomic orbitals
<b>LDA</b>	local density approximation
<b>MD</b>	molecular dynamics
<b>ML</b>	machine learning
<b>MLP</b>	machine learning potential

<b>MLWFC</b>	maximally localized Wannier function center
<b>MPNN</b>	message passing neural network
<b>MTP</b>	moment tensor potential
<b>NNP</b>	neural network potential
<b>PBC</b>	periodic boundary conditions
<b>PBE</b>	Perdew-Burke-Ernzerhof
<b>PES</b>	potential energy surface
<b>Qeq</b>	charge equilibration
<b>RMSD</b>	root mean square deviation
<b>RMSE</b>	root mean square error
<b>RuNNer</b>	Runner Neural Network Energy Representation
<b>SCF</b>	self-consistent field
<b>SNAP</b>	spectral neighbor analysis potential
<b>SOAP</b>	smooth overlap of atomic positions
<b>vdW</b>	van der Waals
<b>wACSF</b>	weighted atom-centered symmetry function
<b>XC</b>	exchange-correlation
<b>ZORA</b>	zero-order regular approximation

# Contents

<b>Abstract</b>	<b>I</b>
<b>Abbreviations</b>	<b>III</b>
<b>I Foundations</b>	<b>1</b>
<b>1 Introduction</b>	<b>3</b>
1.1 Hierarchy of Atomistic Simulation Methods . . . . .	3
1.2 Introduction to Machine Learning Potentials . . . . .	5
1.2.1 Overview . . . . .	5
1.2.2 First Generation: Low-Dimensionality . . . . .	6
1.2.3 Second Generation: Short-Range Interactions . . . . .	6
1.2.4 Third Generation: Long-Range Interactions . . . . .	8
1.2.5 Fourth Generation: Non-Local Interactions . . . . .	9
1.3 Outline of the Thesis . . . . .	13
<b>2 Theoretical Background</b>	<b>15</b>
2.1 Density Functional Theory . . . . .	15
2.1.1 Schrödinger Equation . . . . .	15
2.1.2 Electron Density . . . . .	17
2.1.3 Hohenberg-Kohn Theorems . . . . .	17
2.1.4 Kohn-Sham Equations . . . . .	18
2.1.5 Atom-Centered Basis Sets . . . . .	20
2.1.6 Exchange-Correlation Functionals . . . . .	20
2.1.7 Hirshfeld Charge Partitioning Scheme . . . . .	22
2.2 Neural Network Potentials . . . . .	23
2.2.1 Second-Generation HDNNP . . . . .	23
2.2.2 Third-Generation HDNNP . . . . .	29
2.2.3 Charge Equilibration Using Neural Network Technique . . . . .	32
2.2.4 Short Summary . . . . .	35
2.3 Molecular Dynamics Simulations . . . . .	36
2.3.1 Overview . . . . .	36
2.3.2 Born-Oppenheimer Molecular Dynamics . . . . .	37
2.3.3 Classical Molecular Dynamics . . . . .	38

2.3.4	Minima Hopping . . . . .	39
<b>3</b>	<b>Computational Details</b>	<b>43</b>
3.1	Overview . . . . .	43
3.2	Reference Data Generation . . . . .	43
3.3	Construction of Neural Network Potentials . . . . .	45
3.4	Settings of Minima Hopping . . . . .	46
<b>II</b>	<b>Results and Discussion</b>	<b>49</b>
<b>4</b>	<b>Fourth-Generation HDNNP</b>	<b>51</b>
4.1	Method . . . . .	51
4.1.1	Non-Local Long-Range Electrostatic Part . . . . .	51
4.1.2	Short-Range Part . . . . .	60
4.2	Comparisons with Local Methods for Benchmark Systems . . . . .	62
4.2.1	Organic Molecule . . . . .	62
4.2.2	Metal Clusters . . . . .	68
4.2.3	Ionic Fragments . . . . .	72
4.2.4	Gold Dimer on an Oxide Surface . . . . .	76
<b>5</b>	<b>Electrostatically Embedded Fourth-Generation HDNNP</b>	<b>83</b>
5.1	Motivation . . . . .	83
5.2	Method . . . . .	84
5.2.1	Energy and Force Calculations . . . . .	84
5.2.2	Training Stage . . . . .	88
5.3	Comparison of Fourth-Generation MLPs on Sodium Chloride Clusters . . . . .	89
5.3.1	Accuracy of Fourth-Generation MLPs . . . . .	90
5.3.2	A Benchmark for Ionic Clusters . . . . .	92
5.3.3	Structural Analysis and Energetic Ordering of Local Minima . . . . .	94
5.3.4	Transferability to Crystals . . . . .	97
<b>III</b>	<b>Conclusion and Bibliography</b>	<b>101</b>
<b>6</b>	<b>Summary and Perspectives</b>	<b>103</b>
	<b>Bibliography</b>	<b>109</b>
	<b>Appendix</b>	<b>119</b>
A.1	Symmetry Functions Used for Constructing Neural Network Potentials . . . . .	119
A.2	Learning Curves of HDNNPs . . . . .	128
A.3	Two-Body Potentials of Dimers for Sodium Chloride . . . . .	133

Part I

Foundations



# Chapter 1

## Introduction

### 1.1 Hierarchy of Atomistic Simulation Methods

Theoretical chemistry is utilized to understand the nature of atomic interactions by mathematical techniques and physical laws. It plays an important role in supporting experimental results and providing new insights to study complex chemical reactions, where experimental measurements are currently not feasible. Atomic interactions in molecules and bulk materials can be accurately described by solving the Schrödinger equation. However, an analytical solution is only possible for systems containing at most two electrons such as the hydrogen molecule.

Ab-initio methods based on the wavefunction approach, such as CCSD(T) [1], MP2 [2] and others [3–6] have been developed. They provide an accurate description of atomic interactions by numerically solving the Schrödinger equation. However, wavefunction based methods are computationally demanding for modeling more than a hundred atoms, despite the rapid development of modern computer technologies.

An alternative approach to numerically solving the Schrödinger equation is to employ the concept of electron densities instead of wavefunctions. This concept introduces the density functional theory (DFT), which has become a popular method due to its excellent compromise between accuracy and efficiency. DFT is capable of handling systems with several hundred atoms for molecular dynamics [7, 8] and Monte Carlo [9] simulations. Even though DFT has been successfully applied to a wide range of systems, the description of many interesting phenomena in chemistry requires much larger system sizes to be studied.

In order to perform efficient large-scale atomistic simulations, empirical force fields such as the Tersoff potential [10, 11], ReaxFF [12], and many others [13–15], have been proposed in the past few decades. They are based on physical approximations and the potential energy surface (PES) of the system can be expressed as a simple analytical function of atomic positions. Empirical force fields are usually parameterized by a set of

ab-initio calculations or experimental results. Such force fields allow to model systems with more than hundreds of thousands atoms. However, the properties of the system extracted from simulations driven by force fields are often inconsistent with ab-initio methods and experimental results due to their limited accuracy.

The hierarchy of atomistic simulation methods in terms of the accuracy and affordable system size is plotted in Fig. 1.1. There existed a huge gap between empirical force fields and ab-initio methods for several decades. In recent years, another approach for the construction of PESs based on machine learning has been proposed. These machine learning potentials (MLPs) [16–18] are able to bridge the hierarchy of existing atomistic simulation methods in terms of accuracy and accessible system size, as shown in Fig. 1.1.

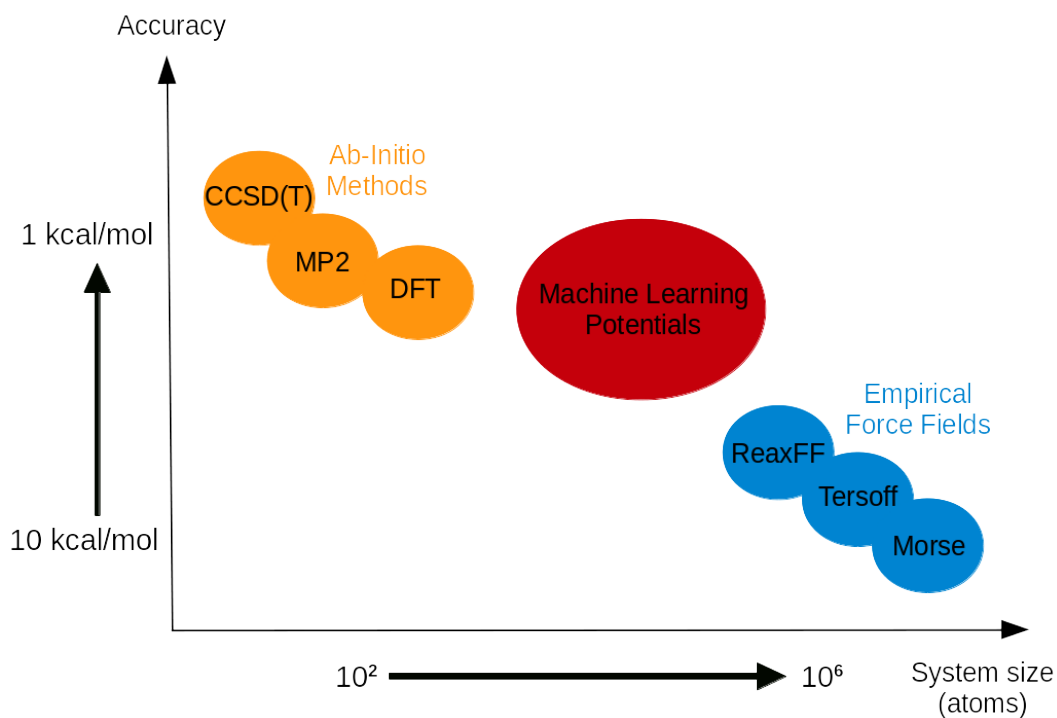


**Fig. 1.1:** Hierarchy of different approaches for performing atomistic simulations in terms of the accuracy and system size. Machine learning potentials have been proposed to bridge the gap between ab-initio methods and empirical force fields that had existed for decades.

## 1.2 Introduction to Machine Learning Potentials

### 1.2.1 Overview

Machine learning (ML) algorithms [19–21] provide accurate predictions after being trained to a set of reference data. They have become indispensable tools in different fields of science that require analysis, classification, or interpolation of data like image recognition and medical diagnosis. Such data-driven sciences are now even being called the 'fourth paradigm of science' together with the other three established paradigms including theoretical models, empirical experimental studies and computer simulations [22].

A particularly encouraging development that has emerged in the past two decades, based on the combination of machine learning and computer simulations, is to represent the high-dimensional PES by MLPs [18, 23–32]. The general idea of MLPs is to use ML techniques to reproduce a PES from reference calculations by establishing a mapping from the atomic positions and possible other physical quantities to the potential energy of the system.

MLPs differ from empirical force fields in several aspects. First, the construction of MLPs usually requires more than thousands of reference data points for the training due to the large number of parameters in the model. Hence, the construction of reference data sets generated from ab-initio methods is computationally demanding. In contrast, the number of data points required for the construction of empirical force fields is significantly reduced because of their simple functional form, which contains only a few parameters to be optimized. However, this also limits the accuracy of force fields. As a consequence, they often predict qualitatively incorrect results compared to ab-initio methods and experiments. On the other hand, MLPs provide a very flexible functional form for fitting the PES of the system, which gives very high accuracy in the regions of configuration space that have been well sampled. Even though the evaluation of energies and forces with MLPs is slightly slower than with empirical force fields, MLPs are still several orders of magnitude faster than electronic structure methods for modelling systems containing thousands of atoms.

Overall, MLPs are considered as an alternative approach for performing large-scale atomistic simulations instead of using empirical force fields, due to their appealing accuracy and efficiency given that the potentials have been constructed properly and validated carefully. This field of research has attracted a great deal of attention and many different types of MLPs have been recently proposed [16, 17, 33].

## 1.2.2 First Generation: Low-Dimensionality

The majority of existing MLPs can be systematically classified into four generations [16, 33, 34]. The first generation of MLPs is only applicable to systems containing few degrees of freedom. Starting with the first model proposed by Doren and coworkers [35] in 1995, they constructed a direct mapping from the atomic positions to the potential energy of the system through a feed-forward neural network. The model was successfully applied to the adsorption of  $\text{H}_2$  on a frozen  $\text{Si}(001)$  surface. In this pioneering work, many technical aspects for the construction of MLPs were investigated and possible improvements for the representation of PESs were also discussed. In the following decade, several groups extended the applicability of neural networks to various molecular systems such as a water dimer [36], vinyl bromide [37], nitrous acid [38] and others [39, 40]. In addition to small molecules, other groups applied neural networks to study gas-surface reactions such as the adsorption of  $\text{O}_2$  on  $\text{Al}(111)$  [41],  $\text{N}_2\text{O}$  on  $\text{Cu}(100)$  [42] and ethanol on  $\text{Au}(111)$  [43].

Besides the applications of MLPs, some progress had been made in methodological development for constructing low-dimensional PESs. For instance, a high-dimensional model representation [44–46] was developed to express the PESs. This representation aims to reduce the dimensionality of PESs by decomposing the total energy into a sum of low-dimensional component functions. Each component function is expressed as a function of few optimized coordinates by a separate neural network. Furthermore, the idea of a many-body expansion was introduced in 2009 for the construction of PESs by using a set of neural networks to express different body terms [47]. In 2013, the permutational invariant polynomials [48] were applied as input coordinates to describe molecules with full permutational invariance to construct a molecular PES by neural networks. Still, this type of descriptors scales factorially with the number of atoms and they are thus only applicable to very small molecular systems [49].

One of the main reasons for the restricted applicability of first-generation MLPs to high-dimensional systems is the lack of generally applicable many-body descriptors that preserve the translational, rotational, and permutational invariance of the total energy. Moreover, these early developed models that directly express the total energy of the system, are not transferable to different system sizes since their architecture is fixed. Finding a solution to address these two problems had become a frustrating challenge in the first decade of MLP development.

## 1.2.3 Second Generation: Short-Range Interactions

Second-generation MLPs overcome the restriction of dimensionality by employing the concept of locality, which works well for the majority of systems. Here it is assumed that a large portion of atomic interactions are attributed to short-range contributions. In 2007, Behler and Parrinello proposed the first MLP of the second generation, namely the

high-dimensional neural network potential (HDNNP or 2G-HDNNP) [50]. The general idea of the model is to decompose the total energy of the system into a sum of all atomic contributions, which is an approximation commonly used in empirical force fields such as the Tersoff [11] and the embedded atom model [51]. Each atomic energy depends on its local chemical environment within a sufficiently large cutoff radius, and is expressed by a set of atomic neural networks (ANNs).

Apart from the definition of atomic energies, Behler and Parrinello also developed a novel type of structural descriptors called atom-centered symmetry functions (ACSFs) [52]. These descriptors are utilized to represent the local atomic environment including exact translational, rotational, and permutational invariances. Hence, the resulting atomic contributions also preserve these invariances. ACSFs have predefined functional forms that contain several parameters controlling the spatial shape of the functions. Based on the combination of the locality approximation and ACSFs descriptors, 2G-HDNNPs can be trained by arbitrary number of atoms and can model systems containing thousands of atoms. 2G-HDNNPs typically reach an accuracy of 1 meV/atom and 0.1 eV/Å in terms of energy and forces. These values define the state-of-the-art accuracy of MLPs.

Other MLPs such as Gaussian approximation potentials (GAPs) [53], spectral neighbor analysis potentials (SNAPs) [54], moment tensor potentials (MTPs) [55] and atomic cluster expansions (ACEs) [56] have been proposed after HDNNPs. All these MLPs also belong to the second generation, since they are capable of modeling thousand of atoms with the state-of-the-art accuracy based on the locality approximation. Moreover, several predefined type structural descriptors for representing the local atomic environments have been developed. Further examples include smooth overlap of atomic positions (SOAPs) [57], the Coulomb matrix [58], and Chebyshev polynomials [59].

More recently, another class of second-generation MLPs has attracted increasing attention. This class of MLPs is based on learning the atomic energies as a function of atomic environments using message passing neural networks (MPNNs) [60]. Instead of using predefined descriptors, the representation of the local chemical environment of each atom is described by an adjustable feature vector, which is iteratively refined by exchanging information with neighboring atoms including their current feature vectors and geometrical information such as bond lengths and angles. The refined atomic feature vectors are then used to predict atomic energies. The range of atomic interactions can in principle be extended by increasing the number of message passing steps.

Various models such as deep tensor neural networks (DTNNs) [61], SchNet [62] and atoms-in-molecules neural networks (AIMNET) [63] are emerging in the field and they also achieve state-of-the-art accuracy for the prediction of energies and forces. Nowadays, second-generation MLPs have become a useful tool for large-scale atomistic simulations in the field of physics, chemistry, and materials science due to their simplicity and efficiency [16, 18].

## 1.2.4 Third Generation: Long-Range Interactions

A crucial limitation of second-generation MLPs is the inability to describe long-range interactions such as electrostatics and dispersion interactions beyond the local atomic environment. Several early attempts have been made to take long-range electrostatic interactions into account based on element-dependent fixed atomic charges for simple force fields [64–67]. This straightforward solution was applied to study gallium nitride and lithium nitride in combination with second-generation MLPs [53, 54]. Still, MLPs that are based on element-specific fixed atomic charges, cannot describe the variability of electrostatic interactions in different chemical environments. For instance, the atomic charges on adsorbate and adsorbant should be different in the case of a metal oxide supported by a slab of its pure metal. Therefore, the development of ML models for the prediction of accurate charges has attracted a great deal of attention.

Starting with the first environment-dependent charges proposed by Popelier and coworkers [68] in 2007, many groups have developed various methods to predict accurate atomic charges and also dipole moments [69–71]. However, only a few MLPs up to date include explicit long-range electrostatic interactions using Coulomb’s law without truncation. Together with environment-dependent atomic energies, they compose the third generation of MLPs. Artrith, Morawietz and Behler [72, 73] proposed the first MLP of the third generation in 2011. They extended the 2G-HDNNP by introducing local environment-dependent charges, which are used to calculate the long-range electrostatic energy and forces.

This third-generation HDNNP (3G-HDNNP) provides a higher flexibility of atomic charges to reliably describe long-range electrostatic interactions and the capabilities of the method have been demonstrated on zinc oxide [72] and the water dimer [73]. In 2018, Tensormol-0.1 [74] was developed to combine the 3G-HDNNP approach with dispersion interactions using Grimme’s D2 method [75]. Instead of reproducing reference atomic charges, the predicted charges in the model are optimized to reproduce dipole moments obtained from reference electronic structure calculations.

Another third-generation MLP based on MPNNs is PhysNet [76], which also includes dispersion interactions using Grimme’s D3 approach [77] and was proposed in 2019. In PhysNet, the atomic feature vectors are repeatedly updated and these refined vectors during every message passing step are also used to determine atomic charges and energies. Notably, the efficiency of the method can be increased by simultaneously predicting both atomic energies and charges based on two different output neurons in the neural networks.

However, only very few applications of third-generation MLPs have been reported for periodic systems due to the fact that long-range electrostatic interactions for the majority of periodic systems are efficiently screened. Furthermore, additional computational time is required for the construction of third-generation MLPs by training another set of machine learning models for the prediction of charges, while the accuracy is just slightly better or comparable to second-generation MLPs.

## 1.2.5 Fourth Generation: Non-Local Interactions

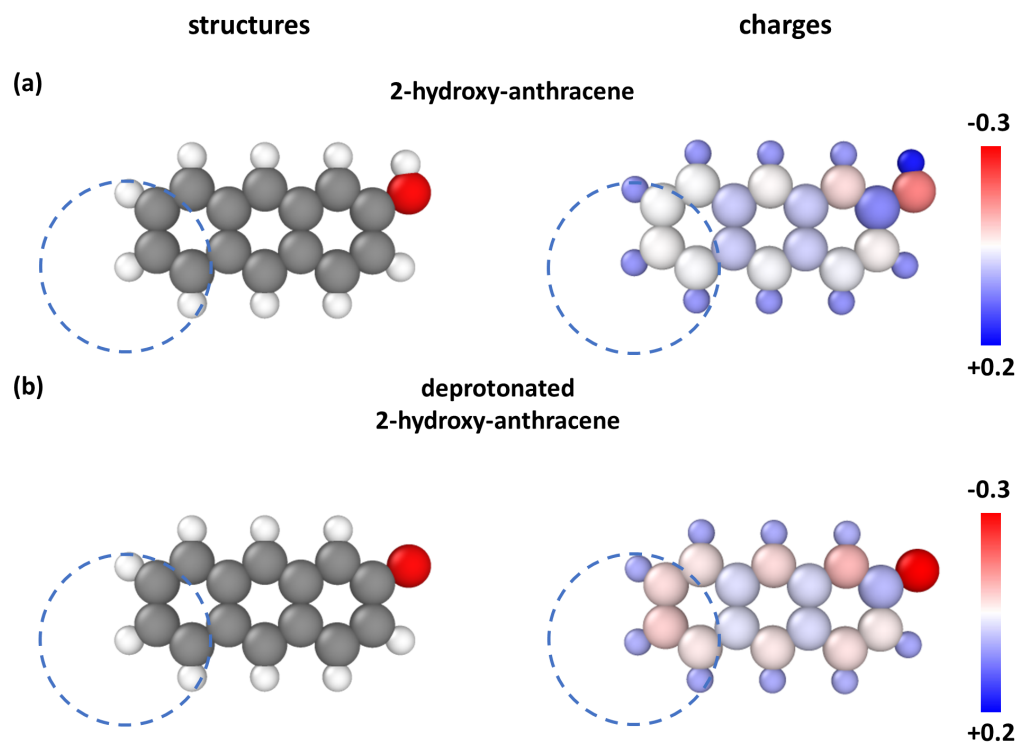


**Fig. 1.2:** Long-range charge transfer in a molecular system. Panel (a) shows the DFT-optimized structure of 2-hydroxy-anthracene. The most distant hydrogen atom is less positively charged as indicated in the plot of DFT Hirshfeld charges on the right side, when the hydroxyl group is deprotonated as shown in panel (b). The local chemical environment of the most distant hydrogen atom indicated as a dashed circle is unchanged and therefore local methods such as second- and third-generation MLPs fail to capture the changes caused by long-range charge transfer. The hydrogen, carbon and oxygen atoms are colored in white, grey and red, respectively. The structural visualization was carried out using Ovito [78]. Reprinted (adapted) with permission from Ref. [79]. Copyright 2021 American Chemical Society.

A remaining limitation of third-generation MLPs is their incapability of describing long-range charge transfer and systems with multiple charge states simultaneously. Long-range charge transfer arises from a global change in the electronic structure of a system by modifying its local chemical environment or total charge. This effect is commonly found in chemistry, materials science, and molecular biology [79–81]. For instance, an

illustrative molecular system for demonstrating long-range charge transfer is displayed in Fig. 1.2. The DFT-optimized structure of the aromatic organic molecule 2-hydroxyanthracene and the corresponding Hirshfeld charges are displayed in panel (a). The global charge distribution of the molecule changes significantly as shown in panel (b) due to the deprotonation of the hydroxyl group. Even the most distant hydrogen atom still experiences long-range charge transfer, despite the electronic change happening far outside the local chemical environment of the hydrogen atom as indicated by the dashed circle. Consequently, second- and third-generation MLPs predict the same atomic energy or charge for both cases due to the identical atomic environment and are thus unable to describe non-local effects arising from the long-range charge transfer.

Another illustrative periodic example, which also exhibits long-range charge transfer, is shown in Fig. 1.3. Panel (a) shows the DFT-optimized structure of a gold atom on a fixed ideal magnesium oxide (001) surface and the corresponding DFT Hirshfeld charges. The favorable adsorption site of a gold atom is on top of an oxygen atom and it is nearly neutral. If a magnesium atom is removed in the bottom layer as displayed in panel (b), the gold atom becomes positively charged and the favorable adsorption site of the gold atom remains the same. Another case is the substitution of an oxygen atom by a fluorine atom in a subsurface layer, which is shown in panel (c). The gold atom becomes heavily negatively charged and the favorable adsorption site changes to a magnesium atom. In all cases, the charge transfers are far beyond the local chemical environment of the gold atom, which is defined by the cutoff sphere indicated as a dashed circle. Again, second- and third-generation MLPs are unable to describe such non-local effects due to the lack of information about the global charge distribution of the system.

The problem of local atomistic PESs, which are unable to capture long-range charge transfer and to describe a system with multiple charge states, has been recognized for a long time. Describing all these non-local effects has led to the development of fourth-generation MLPs. In 2015, the first MLP of the fourth generation was proposed, the charge equilibration via neural network technique (CENT), by Ghasemi and coworkers [82]. The essential idea of CENT is to allow the redistribution of atomic charges over the whole system, relying on the environment dependent electronegativities, according to a charge equilibration (Qeq) scheme [83]. These electronegativities expressed by ANNs, are trained to distribute the partial charges in an optimal way to reproduce the reference total energy of the system. CENT has shown the ability to describe non-local charge transfer and systems with different total charge states. Apart from non-local dependencies, the applications of CENT for the structure prediction of ionic materials has been reported [84, 85]. All these works show that the method provides excellent transferability to periodic systems when just training on the cluster structures.

In 2020, Xie, Persson and Small [86] introduced the Becke population neural network (BpopNN) for modelling systems with different total charges. The expression of the total energy consists of atomic contributions, intra-atomic, and Coulomb electrostatic energy. Here the atomic contributions are expressed as a function of their local environments

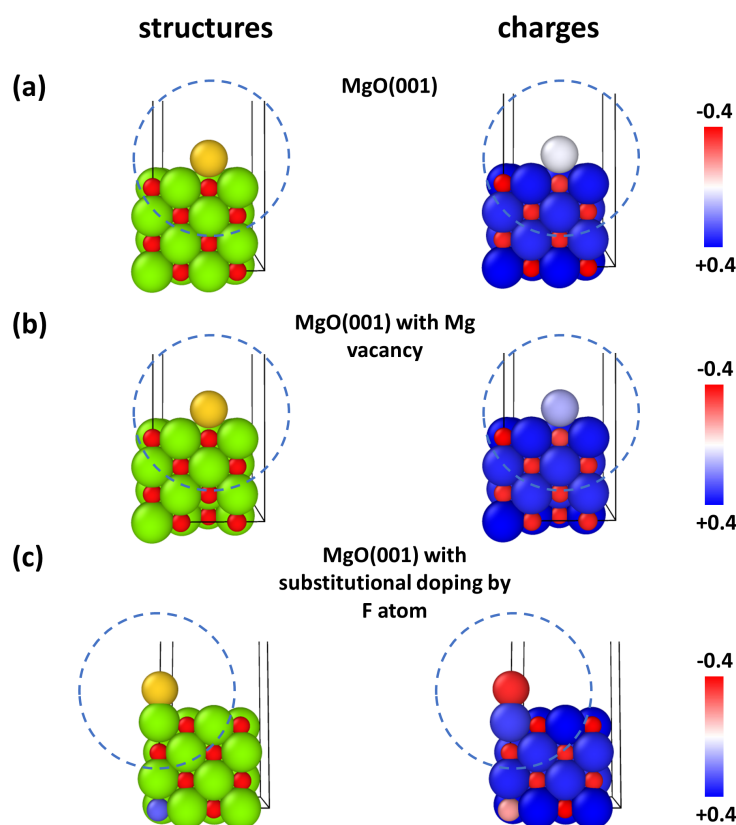


**Fig. 1.3:** Long-range charge transfer in a periodic system. The favourable adsorption site of a gold atom on a fixed ideal magnesium oxide slab (001) predicted by DFT is on top of an oxygen atom as shown in panel (a) and the gold atom is nearly neutral. The gold atom becomes positively charged as indicated in the plot of DFT Hirshfeld charges on the right side, when the vacancy of a magnesium atom is introduced to the bottom layer as displayed in panel (b). If an oxygen atom in the bottom layer of the surface is replaced by a fluorine atom as shown in panel (c), the favourable adsorption site of a gold atom changes to a magnesium atom and the gold becomes heavily negatively charged. The charge transfer in all cases is far beyond the atomic environment of the gold atom as indicated in the dashed circle and are thus unable to be described by local MLPs. The oxygen, fluorine, magnesium, and gold atoms are colored in red, blue, green and yellow, respectively. Reprinted (adapted) with permission from Ref. [79]. Copyright 2021 American Chemical Society.

and atomic populations, i.e. partial charge. This structural and electronic information is transformed into modified SOAP descriptors to predict short-range interactions through ANNs. In the training stage, the initial guess of atomic charges and the corresponding total energy are updated through an iterative SCF-like process.

Despite all these encouraging developments of fourth-generation MLPs, they still have some technical limitations. For instance, the CENT is primarily applicable to ionic systems due to the restricted total energy expression and the overall accuracy is still lower than the state-of-the-art MLPs. In addition, the BpopNN requires an extra SCF-like cycle, which increases the computational costs of energy and force calculations, and this cycle could induce a technical problem regarding the possibility of having multiple or no solutions [86], leading to a problematic energy and force prediction.

More recently, several fourth-generation MLPs based on MPNNs such as SpookyNet [87], AIMNET-NSE [88] and QRNN [89] have been proposed. These models are able to describe long-range charge transfer and multiple charge states by refining the atomic weight factors that determine the redistribution of the charges over the whole system, during the message passing steps. This non-local electronic information is adapted to the atomic feature vectors, which serve as inputs for predicting atomic energies. The ability of these methods to describe non-local effects has been demonstrated for a series of molecular and bulk systems.

The development of fourth-generation MLPs has attracted increasing attention due to their great potential for modeling large systems in electrochemical environments [90], which usually involve long-range charge transfer. In this thesis, a general solution to overcome the limitations of existing MLPs that are based on the locality approximation, is proposed by introducing a fourth-generation HDNNP (4G-HDNNP) [34], which takes the global charge distribution into account. 4G-HDNNP can describe non-local physical effects caused by long-range charge transfer and even changes in the whole electronic structure depending on different total charges of the system. It is generally applicable to ionic and covalent systems without any SCF-like cycle.

The capabilities of the method are revealed in a variety of model systems, which are well studied in chemistry and materials science and involve long-range charge transfer. The 4G-HDNNPs trained to electronic structure calculations can reproduce charges, energies, and forces with excellent accuracy. In contrast, 2G- and 3G-HDNNPs yield inaccurate PESs and they are thus unable to correctly describe these systems. In fact, all MLPs of the second and third generation suffer from the same problem as they are based on the approximation of locality. Finally, possible enhancements of 4G-HDNNP are discussed and a modified framework of the 4G-HDNNP, namely the electrostatically embedded 4G-HDNNP (ee4G-HDNNP), is proposed. The promising improvements of ee4G-HDNNP compared to the 4G-HDNNP are demonstrated on a data set of sodium chloride clusters, which clearly show the ability of the method to provide an accurate description of non-local effects. Furthermore, the ee4G-HDNNP provides excellent transferability to different atomic environments that are not provided in the data set. It is anticipated that the ee4G-HDNNP can be used to study complex electrochemical problems, which require modelling more than thousands of atoms with an accurate description of non-local electronic effects, while ab-initio methods are still impractical.

## 1.3 Outline of the Thesis

This thesis is organized as follows: The hierarchy of atomistic simulation methods and an overview of MLPs are introduced in chapter 1. In chapter 2 the theoretical background is summarized including an overview of DFT and the important features of the 2G-HDNNP, 3G-HDNNP, and CENT, which inspire the framework of the 4G-HDNNP. Both Born-Oppenheimer and classical molecular dynamics including their application to the minima hopping algorithm are also introduced. The computational details for reference data generation, construction of HDNNPs and settings of minima hopping are given in chapter 3. In chapter 4 the framework of 4G-HDNNP is presented and its ability to accurately reproduce ab-initio based PESs for describing non-periodic and periodic benchmark systems is demonstrated, including a detailed comparison to 2G- and 3G-HDNNPs. Further, the ee4G-HDNNP is introduced in chapter 5 and considerable improvements with respect to the 4G-HDNNP on a data set containing both neutral and negatively charged sodium chloride clusters with large structural diversity are also presented. The thesis concludes with a summary and perspectives for the development of 4G-HDNNPs and possible future extensions of the model in chapter 6.



# Chapter 2

## Theoretical Background

### 2.1 Density Functional Theory

Any kind of electronic structure method that provides the total energy, atomic forces and, possibly, the atomic charges for the reference structures can be used to generate a data set for constructing HDNNPs in principle. However, a large number of data points are required to construct the high-dimensional potential energy surface (PES) using neural networks. Hence, the compromise between computational cost and accuracy is a crucial factor for choosing the right electronic structure method.

DFT was chosen to generate reference data in this work because it provides a reliable description of the atomic interactions for a broad range of systems ranging from organic molecules to bulk materials. Furthermore, its efficiency allows to simulate systems containing up to a few hundred atoms. In the following subsections, the theoretical background of DFT is summarized.

#### 2.1.1 Schrödinger Equation

The energies and wavefunctions of non-relativistic quantum mechanical systems can be obtained by solving the time-independent Schrödinger equation for all electrons and nuclei in the system,

$$\hat{H}_{\text{total}}\Psi_{\text{total}}(\{\mathbf{x}_i\}, \{\mathbf{R}_\alpha\}) = E_{\text{total}}\Psi_{\text{total}}(\{\mathbf{x}_i\}, \{\mathbf{R}_\alpha\}) \quad , \quad (2.1)$$

where  $\hat{H}_{\text{total}}$  is the Hamiltonian of the system,  $\Psi_{\text{total}}$  the total wavefunction and  $E_{\text{total}}$  the corresponding total energy. The wavefunction depends on a set of spatial coordinates of the nuclei  $\{\mathbf{R}_\alpha\}$  and the combined spatial  $\{\mathbf{r}_i\}$  and spin coordinates  $\{s_i\}$  of the electrons  $\{\mathbf{x}_i\}$ . Hence, the Schrödinger equation is an eigenvalue problem, where the eigenfunctions are interpreted as wavefunctions of the system and eigenvalues as the allowed total energies. The Hamilton operator encompasses all interactions in the system. It can be

written as the following in atomic units (i.e.,  $m_e = \hbar = e = 1$ ):

$$\begin{aligned}
\hat{H}_{\text{total}} &= \hat{T}_e + \hat{T}_n + \hat{V}_{\text{nn}} + \hat{V}_{\text{ne}} + \hat{V}_{\text{ee}} \\
&= -\sum_{i=1}^{N_{\text{el}}} \frac{1}{2} \nabla_i^2 - \sum_{i=1}^{N_{\text{nuc}}} \frac{1}{2m_i} \nabla_i^2 \\
&\quad + \sum_{i=1}^{N_{\text{nuc}}} \sum_{j>i}^{N_{\text{nuc}}} \frac{Z_i Z_j}{|\mathbf{R}_i - \mathbf{R}_j|} - \sum_{i=1}^{N_{\text{nuc}}} \sum_{j=1}^{N_{\text{el}}} \frac{Z_i}{|\mathbf{r}_i - \mathbf{R}_j|} + \sum_{i=1}^{N_{\text{el}}} \sum_{j>i}^{N_{\text{el}}} \frac{1}{|\mathbf{r}_i - \mathbf{r}_j|} \quad . \quad (2.2)
\end{aligned}$$

The Hamiltonian includes the kinetic energy operators of the nuclei  $\hat{T}_n$  and electrons  $\hat{T}_e$ , the nucleus-nucleus repulsions  $\hat{V}_{\text{nn}}$ , nucleus-electron attractions  $\hat{V}_{\text{ne}}$  and electron-electron interactions  $\hat{V}_{\text{ee}}$ . Here  $\nabla_i^2$  represents the Laplace operator acting on the particle  $i$ .  $Z_i$  and  $m_i$  denote the nuclear charge and atomic mass of nucleus  $i$ , respectively.  $N_{\text{el}}$  and  $N_{\text{nuc}}$  indicate the number of electrons and nuclei in the system.

Solving the Schrödinger equation using the total wavefunction is computationally very demanding since the total number of variables is  $3(N_{\text{el}} + N_{\text{nuc}})$  spatial and  $N_{\text{el}}$  spin coordinates. In 1927, Born and Oppenheimer [91] proposed a physical approximation to reduce the complexity of the problem. It is based on the fact that nuclei are much heavier than electrons. Therefore, the nuclei can be regarded as static on the time scale of the fast moving electrons. Due to the decoupling between the motion of electrons and nuclei, the total wavefunction can be approximated by a product of an electronic wavefunction  $\Psi_e$  and a nuclear wavefunction  $\Psi_n$

$$\Psi_{\text{total}}(\{\mathbf{x}_i\}, \{\mathbf{R}_\alpha\}) \approx \Psi_e(\{\mathbf{x}_i\}, \{\mathbf{R}_\alpha\}) \cdot \Psi_n(\{\mathbf{R}_\alpha\}) \quad . \quad (2.3)$$

As a consequence, the kinetic energy of the nuclei is omitted and their repulsion only exists in the equation as a constant term. The Coulomb interaction between nuclei and electrons is now considered as the external potential  $V_{\text{ext}}$ . The remaining Hamiltonian only acts on the electronic wavefunction. Hence, The electronic energy eigenvalues  $E_e$  can be obtained by solving the following electronic Schrödinger equation:

$$\hat{H}_e \Psi_e = E_e \Psi_e \quad , \quad (2.4)$$

where the electronic Hamiltonian  $\hat{H}_e$  can be expressed as

$$\hat{H}_e = \hat{T}_e + \hat{V}_{\text{ext}} + \hat{V}_{\text{ee}} \quad . \quad (2.5)$$

Consequently, the electronic energy eigenvalue of the electronic wavefunctions  $E_e$  depends parametrically on the nuclear positions. The PES establishes a direct mapping from a set of spatial coordinates of atoms to the potential energy of the system. It can be obtained by varying the positions of the nuclei and repeatedly solving the electronic Schrödinger equation for each chosen atomic configuration. Nowadays, many methods aim to solve the electronic Schrödinger equation numerically and they are referred to as electronic structure methods.

### 2.1.2 Electron Density

Solving the electronic Schrödinger equation with  $4N_{\text{el}}$  degrees of freedom is still very computationally intensive. To further reduce the dimensionality of the problem, the concept of electron density has been proposed for the representation of a many-electron system. It can be written as

$$\rho(\mathbf{r}_1) = N_{\text{el}} \int \dots \int |\Psi_{\text{e}}(\mathbf{x}_1, \dots, \mathbf{x}_{N_{\text{el}}})|^2 ds_1 d\mathbf{x}_2 \dots d\mathbf{x}_{N_{\text{el}}} \quad , \quad (2.6)$$

where  $\rho(\mathbf{r}_1)$  denotes the probability density of finding an electron in the volume element  $d\mathbf{r}_1$  at position  $\mathbf{r}_1$  and the other  $N_{\text{el}} - 1$  electrons elsewhere. This is equal to  $N_{\text{el}}$  times the probability to find one of the electrons at that region since the probability is exactly the same for all indistinguishable electrons. Hence, the electron density only depends on three spatial coordinates, which is much lower than the dimensionality of the wavefunction. Furthermore, the electron density can also provide all necessary information such as the number of electrons and the position of nuclei to construct the electronic Hamiltonian as explained in the next subsection.

### 2.1.3 Hohenberg-Kohn Theorems

In 1964, Hohenberg and Kohn established two theorems [92] to provide the theoretical justification for solving the electronic Schrödinger equation using the electron density instead of the wavefunction. The first theorem states that a one-to-one functional relation exists between the external potential and the electron density. Hence, the external potential, except for a constant, is uniquely determined by the electron density. In this way, the electronic energy of a system can be expressed as a functional of the electron density

$$E[\rho] = E_{\text{kin}}[\rho] + E_{\text{ext}}[\rho] + E_{\text{ee}}[\rho], \quad (2.7)$$

where  $E_{\text{kin}}[\rho]$  and  $E_{\text{ee}}[\rho]$  denote the kinetic energy of the electrons and the electron-electron interaction.  $E_{\text{ext}}[\rho]$  is the interaction with external potential. Notably, the electron-electron interactions can be further decomposed into a sum of the Coulomb interactions  $E_{\text{coul}}[\rho]$  and the non-classical contributions  $E_{\text{ncl}}[\rho]$  including exchange and correlation interactions

$$E_{\text{ee}}[\rho] = E_{\text{coul}}[\rho] + E_{\text{ncl}}[\rho] \quad . \quad (2.8)$$

The second Hohenberg-Kohn theorem indicates that the exact ground state electron density corresponds to the lowest total energy in a many-electron system. Hence, the theorem provides a practical way for optimizing any given electron density  $\rho$  to obtain the ground state electron density  $\rho_0$  and the corresponding energy using the variational principle

$$E[\rho_0(\mathbf{r})] \leq E[\rho(\mathbf{r})] \quad . \quad (2.9)$$

However, an expression for the exact functional dependence of energy and electron density remains unknown.

### 2.1.4 Kohn-Sham Equations

Before the foundations for DFT were established by Hohenberg and Kohn in 1964, Thomas and Fermi [93] already employed the concept of the electron density to calculate the total energy of a system in the late 1920s. Based on the approximation of the uniform electron distribution in an atom, the representation of the kinetic energy expression of the electron density can be deduced directly.

The total energy of the model is expressed as the sum of the Thomas-Fermi kinetic energy functional and two classical terms including the electron-electron and nucleus-electron interactions, which are also represented by the electron density. However, the model provides a very poor description for realistic systems since the predicted energy of a molecule is higher than the sum of its isolated atoms. This is attributed to the unrealistic approximation to the kinetic energy functional term. Apart from that, the lack of exchange and correlation effects of electrons is another source of error.

Kohn and Sham addressed these problems by introducing a fictitious system of non-interacting electrons, which moves within an effective potential  $V_{\text{eff}}$ . For this model system, the kinetic energy can be calculated exactly. The effective potential for the non-interacting system is chosen such that it generates the same density as the system of interacting electrons,

$$\rho_{\text{eff}}(\mathbf{r}) = \sum_{i=1}^{N_{\text{el}}} |\psi_i|^2 = \rho(\mathbf{r}) \quad . \quad (2.10)$$

Here,  $\psi_i$  stands for the Kohn-Sham orbital of a single electron. A set of Kohn-Sham orbitals  $\psi_i$  is determined by solving a set of one-electron Kohn-Sham equations using the Kohn-Sham operator  $\hat{F}^{\text{KS}}$

$$\hat{F}^{\text{KS}} \psi_i = \varepsilon_i \psi_i \quad \text{with} \quad \hat{F}^{\text{KS}} = -\frac{1}{2} \nabla_i^2 + V_{\text{eff}} \quad . \quad (2.11)$$

To derive Eq. 2.11 for a system of fictitious non-interacting electrons, Kohn and Sham split the energy functional into the following contributions:

$$E[\rho] = E_{\text{kin,KS}}[\rho] + E_{\text{coul}}[\rho] + E_{\text{ext}}[\rho] + E_{\text{xc}}[\rho] \quad . \quad (2.12)$$

where the kinetic energy of non-interacting electrons  $E_{\text{kin,KS}}[\rho]$ , the electron-electron

Coulomb interactions  $E_{\text{coul}}[\rho]$ , and the external potential  $E_{\text{ext}}[\rho]$  are written as:

$$\begin{aligned} E_{\text{kin,KS}}[\rho] &= -\frac{1}{2} \sum_{i=1}^{N_{\text{el}}} \langle \psi_i | \nabla_i^2 | \psi_i \rangle \quad , \\ E_{\text{coul}}[\rho] &= \frac{1}{2} \int \int \frac{\rho(\mathbf{r})\rho(\mathbf{r}')}{|\mathbf{r}-\mathbf{r}'|} d\mathbf{r}d\mathbf{r}' \quad , \\ E_{\text{ext}}[\rho] &= \int V_{\text{ext}}\rho(\mathbf{r})d\mathbf{r} \quad , \\ E_{\text{xc}}[\rho] &= (E_{\text{kin}}[\rho] - E_{\text{kin,KS}}[\rho]) + E_{\text{ncl}}[\rho] \quad . \end{aligned}$$

The first three terms in Eq. 2.12 can be computed exactly. The last term is the so-called exchange correlation functional  $E_{\text{xc}}[\rho]$ . It includes the quantum exchange and correlation contributions caused by the electron-electron interaction  $E_{\text{ncl}}[\rho]$  and the difference between the kinetic energy of the interacting and non-interacting electron systems ( $E_{\text{kin}}[\rho] - E_{\text{kin,KS}}[\rho]$ ).

The Eq. 2.12 is then minimized with respect to the Kohn-Sham orbitals  $\psi_i^*$  under the normality constraint of each orbital with the corresponding Lagrange multiplier  $\varepsilon_i$ . The expression of the constrained minimization can be written as:

$$\frac{\delta}{\delta \psi_i^*} \left( E[\rho] - \sum_{i=1}^{N_{\text{el}}} \varepsilon_i \int \psi_i^*(\mathbf{r})\psi_i(\mathbf{r})d\mathbf{r} \right) = 0 \quad (2.13)$$

and finally the Kohn-Sham equations can be derived in the following steps:

$$\begin{aligned} -\frac{1}{2}\nabla_i^2\psi_i + \left( \frac{\delta E_{\text{coul}}}{\delta \rho} + \frac{\delta E_{\text{ext}}}{\delta \rho} + \frac{\delta E_{\text{xc}}}{\delta \rho} \right) \psi_i - \varepsilon_i \psi_i &= 0 \\ \left\{ -\frac{1}{2}\nabla_i^2 + \left( \frac{\delta E_{\text{coul}}}{\delta \rho} + \frac{\delta E_{\text{ext}}}{\delta \rho} + \frac{\delta E_{\text{xc}}}{\delta \rho} \right) \right\} \psi_i &= \varepsilon_i \psi_i \\ \left( -\frac{1}{2}\nabla_i^2 + V_{\text{eff}}(\mathbf{r}) \right) \psi_i &= \varepsilon_i \psi_i \quad . \end{aligned} \quad (2.14)$$

The effective potential  $V_{\text{eff}}$  is expressed as a sum of the functional derivatives with respect to the electron density. A new set of Kohn-Sham orbitals  $\psi_i$  and corresponding orbital energies  $\varepsilon_i$  are then obtained by solving the eigenvalue problem in Eq. 2.14. Finally, the total energy for the system of interacting electrons can be calculated based on the updated electron density obtained from Eq. 2.10:

$$E[\rho] = \sum_{i=1}^{N_{\text{el}}} \varepsilon_i - E_{\text{coul}}[\rho] - \int \frac{\delta E_{\text{xc}}}{\delta \rho} \rho(\mathbf{r})d\mathbf{r} + E_{\text{xc}}[\rho] \quad . \quad (2.15)$$

In this way the ground state energy of the system in the Schrödinger equation can be solved iteratively. The standard procedure for determining the ground state density and

energy is to first initialize the electron density, then construct the Kohn-Sham operators and solve an eigenvalue problem that yields a new electron density. The above steps are repeated until the change of the electron density and the corresponding total energy is lower than the desired tolerance. An iterative procedure like this is called a self-consistent field (SCF) cycle.

## 2.1.5 Atom-Centered Basis Sets

The representation of the Kohn-Sham orbital for a single electron plays an essential role in the efficiency and accuracy of DFT calculations. One particularly advantageous approach to solve the Kohn-Sham equations is based on the linear combination of atomic orbitals, in which the Kohn-Sham orbitals are expressed as a linear combination of atom-centered basis functions (in Dirac notation),

$$\psi_i = \sum_{\mu} c_{i,\mu} |\phi_{\mu}\rangle \quad , \quad (2.16)$$

where  $\phi_{\mu}$  represents a set of basis functions and with the corresponding expansion coefficients  $c_{i,\mu}$ . Substituting this expression into Eq. 2.11 yields

$$\hat{F}^{\text{KS}} \sum_{\mu} c_{i,\mu} |\phi_{\mu}\rangle = \varepsilon_i \sum_{\mu} c_{i,\mu} |\phi_{\mu}\rangle \quad . \quad (2.17)$$

A generalized eigenvalue problem can be established by multiplying an arbitrary basis function  $\langle \phi_{\nu} |$  from the left:

$$\sum_{\mu} c_{i,\mu} \langle \phi_{\nu} | \hat{F}^{\text{KS}} | \phi_{i,\mu} \rangle = \varepsilon_i \sum_{\mu} c_{i,\mu} \langle \phi_{\nu} | \phi_{\mu} \rangle \quad , \quad (2.18)$$

where  $\langle \phi_{\nu} | \hat{F}^{\text{KS}} | \phi_{i,\mu} \rangle$  and  $\langle \phi_{\nu} | \phi_{\mu} \rangle$  are the matrix elements of the Kohn-Sham matrix and overlap matrix, respectively. The size of these two matrices is determined by the number of basis functions. Linear eigenvalue problems like this can then be efficiently solved using highly optimized libraries [94, 95]. In this way, the solution of computationally demanding partial differential equations can be avoided.

## 2.1.6 Exchange-Correlation Functionals

### 2.1.6.1 Overview

The exchange-correlation functional describes all unknown quantities in the Kohn-Sham equations. As a consequence, an accurate approximation of the exchange-correlation

functional is essential for practical applications of DFT. In the past few decades, the development of exchange-correlation functionals has attract a great deal of attention and several approximations have been developed.

In 2001, Perdew and Schmidt [96] presented Jacob's ladder of density functional approximations. It classifies the accuracy of different approximations from no consideration of exchange-correlation effects up to the goal of "chemical accuracy" with an energy accuracy below 1 kcal/mol. Nowadays, generalized gradient approximations (GGAs) are commonly used in DFT due to their appealing compromise between accuracy and computational cost [97, 98].

### 2.1.6.2 Generalized Gradient Approximation

In the very early days of DFT, only the local density approximation (LDA) was used to evaluate the exchange-correlation energy. It is based on the assumption that the density varies slowly and the electron density can thus be approximated by a homogeneous electron gas. Hence, the LDA provides reasonable descriptions for metallic systems where the electron density changes slowly. However, a well known problem of LDA is the overestimation of binding energies. Besides, the LDA only depends on the distribution of the electron density (i.e.,  $\rho(\mathbf{r})$ ), which is insufficient to describe systems with rapidly varying electron densities.

To overcome the limitations of LDA, Langreth and Perdew proposed the GGA for non-uniform electronic systems [99] in 1980. Related works were reported in the following years [100–102]. In the framework of GGA, the gradient of the electron density  $\nabla\rho(\mathbf{r})$  is introduced as an additional variable to approximate the exchange-correlation energy density  $\epsilon_{xc}$ :

$$E_{xc}^{GGA}[\rho(\mathbf{r})] = \int \epsilon_{xc}(\rho(\mathbf{r}), \nabla\rho(\mathbf{r}))\rho(\mathbf{r})d\mathbf{r} \quad . \quad (2.19)$$

The exchange-correlation energy  $E_{xc}^{GGA}[\rho(\mathbf{r})]$  can be further decomposed into exchange and correlation contributions. Different approximations are based on the fitting of highly accurate wavefunction methods [103, 104] for  $E_x^{GGA}$  and  $E_c^{GGA}$ . They show general improvements for describing bulk materials and biological molecules compared to LDA. For instance, Perdew, Burke, and Ernzerhof proposed the PBE functional [105], which is generally applicable to periodic and non-periodic systems. Becke, Lee, Yang and Parr developed the BLYP functional [106, 107] that provides reliable descriptions for organic molecules.

In conclusion, GGAs are considered standard functionals for electronic structure studies in numerous applications. Developments related to the improvement of accuracy of GGAs are expected to continue in the coming years.

### 2.1.7 Hirshfeld Charge Partitioning Scheme

The electron density is not only used to calculate the total energy and atomic forces of a system, but also to investigate charge transfer processes. Its visualization provides useful insight to understand and control chemical interactions [108]. However, direct visualization of the electron density requires a large amount of data storage for all coefficients of basis sets. Hence, it is not feasible for large systems containing thousands of electrons.

To characterize the distribution of the electron density over the whole system efficiently, various charge partitioning schemes have been developed to extract atomic charges from the electronic density. Many schemes such as Mulliken [109] and Löwdin [110] population analysis require the definition of atomic basis functions. However, choosing different basis functions can yield considerably different partial charges on the same atoms [111, 112]. In contrast, the Hirshfeld charge partitioning scheme [113] does not rely on any basis set and it is computationally efficient. Therefore, Hirshfeld charges are employed throughout this work.

Hirshfeld population analysis considers a reference molecule of non-interacting particles, the so-called promolecule. The total electron density of the promolecule at position  $\mathbf{r}$  is then defined as the sum of all free atom densities

$$\rho_{\text{total}}(\mathbf{r}) = \sum_{i=1}^{N_{\text{atoms}}} \rho_i(\mathbf{r}) \quad , \quad (2.20)$$

where  $\rho_i(\mathbf{r})$  represents a spherically averaged ground state free-atom density obtained from DFT calculations. A weight function for each atom that describes their relative share in the promolecule density is expressed as

$$w_i(\mathbf{r}) = \frac{\rho_i(\mathbf{r})}{\sum_{i=1}^{N_{\text{atoms}}} \rho_i(\mathbf{r})} \quad . \quad (2.21)$$

The weight functions are all positive and their sum must be equal to one everywhere. It is noteworthy that the free-atom electron density depends on the choice of functional used in the DFT calculations. The density of the bonded atom  $i$  can be defined in a similar way

$$\rho_i^{\text{bonded}}(\mathbf{r}) = w_i(\mathbf{r})\rho_{\text{mol}}(\mathbf{r}) \quad , \quad (2.22)$$

where  $\rho_{\text{mol}}(\mathbf{r})$  is the actual total electron density of the molecule. The total density is decomposed into all bonded atomic densities according to their respective weight functions. Finally, the partial charge on atom  $i$  is calculated by integrating over the bonded atomic densities and subtracting the nuclear charge  $Z_i$

$$Q_i = Z_i - \int \rho_i^{\text{bonded}}(\mathbf{r})d\mathbf{r} \quad . \quad (2.23)$$

## 2.2 Neural Network Potentials

### 2.2.1 Second-Generation HDNNP

#### 2.2.1.1 Overview

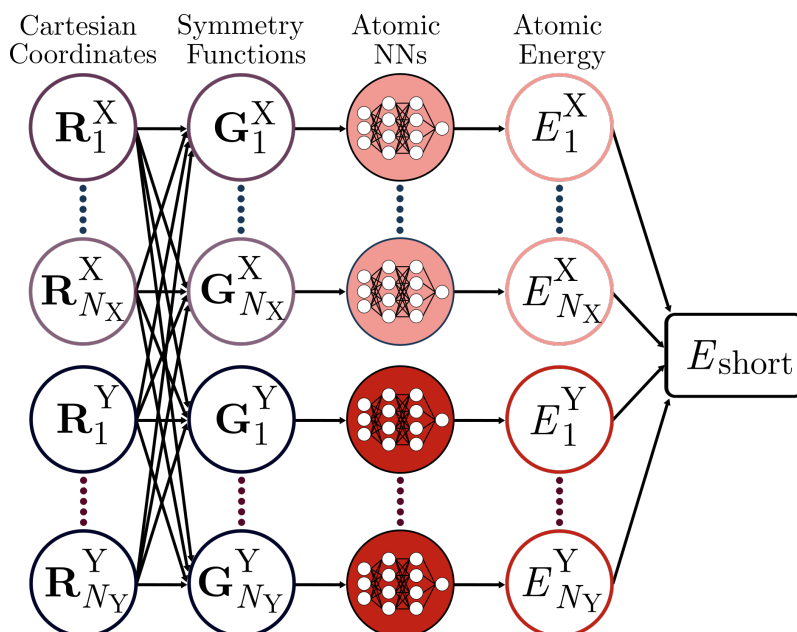


**Fig. 2.1:** Schematic diagram of a 2G-HDNNP for a binary system  $X_{N_X} Y_{N_Y}$ . Two sets of element-specific atomic neural networks are used to predict the atomic energy contribution of the respective elements. Atom-centered symmetry functions  $\{G_i\}$ , which describe the chemical environment within the cutoff sphere based on atomic coordinates, serve as inputs for the atomic neural networks. The sum of all atomic energy contributions  $E_i$  is equal to the short-range energy of the system  $E_{\text{short}}$ , which is equivalent to the total energy of a system based on the approximation of locality. Reprinted (adapted) with permission from Ref. [79]. Copyright 2021 American Chemical Society.

Second-generation high-dimensional neural network potential (2G-HDNNP) [50] is the first MLP, which can efficiently simulate thousands of atoms with excellent accuracy. Fig. 2.1 shows the structure of a 2G-HDNNP for any binary system. 2G-HDNNPs are based on the concept of locality. The short-range energy of the system is decomposed into the sum of environment-dependent atomic energies:

$$E_{\text{short}} = \sum_{i=1}^{N_{\text{atoms}}} E_i(\{G_i\}) \quad , \quad (2.24)$$

where  $E_i$  is the atomic energy of atom  $i$  and  $E_{\text{short}}$  denotes the short-range energy of

the system, which accounts for all atomic interactions between atoms up to a given cutoff radius. Each atomic contribution is calculated by an element-specific ANN and it depends on a set of ACSFs  $\{G_i\}$ , which describe the local atomic environment of atom  $i$ . In this expression, any system size can be handled by adapting the corresponding number of ANNs.

### 2.2.1.2 Atom-Centered Symmetry Functions

One of the crucial components for the construction of HDNNPs is ACSFs, as they provide structural fingerprints of the atomic environment within a cutoff radius. A main advantage of using ACSFs for the construction of HDNNPs is to ensure that the potential energy of the system is invariant under the translation, the rotation, or the permutation of the atoms. Several types of ACSFs have been developed to describe radial and angular information within the local atomic environment. The most commonly used functional forms of ACSFs are as follows:

$$G_{\text{radial},i} = \sum_{j \neq i}^{N_{\text{neig}}} e^{-\eta(R_{ij}-R_s)^2} f_c(R_{ij}) \quad , \quad (2.25)$$

$$G_{\text{angular},i} = 2^{1-\zeta} \sum_{j,k \neq i}^{N_{\text{neig}}} (1 + \lambda \cos \theta_{ijk})^\zeta e^{-\eta(R_{ij}^2 + R_{ik}^2 + R_{jk}^2)} f_c(R_{ij}) f_c(R_{ik}) f_c(R_{jk}) \quad . \quad (2.26)$$

The radial symmetry function  $G_{\text{radial},i}$  describes the coordination at various distances from the central atom  $i$  and the angular symmetry function  $G_{\text{angular},i}$  describes the angular distribution at various distances and angles from the central atom  $i$ . Notably, these are many-body descriptors due to the fact that all two-body and three-body terms within the atomic environment are considered. The parameter  $\eta$  controls the decay rate of the Gaussian function.  $R_s$  shifts the center of the Gaussian functions by a certain radial distance.  $f_c$  is a cutoff function to ensure that the ACSF values and their derivatives smoothly decay to zero at a cutoff radius  $R_c$ , which is typically set to 6-10 Å.

Two typical cutoff functions based on the cosine and the hyperbolic tangent are

$$f_c(R_{ij}) = \begin{cases} \frac{1}{2} \left[ \cos\left(\frac{\pi R_{ij}}{R_c}\right) + 1 \right] & \text{for } R_{ij} \leq R_c \\ 0 & \text{for } R_{ij} > R_c \end{cases} \quad (2.27)$$

and

$$f_c(R_{ij}) = \begin{cases} \tanh^3\left(1 - \frac{R_{ij}}{R_c}\right) & \text{for } R_{ij} \leq R_c \\ 0 & \text{for } R_{ij} > R_c \end{cases} \quad . \quad (2.28)$$

More detailed information about the ACSFs and cutoff functions for constructing HDNNPs can be found in the recent literature [16, 52]. These local structural fingerprints with a

set of parameters  $\lambda$ ,  $\eta$  and  $\zeta$ , which provide a distinguishable representation of different chemical environments, are then fed into ANNs to predict the atomic energy contribution. Fig. 2.2 shows the spatial shape of the ACSFs  $G_{\text{radial},i}$  and  $G_{\text{angular},i}$  with different combinations of parameters.

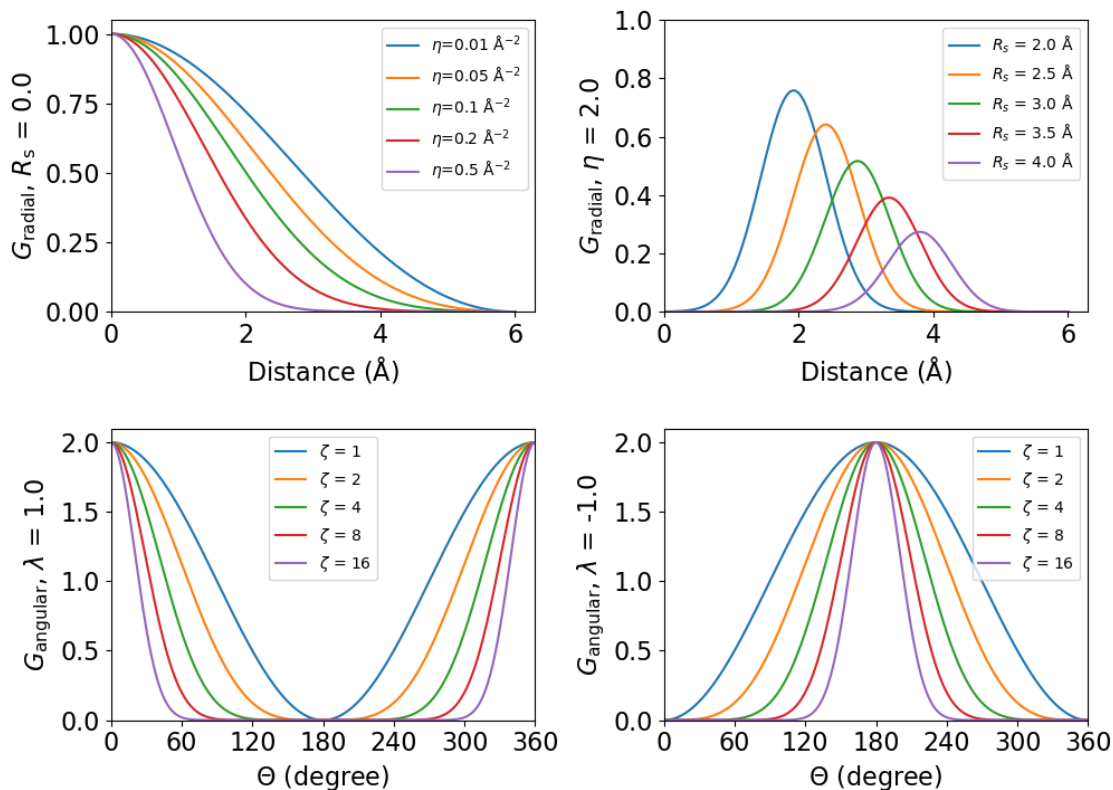


**Fig. 2.2:** Radial and angular symmetry functions with different combinations of parameters. Panel (a) and (b) show the  $G_{\text{radial},i}$  for central atom  $i$  with one neighboring atom only. Here a cosine cutoff function with  $R_c = 6 \text{ \AA}$  is used to ensure that both radial symmetry functions smoothly decay to zero at  $R_c$ . Panel (c) and (d) display the angular contributions of  $G_{\text{angular},i}$  for a triplet system.

### 2.2.1.3 Architecture of Atomic Neural Networks

Apart from ACSFs, ANNs also play a central role in the construction of HDNNPs since the functional relationship between atomic positions and the corresponding atomic energy is expressed by ANNs. The number of ANNs that needs to be parameterized during training depends on the number of chemical elements in the system. For instance, a binary system with elements X and Y requires two different set of ACSFs and ANNs for predicting the atomic contributions of the respective element. ANNs are feed-forward neural networks (FFNNs) as depicted in Fig 2.3. FFNNs consists of an input layer, one

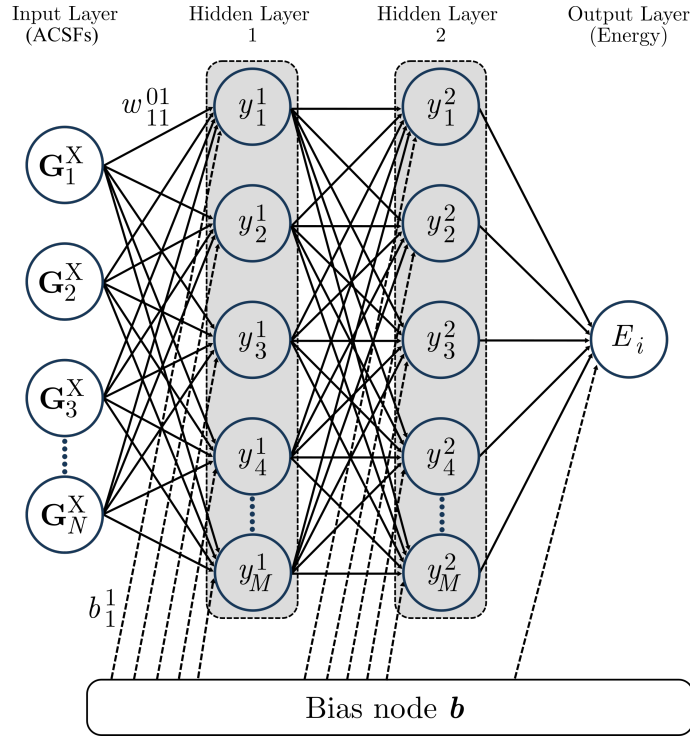


**Fig. 2.3:** Schematic structure of an atomic neural network for element X. Each symmetry function represents a single input neuron and this information passes through two hidden layers that contain  $M$  hidden neurons, to the output layer yielding atomic energy  $E_i$ . Every neuron in the adjacent layer is fully connected by the weight as indicate in the solid line.  $w_{11}^{01}$  is the weight connecting the neuron  $G_1^X$  in layer 0 (input layer) with the neuron 1 in layer 1 (1<sup>st</sup> hidden layer). A set of bias weight values  $\{b\}$  is connected to hidden neurons and an output neuron as shown in dashed line.  $b_1^1$  is the bias value for the neuron 1 in the hidden layer 1.

or more hidden layers, and an output layer. Each layer in principle can have an arbitrary number of nodes depending on the application.

In the case of ANNs, the input neurons correspond to ACSFs and the output neuron represents the resulting atomic energy contribution. The nodes in the hidden layers have no physical meaning but provide the non-linearity of the neural network in predicting high-dimensional functions such as the PES. The flexibility of the functional relation between ACSFs and atomic energy contribution crucially depends on the number of hidden layers and nodes per layer. Each neuron is fully connected to the neurons in the adjacent layers by weights and information moves forward from the input layer, through the hidden layers, to the output layer in a single direction. In addition, a bias value is connected to every neuron in the hidden layers and the output layer.

The value of a node  $y_j^l$  can then be calculated in the following way:

$$y_j^l = f_j^l \left( \sum_{i=1}^{N_k} y_i^k w_{ij}^{kl} + b_j^l \right). \quad (2.29)$$

where  $f_j^l$  is an activation function for neuron  $j$  in layer  $l$ .  $y_i^k$  is the value of node  $i$  in layer  $k = l - 1$  and  $w_{ij}^{kl}$  is the weight connecting node  $i$  in layer  $k$  with node  $j$  in layer  $l$ .  $b_j^l$  is the bias value for neuron  $j$  in layer  $l$ . The value of a node  $j$  is calculated by summing over all node values in the last layer  $k$  multiplied by the respective weights that connect with node  $i$ . The activation function  $f_j^l$  introduces the non-linearity into the model. The same type of activation function is often used for all neurons in a layer. The common type of activation functions for hidden layers in ANNs are chosen as the hyperbolic tangent or the sigmoid function. The activation function for the output layer is chosen as a linear function to avoid any boundary for the range of possible resulting atomic energy contributions predicted by ANNs.

$N_k$  is the number of neurons in layer  $k$  and typical number of hidden neurons for constructing PESs ranges from 15-40. The resulting atomic energies predicted by ANNs are summed up to yield  $E_{\text{short}}$ .

#### 2.2.1.4 Force and Stress Calculations

In order to perform MD simulations, one needs to calculate the atomic forces and, possibly, the stress in a system. In 2G-HDNNPs, the short-range force contribution  $F_{k,\alpha}^{\text{short}}$  acting on atom  $k$  along direction  $\alpha = \{x, y, z\}$  with respect to coordinate  $R_{k,\alpha}$  can be calculated analytically using the following chain rules:

$$F_{k,\alpha}^{\text{short}} = -\frac{\partial E_{\text{short}}}{\partial R_{k,\alpha}} = -\sum_{i=1}^{N_{\text{atoms}}} \frac{\partial E_i}{\partial R_{k,\alpha}} = -\sum_{i=1}^{N_{\text{atoms}}} \sum_{j=1}^{N_{\text{sym},i}} \frac{\partial E_i}{\partial G_{i,j}} \frac{\partial G_{i,j}}{\partial R_{k,\alpha}}, \quad (2.30)$$

where  $N_{\text{sym},i}$  represents the number of ACSFs describing atom  $i$  and  $G_{i,j}$  is the  $j^{\text{th}}$  symmetry function of atom  $i$ . The first term,  $\frac{\partial E_i}{\partial G_{i,j}}$  can be obtained by the back-propagation of the neural network, the second term  $\frac{\partial G_{i,j}}{\partial R_{k,\alpha}}$  can be calculated from the expression of the employed symmetry functions. The atomic forces depend on the atomic environment with effectively two cutoff spheres, since the atomic forces acting on the central atom are calculated from the sum of the atomic energies within its local environment and these atomic energies also rely on their own local environment.

The expression of stress contribution of atom  $i$  to the static stress matrix  $\sigma_{i,\alpha\beta}^{\text{static}}$  is pro-

vided in Ref. [16]:

$$\sigma_{i,\alpha\beta}^{\text{static}} = \sum_{j=1}^{N_{\text{atoms}}} R_{ij,\alpha} F_{j,\beta} = - \sum_{k=1}^{N_{\text{atoms}}} \sum_{v=1}^{N_{\text{sym},k}} \frac{\partial E_k}{\partial G_{k,v}} \sum_{j=1}^{N_{\text{atoms}}} R_{ij,\alpha} \frac{\partial G_{k,v}}{\partial R_{j,\beta}}, \quad (2.31)$$

where  $R_{ij,\alpha}$  is defined as the difference of the Cartesian coordinate between atom  $i$  and  $j$  along direction  $\alpha$ , i.e.,  $R_{ij,\alpha} = R_{i,\alpha} - R_{j,\alpha}$ . These equations enable the efficient calculation of forces and stress tensors for performing MD simulations. Hence, HDNNPs have become a useful tool for atomistic simulations since they can considerably extend the time scale and the system size with linear scaling  $O(N)$ , while their accuracy is in good agreement with reference electronic structure calculations.

### 2.2.1.5 Modifications of Second-Generation HDNNP

In recent years, several attempts have been made to modify the ACSF for the construction of HDNNPs. For instance, generally applicable HDNNPs like ANI-1 [114], which employs modified angular symmetry functions, have been reported for a wide range of organic molecules. Besides, Gastegger et al. proposed weighted atom-centered symmetry functions (wACSFs) [115], which aim to overcome the undesirable scaling of the number of ACSFs with the number of elements in the system. The general idea of wACSFs is to introduce a set of element-dependent weight functions to modify the contribution of each radial and angular term so that the wACSFs values are distinguishable for all element types. In this way the number of ACSFs is independent of the number of elements in the system.

In addition to the modifications of ACSFs, the element-specific ANNs have been replaced by a single universal ANN in combination with wACSFs for constructing a PES for a system containing multiple chemical species [116]. In this model, the number of atomic energy outputs depends on the number of elements in a system and all of them share the same weights in the hidden layers, while the linear weights connected to the output layer are element-specific. The expected outcome of this development is to increase the transferability of the model to different data sets that contain different elements by only training the linear weights in the output layer. Hence, the training time for the construction of PES can be markedly reduced.

Still, due to the limited number of reported studies using these modifications of 2G-HDNNP, their actual performance in terms of accuracy and efficiency remains unknown since the flexibility of the model, which crucially depends on the quality of ACSFs and the number of element-specific ANNs for constructing HDNNPs, is also reduced after the dimensionality reduction. More detailed investigations of this direction are required in the future.

## 2.2.2 Third-Generation HDNNP

### 2.2.2.1 Overview

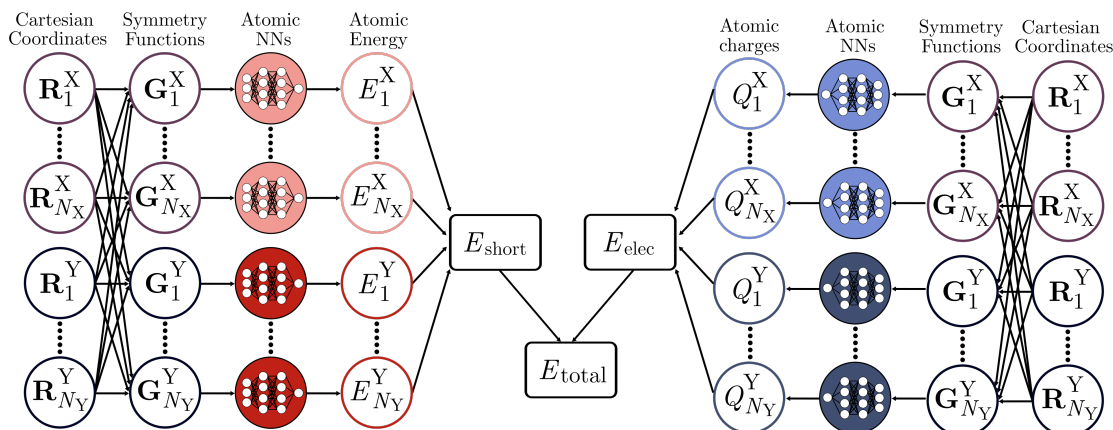


**Fig. 2.4:** Schematic diagram of a 3G-HDNNP for an arbitrary binary system. In addition to the short-range energy calculated by a set of atomic neural networks (left) as usual 2G-HDNNPs, another set of atomic neural networks (right) is trained to predict environment-dependent charges  $Q_i$ . These point charges are then used to calculate the electrostatic energy without truncation according to Coulomb's law. The sum of the electrostatic energy  $E_{elec}$  and short-range energy  $E_{short}$  is equal to the total energy of the system. Reprinted (adapted) with permission from Ref. [79]. Copyright 2021 American Chemical Society.

The 2G-HDNNP is currently one of the most commonly used MLPs and many successful applications for a wide range of systems have been reported [117–120]. Still, 2G-HDNNPs are unable to describe long-range interactions beyond the cutoff radius such as electrostatics and dispersion interactions, which can play an important role in describing many systems. A straight-forward solution is to assign fixed atomic charges depending on the element type and calculate the electrostatic energy explicitly using Coulomb's law. However, this approximation cannot be generalized to different chemical environments since the partial charges can vary according to the arrangement of atomic positions. Therefore, 2G-HDNNPs were extended to include long-range electrostatic interactions, based on environment-dependent charges. This constitutes the third generation of HDNNPs (3G-HDNNPs).

Fig. 2.4 shows the general structure of a 3G-HDNNP for a binary system. In addition to the short-range energies obtained from a 2G-HDNNP, another set of ANNs is introduced to predict environment-dependent charges, which are usually expressed as a function of the same set of ACSFs used for the short-range ANNs. Thus, the total energy expression of 3G-HDNNP consists of the short-range and the long-range electrostatic energy and it

can be written as

$$\begin{aligned}
 E_{\text{total}} &= E_{\text{short}} + E_{\text{elec}} \\
 &= \sum_{i=1}^{N_{\text{atoms}}} E_i(\{G_i\}) + \sum_{i>j}^{N_{\text{atoms}}} \frac{Q_i(\{G_i\})Q_j(\{G_j\})}{R_{ij}} \quad , \quad (2.32)
 \end{aligned}$$

where  $E_{\text{elec}}$  is calculated by summing over all pairwise electrostatic interaction energies between  $Q_i$  and  $Q_j$  using Coulomb's law.  $E_{\text{short}}$  is computed in the same way as in 2G-HDNNPs. The corresponding force expression can be derived from the partial derivative of the total energy with respect to coordinate  $R_{k,\alpha}$ :

$$\begin{aligned}
 F_{k,\alpha}^{\text{total}} &= - \frac{\partial E_{\text{total}}}{\partial R_{k,\alpha}} \\
 &= - \sum_{i=1}^{N_{\text{atoms}}} \sum_{j=1}^{N_{\text{sym},i}} \frac{\partial E_i}{\partial G_{i,j}} \frac{\partial G_{i,j}}{\partial R_{k,\alpha}} - \sum_{i>j}^{N_{\text{atoms}}} Q_i Q_j \frac{\partial}{\partial R_{k,\alpha}} \left( \frac{1}{R_{ij}} \right) \\
 &\quad - \sum_{i>j}^{N_{\text{atoms}}} \frac{1}{R_{ij}} \left( Q_i \frac{\partial Q_j}{\partial R_{k,\alpha}} + Q_j \frac{\partial Q_i}{\partial R_{k,\alpha}} \right) \quad . \quad (2.33)
 \end{aligned}$$

The first term in Eq. 2.33 is the short-range force contribution as in 2G-HDNNPs. The second term is the typical Coulomb forces between two fixed point charges, while the third term represents the force contribution due to the partial derivatives of the partial charges on atom  $i$  and  $j$  with respect to the change of the atomic position  $R_{k,\alpha}$ . These partial derivatives can be calculated from the architecture of ANNs and the ACSFs using the chain rule,

$$\frac{\partial Q_i}{\partial R_{k,\alpha}} = \sum_{j=1}^{N_{\text{sym},i}} \frac{\partial Q_i}{\partial G_{i,j}} \cdot \frac{\partial G_{i,j}}{\partial R_{k,\alpha}} \quad . \quad (2.34)$$

It is noteworthy that the atomic charges only depend on the local atomic environment, which fails to capture global changes in the electronic structure.

To train a 3G-HDNNP, the first step is to convert the atomic coordinates into ACSFs which are fed into ANNs to determine the atomic charges as a function of the local chemical environment. The ANN weights are adjusted during the training process to minimize the error between the predicted and reference charges. In principle, any charge partitioning scheme can be used to obtain the reference charges. Once the ANNs are trained, the electrostatic energy and forces can be calculated through Coulomb's law.

The electrostatic energies and forces have to be removed from the reference calculations to obtain the remaining contribution for the training of the short-range part. In such a manner, double counting of electrostatic contributions can be avoided. The two-step sequential training is necessary because the electrostatic forces require the gradient of the atomic charges with respect to the atomic positions. These quantities can only be obtained from the trained ANNs, which are responsible for predicting charges.

A major limitation of this approach is that the sum of the atomic charges predicted by the ANNs is not guaranteed to equal the correct total charge of the system due to the lack of any constraint. Therefore, a scaling treatment is needed in order to achieve charge conservation:

$$Q_{i,\text{scaled}} = Q_i - \frac{\sum_{j=1}^{N_{\text{atoms}}} Q_j - Q_{\text{total}}}{N_{\text{atoms}}}, \quad (2.35)$$

where  $Q_{\text{total}}$  represents the total charge of the system.  $Q_{i,\text{scaled}}$  is the scaled partial charge of atom  $i$  using Eq. 2.35. In this way, the 3G-HDNNP can be chosen to construct on either the unscaled or scaled charges since the target energies and forces for the training of the short-range part depend on the electrostatic contributions calculated from the charges.

Except for long-range electrostatics, dispersion interactions also play a crucial role in structural stability, catalysis and chemical reactivity [121]. These can be also taken into account explicitly with the 2G-HDNNP framework. For instance, Morawietz and Behler extended the 2G-HDNNP by including addition dispersion interactions for modelling bulk liquid water [122]. The total energy expression is then written as:

$$E_{\text{total}} = E_{\text{short}} + E_{\text{disp}}, \quad (2.36)$$

where  $E_{\text{disp}}$  is calculated using Grimme's D3 method [77]. The reference energy without dispersion corrections are reproduced by the usual 2G-HDNNP. The correction is then directly added on top of the short-range energy predicted by the 2G-HDNNP. This is analogous to applying an empirical correction to density functionals which fail to describe dispersion interactions accurately.

### 2.2.2.2 Screening of Short-Range Electrostatics

When subtracting the long-range electrostatic energy from the reference data, one leaves behind cusps in the remaining short-range part due to the large Coulomb interactions at a very short distance  $R_{ij}$ . This deteriorates the accuracy of short-range fitting. A screening function is introduced to address this problem, and the expression is given in the following:

$$f_{\text{screen}} = \begin{cases} 0 & \text{for } R_{ij} < R_{\text{inner},s} \\ \frac{1}{2} \left( 1 - \cos \left( \frac{\pi(R_{ij} - R_{\text{inner},s})}{R_{\text{outer},s}} \right) \right) & \text{for } R_{\text{inner},s} < R_{ij} < R_{\text{outer},s} \\ 1 & \text{for } R_{ij} > R_{\text{outer},s} \end{cases} \quad (2.37)$$

where  $R_{\text{inner},s}$  and  $R_{\text{outer},s}$  define the inner and outer cutoff radius that determine the range of the screening function.

The screened electrostatic energy of the system is given by

$$E_{\text{elec,screen}} = \sum_{i>j}^{N_{\text{atoms}}} \frac{Q_i Q_j}{R_{ij}} \cdot f_{\text{screen}} \quad . \quad (2.38)$$

The corresponding screened electrostatic forces are obtained by taking the partial derivative of the screened electrostatic energy with respect to coordinate  $R_{k,\alpha}$

$$\begin{aligned} F_{k,\alpha}^{\text{elec,screen}} = \frac{dE_{\text{elec,screen}}}{dR_{k,\alpha}} = & - \sum_{i>j}^{N_{\text{atoms}}} Q_i Q_j \frac{\partial}{\partial R_{k,\alpha}} \left( \frac{1}{R_{ij}} \right) f_{\text{screen}} \\ & - \sum_{i>j}^{N_{\text{atoms}}} \frac{1}{R_{ij}} \left( Q_j \frac{\partial Q_i}{\partial R_{k,\alpha}} + Q_i \frac{\partial Q_j}{\partial R_{k,\alpha}} \right) \cdot f_{\text{screen}} \\ & - \sum_{i>j}^{N_{\text{atoms}}} \frac{1}{R_{ij}} Q_i Q_j \frac{\partial f_{\text{screen}}}{\partial R_{k,\alpha}} \quad . \end{aligned} \quad (2.39)$$

Notably, the screening of short-range electrostatics does not affect the total PES in general, since the screened contributions are automatically covered by the remaining short-range part. This ensures that the total energy of the system is conserved during simulations. Typically, the  $R_{\text{outer,s}}$  is chosen to be the cutoff radius of ACSFs so that all interactions beyond the short-range part are considered as long-range electrostatics.

### 2.2.3 Charge Equilibration Using Neural Network Technique

Before starting the development of fourth-generation MLPs, some early attempts have been made to describe long-range charge transfer. In 1991, Rappe and Goddard [83] proposed the Qeq scheme to predict charge distributions of the system. The basic idea of Qeq scheme is to distribute the charges in an optimal way to minimize the energy expression

$$\begin{aligned} E_{\text{total}}(\{Q_i\}, \{R_i\}) = & \sum_{i=1}^{N_{\text{atoms}}} \left( E_i^0 + \chi_i Q_i + \frac{1}{2} \eta_i Q_i^2 \right) + \\ & \frac{1}{2} \iint \frac{\rho(\mathbf{R})\rho(\mathbf{R}')}{|\mathbf{R} - \mathbf{R}'|} d\mathbf{R} d\mathbf{R}' \quad . \end{aligned} \quad (2.40)$$

The Eq. 2.40 contains the second order Taylor expansion of the atomic energy as a function of the partial charges and Coulomb interactions. The constant term  $E_i^0$  denotes the energy of an isolated atom. The coefficient of the linear and quadratic terms is referred to as the atomic electronegativity  $\chi_i$  and hardness  $\eta_i$ , respectively, and the resulting charge distribution depends on the atomic positions as well as these coefficients. The Qeq scheme is ready to use once the electronegativities and hardnesses are parameterized from a set of

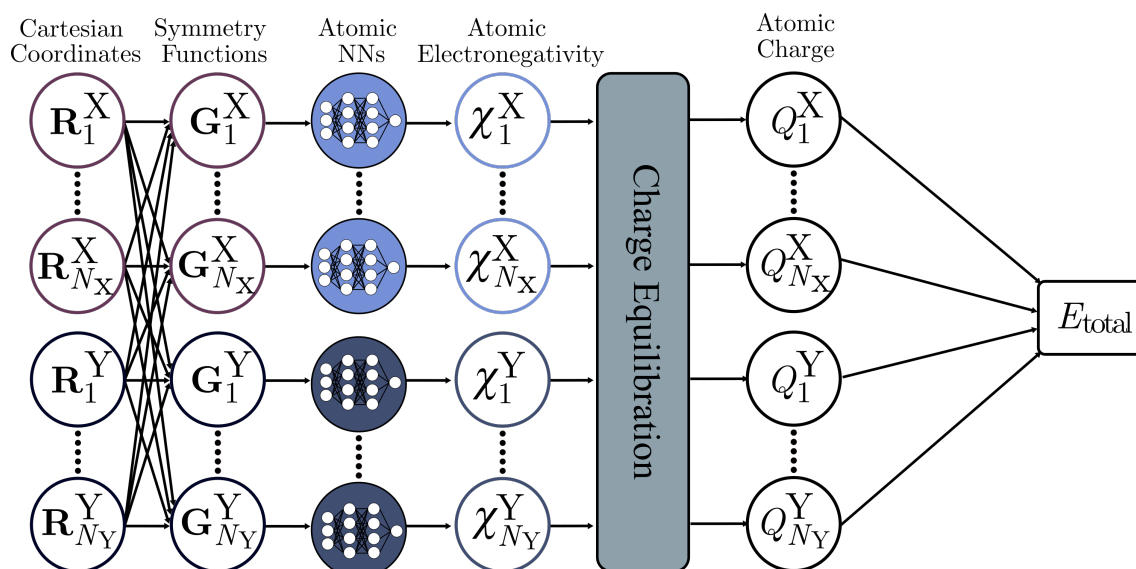


**Fig. 2.5:** Architecture of a CENT for a binary system. Instead of directly predicting atomic energies, the intermediate physical quantities, so-called electronegativities  $\chi_i$ , as a function of atom-centered symmetry functions  $\{G_i\}$  are obtained from atomic neural networks. These environment-dependent electronegativities are then used to determine the global charge distributions with element dependent hardness and width of Gaussian charge density according to charge equilibration scheme. The total energy of the system is then computed from these equilibrated charges  $Q_i$  using Eq. 2.41. Reprinted (adapted) with permission from Ref. [79]. Copyright 2021 American Chemical Society.

reference calculations or experimental data.

Some modern empirical force fields such as COMB [123, 124] and ReaxFF [12] have successfully employed this scheme to describe a variety of systems [125–129]. However, these force fields are unable to provide an acceptable accuracy for describing charge transfer in complicated systems since the electronegativity depends on the atomic environment via simple analytical functions only.

In 2015, the first non-local fourth-generation MLP was proposed to overcome the limitation of Qeq-based empirical force fields: the charge equilibration via neural network technique (CENT) [82, 84]. Fig 2.5 shows the architecture of a CENT model for a binary system. In CENT, the atomic electronegativities  $\chi_i$  are assumed to be local environment-dependent properties. The local atomic environments are represented by ACSFs, which serves as inputs for ANNs yielding the electronegativities. This can provide much more flexibility for the model to accurately describe long-range charge transfer and systems with multiple charge states. CENT is conceptually equivalent to 2G-HDNNPs [50] whose ANNs determine the environment-dependent energy contribution. This demonstrates the flexibility of the ANN approach, which can further be generalized for predicting other

local atomic physical properties such as partial charges, polarizabilities, and spins [130].

The CENT method was originally developed for describing ionic materials and therefore the total energy expression is the same as for the Qeq scheme in Eq. 2.40 and no additional terms are needed. The charge density  $\rho(\mathbf{R})$  is represented by the Gaussian

$$\rho_i(\mathbf{R}) = \frac{Q_i}{\alpha_i^3 \pi^{\frac{3}{2}}} \exp\left(-\frac{|\mathbf{R} - \mathbf{R}_i|^2}{\alpha_i^2}\right) ,$$

where  $\rho_i(\mathbf{R})$  describes the electron density at atom  $i$  as a function of the distance between  $\mathbf{R}$  and atomic position  $\mathbf{R}_i$ .  $\alpha_i$  controls the width of the Gaussian. This functional form enables the straightforward calculation of the overlap of charge densities as the superposition of two Gaussians. The total energy of Eq. 2.40 for non-periodic systems can thus be calculated analytically,

$$\begin{aligned} E_{\text{total}}(\{Q_i\}, \{\mathbf{R}_i\}) &= \sum_{i=1}^{N_{\text{atoms}}} \left( E_i^0 + \chi_i Q_i + \frac{1}{2} \eta_i Q_i^2 + \frac{Q_i^2}{\sqrt{2\pi}\alpha_i} \right) \\ &+ \sum_{i>j}^{N_{\text{atoms}}} Q_i Q_j \frac{\text{erf}(\gamma_{ij} R_{ij})}{R_{ij}}, \end{aligned} \quad (2.41)$$

where  $\gamma_{ij} = (\alpha_i^2 + \alpha_j^2)^{-\frac{1}{2}}$  and  $R_{ij}$  is the distance between atoms  $i$  and  $j$ . The Coulomb interactions for periodic systems can be calculated using Ewald summation [131]. The charge distribution can be obtained by taking the partial derivative of the total energy with respect to the charge  $Q_i$  and setting it equal to zero,

$$\frac{\partial E_{\text{total}}}{\partial Q_i} = 0, \forall i = 1, \dots, N_{\text{atoms}} \implies \sum_{j=1}^{N_{\text{atoms}}} A_{ij} Q_j + \chi_i = 0 , \quad (2.42)$$

where the elements of the matrix  $\mathbf{A}$  are given by

$$\mathbf{A}_{ij} = \begin{cases} \eta_i + \frac{\sqrt{2}}{\sqrt{\pi}\alpha_i} & \text{if } i = j \\ \frac{\text{erf}(\gamma_{ij} R_{ij})}{R_{ij}} & \text{otherwise} \end{cases} . \quad (2.43)$$

A  $(N_{\text{atoms}} + 1)$  by  $(N_{\text{atoms}} + 1)$  system of linear equations is constructed by including the constraint that the sum over all atomic charges must be equal to the total charge  $Q_{\text{total}}$ , via introducing a Lagrange multiplier  $\lambda$ ,

$$\left( \begin{array}{c|c} \mathbf{A} & \begin{matrix} 1 \\ \vdots \\ 1 \\ 0 \end{matrix} \end{array} \right) \begin{pmatrix} Q_1 \\ \vdots \\ Q_{N_{\text{atoms}}} \\ \lambda \end{pmatrix} = \begin{pmatrix} -\chi_1 \\ \vdots \\ -\chi_{N_{\text{atoms}}} \\ Q_{\text{total}} \end{pmatrix} \quad (2.44)$$

where  $N_{\text{atoms}}$  represents the number of atoms. The redistributed charges can be calculated by solving this system of linear equations. CENT has been successfully applied to both neutral and charged ionic systems with nearly ab-initio accuracy [82]. Furthermore, the excellent transferability of CENT has been demonstrated for completely new structure predictions of materials like transitional metal oxides [132, 133].

In CENT, the force acting on atom  $k$  with respect to coordinate  $R_{k,\alpha}$  is given by

$$F_{k,\alpha}^{\text{total}} = -\frac{\partial E_{\text{total}}}{\partial R_{k,\alpha}} - \sum_{i=1}^{N_{\text{atoms}}} \frac{\partial E_{\text{total}}}{\partial Q_i} \frac{\partial Q_i}{\partial R_{k,\alpha}}. \quad (2.45)$$

Here the second term vanishes as required by Eq. 2.42. Therefore the calculation of the partial derivatives  $\frac{\partial Q_i}{\partial R_{k,\alpha}}$  is not needed, which avoids solving many systems of linear equations. This is similar to the use of the Hellmann-Feynman theorem in standard DFT, which states that the derivative of the electron density with respect to the atomic positions is not required. As a result, only the first term of the equation has to be expanded and the formula becomes

$$F_{k,\alpha}^{\text{total}} = -\sum_{i=1}^{N_{\text{atoms}}} \left( Q_i \frac{\partial \chi_i}{\partial R_{k,\alpha}} \right) + \sum_{i>j}^{N_{\text{atoms}}} Q_i Q_j \frac{\partial}{\partial R_{k,\alpha}} \left( \frac{\text{erf}(\gamma_{ij} R_{ij})}{R_{ij}} \right), \quad (2.46)$$

where the partial derivatives of the electronegativities with respect to the atomic positions can be obtained from the architecture of the ANNs and the employed ACSFs. The first term describes the force exerted on atom  $k$  due to the local charge distribution around this atom. The second term represents the force contribution arising from the electrostatic energy of the global charge distribution excluding the self-interaction of Gaussian charges.

In the training stage of CENT, the neural network weights are adjusted such that the error of total energy with respect to reference methods is minimized. This means that the value of the resulting atomic charges obtained from the charge equilibration scheme does not have a physical meaning.

## 2.2.4 Short Summary

2G-HDNNPs [50] provide a very flexible functional form for describing atomic energies as a function of the local chemical environment. The model is generally applicable to any type of chemical bonding such as ionic, metallic and covalent bonds. However, 2G-HDNNPs are unable to describe long-range electrostatic interactions beyond the cutoff radius.

The 3G-HDNNP [72] method overcomes the limitation of 2G-HDNNPs by introduc-

ing flexible environment-dependent charges predicted by another set of ANNs. These charges are used to calculate long-range electrostatic interactions without truncation. Still, 3G-HDNNPs cannot describe non-local effects caused by long-range charge transfer and cannot account for multiple charge states. In addition, the sum of the atomic charges is not guaranteed to agree with the correct total charge of the system.

All these remaining problems can be addressed by fourth-generation machine learning potentials such as CENT [82], which is based on a charge equilibration scheme to capture the global charge distribution due to the change of the electronic structure. Despite the capability of describing non-local effects, CENT is less accurate when modelling mixed ionic-covalent interactions due to a lack of accurate description for covalent contributions in the total energy expression. It is expected that such systems can be accurately described by combining both the advantages of 2G-HDNNPs and CENT.

## 2.3 Molecular Dynamics Simulations

### 2.3.1 Overview

Molecular dynamics (MD) simulations are a computational tool for investigating the structural and dynamic properties of molecules and bulk materials by analyzing their motion. The basic idea of MD simulations is to predict the motion of the system during time evolution by solving the classical Newtonian equations of motion, which is based on the assumption that all nucleus are considered as classical particles. This problem involves solving a system of  $N_{\text{atoms}}$  coupled second order non-linear differential equations. It can be only solved numerically by discretizing the trajectory and using an integrator to propagate over small time steps. Commonly used integrators include the velocity Verlet algorithm,[134] the leapfrog algorithm [135], and predictor-correctors algorithms [136].

The reliability of the simulation results relies on an accurate description of the atomic interactions provided by the chosen method for energy and force calculations such as DFT or empirical force fields. In this section, two popular approaches for performing MD simulations that have been applied in this work are introduced. Other technical details of molecular dynamics simulations such as propagators and ensembles can be found in the literature [136]. In addition, the minima hopping algorithm [137], which aims to search the minimum on the PES based on MD simulations, employed in this work is also presented.

### 2.3.2 Born-Oppenheimer Molecular Dynamics

The position and velocity of nuclei are determined by Newton's equation of motion

$$\mathbf{F}_k = -\frac{\partial E_{\text{total}}}{\partial \mathbf{R}_k} = m_k \ddot{\mathbf{R}}_k, \quad (2.47)$$

where the  $m_k$  and  $\ddot{\mathbf{R}}_k$  denote the mass and acceleration of nucleus  $k$ , respectively. The force acting on nucleus  $k$ , which is equal to the negative partial derivative of the total energy with respect to the atomic positions  $-\frac{\partial E_{\text{total}}}{\partial \mathbf{R}_k}$ , can be calculated using DFT based on the Born-Oppenheimer approximation.

The concept of Born-Oppenheimer molecular dynamics (BOMD) is to solve the static electronic structure problem under the Born-Oppenheimer approximation at every time step given that the position of nuclei are fixed. Hence, the time-independent Schrödinger equation has to be solved. The forces acting on nuclei due to the electron-nucleus and nucleus-nucleus interactions can be calculated using the Hellmann-Feynman theorem. The theorem states that the partial derivative of the total energy with respect to a parameter  $\lambda$  is equal to the expectation value of the derivative of the Hamiltonian with respect to the same parameter. This can be derived in the following way:

$$\begin{aligned} \frac{\partial E_{\text{total}}}{\partial \lambda} &= \frac{\partial \langle \Psi | \hat{H} | \Psi \rangle}{\partial \lambda} \\ &= \left\langle \frac{\partial \Psi}{\partial \lambda} | \hat{H} | \Psi \right\rangle + \langle \Psi | \frac{\partial \hat{H}}{\partial \lambda} | \Psi \rangle + \langle \Psi | \hat{H} | \frac{\partial \Psi}{\partial \lambda} \rangle. \end{aligned} \quad (2.48)$$

When  $\Psi$  is an eigenstate, the Eq. 2.48 can be rewritten as:

$$\frac{\partial E_{\text{total}}}{\partial \lambda} = E_{\text{total}} \left\langle \frac{\partial \Psi}{\partial \lambda} | \Psi \right\rangle + E_{\text{total}} \left\langle \Psi | \frac{\partial \Psi}{\partial \lambda} \right\rangle + \langle \Psi | \frac{\partial \hat{H}}{\partial \lambda} | \Psi \rangle. \quad (2.49)$$

The first two terms vanish since the partial derivative of the overlap of a wavefunction with itself is equal to zero given the identity of normalized wavefunctions.

The force calculations are analogous to Eq. 2.49, which is now the partial derivative of  $E_{\text{total}}$  with respect to  $R_{k,\alpha}$  and assuming that the nuclei are classical particles with the corresponding mass  $m_i$ . The position of nuclei can be updated by solving the equations of motion

$$m_i \ddot{\mathbf{R}}_k = -\langle \Psi | \frac{\partial \hat{H}}{\partial \mathbf{R}_k} | \Psi \rangle. \quad (2.50)$$

The basic flow chart of BOMD simulations is given in Fig. 2.6. First, the atomic positions and velocities are initialized. The velocities are usually randomly assigned on each atom according to the Maxwell-Boltzmann distribution, which provides a reason-

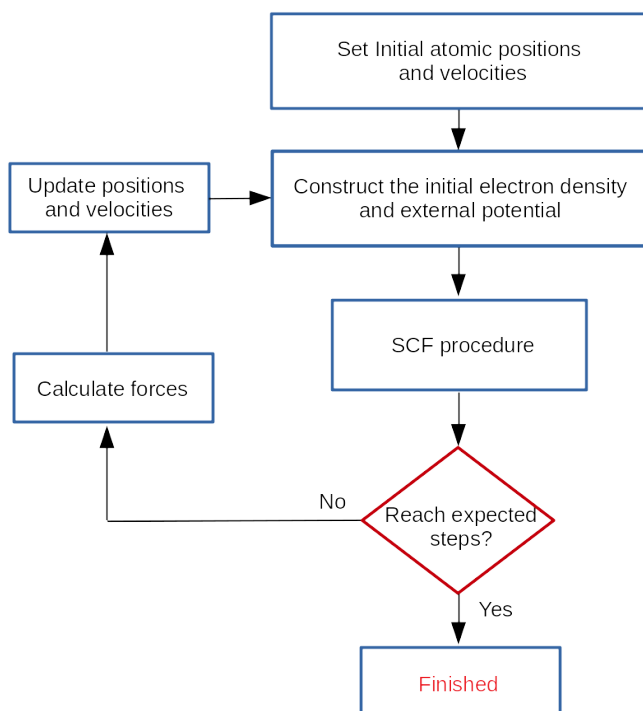


**Fig. 2.6:** Workflow of Born-Oppenheimer molecular dynamics.

able starting point for BOMD simulations at a given temperature. The process of the BOMD begins with setting the initial electron density and external potential for the construction of the Kohn-Sham equations. The ground state energy of the system is obtained after the SCF procedure. The corresponding atomic forces are then calculated using the Hellmann-Feynman theorem. Next, the nuclear positions and velocities can be updated based on the atomic forces according to the equation of motion with a numerical integration scheme. Additional constraints like thermostats or barostats can be imposed on the system depending on the given ensemble. These processes are repeating until the desired number of time steps have been performed.

In practice, most BOMD simulations are performed on a ground state PES. Although the BOMD provides a reliable description for a wide range of systems, it is computationally very demanding to compute forces on the fly from electronic structure calculations and therefore this prevents the investigation of various interesting phenomena.

### 2.3.3 Classical Molecular Dynamics

Classical molecular dynamics are driven by empirical force fields. Instead of solving the electronic structure problem on the fly for the force calculations, empirical force fields

provide a direct mapping from atomic positions and possible charges to the corresponding potential energy of a system. Depending on the functional form of force fields, the atomic forces can be derived analytically using Eq. 2.47. Therefore, they can be used to study very large systems at significantly reduced computational cost.

Most computationally efficient empirical force fields can be expressed as a sum of bonded and non-bonded interaction terms. The former term can be described by simple analytical functions of the bond lengths, angles and dihedrals torsion between atoms. The non-bonded interactions include long-range pairwise electrostatic and dispersion interactions, based on Coulomb's law and Lennard-Jones potentials. Such force fields are able to simulate systems up to hundreds of thousands of atoms. Many interesting applications such as the exploration of folding dynamics and other biophysical processes [138] as well as the investigation of phase transitions and surface reconstructions [139, 140] have been reported.

The workflow of classical molecular dynamics is the same as for BOMD except that the whole SCF procedure including the initialization during every time step is not required. However, the accuracy of force fields is limited by their simple functional form. Hence, the reliability of the properties that are obtained from MD simulations is limited by the accuracy of the underlying force fields. Nowadays, MLPs have become an alternative tool to perform large-scale MD simulations since they are significantly more accurate than modern empirical force fields with comparable efficiency.

### 2.3.4 Minima Hopping

A useful application of molecular dynamic simulations is minima hopping [137, 141], which aims to find the global minimum of the PES of complex systems. Finding their ground state structure is usually very computationally expensive, since the number of local minima increases exponentially with number of atoms [137]. In addition, the system often needs to go through a great deal of intermediate local minima, which requires overcoming high energy barriers.

In many studies, Monte Carlo based algorithms [142, 143] are employed for global optimization problems. However, these schemes tend to revisit neighboring configurations that are close in energy. Hence, the simulations can keep jumping back and forth between two configurations if crossing high energy barriers is required to reach other configurations. All these limitations can be overcome by minima hopping, which limits repeated visits by performing escape trials at a higher temperature for already visited minima.

The minima hopping algorithm depends on the parameters  $\alpha_r$ ,  $\alpha_a$ ,  $\beta_n$ ,  $\beta_s$ ,  $\beta_o$ ,  $E_{\text{diff}}$ . The first five parameters control the temperatures for performing MD simulations according to the kinetic energy  $E_{\text{kin}}$ .  $\beta_s$  and  $\alpha_r$  are set to be larger than 1.0 and other parameters are set to below 1.0. The last parameter  $E_{\text{diff}}$  determines whether the escaped minimum is

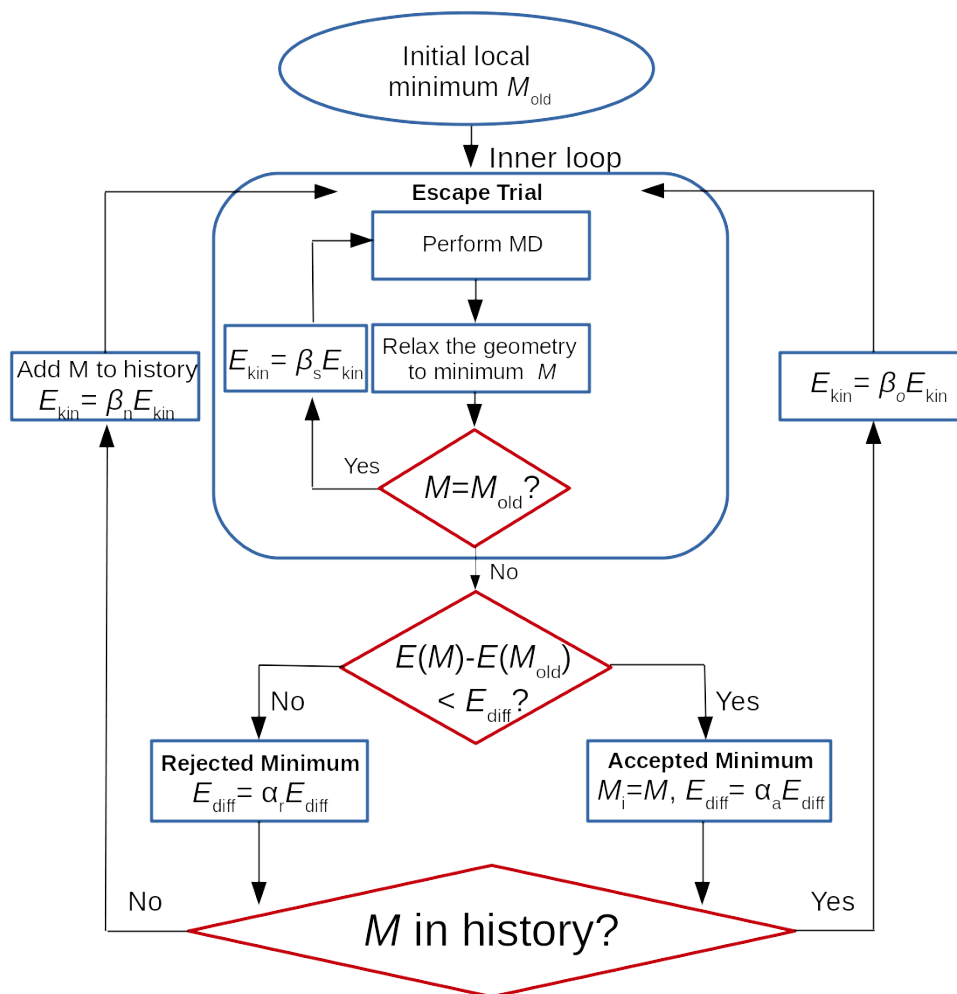


**Fig. 2.7:** Flowchart of the minima hopping algorithm [137].

accepted or rejected.

The flowchart of the algorithm is given in Fig. 2.7. The simulation starts by the escape trial. The current minimum is used to perform molecular dynamic simulations at given temperature  $E_{\text{kin}}$  for a certain number of time steps. The geometry at the end of the MD run is then relaxed to the closest minimum on the PES. These procedures repeat with increased temperature by multiplying a factor of  $\beta_s$  until the current minimum is escaped. The new minimum  $M$  is considered to be accepted if  $E_{\text{diff}}$  is larger than the energy difference between the current minimum and the last minimum ( $E(M) - E(M_{\text{old}})$ ). Then the  $E_{\text{diff}}$  is decreased by multiplying a factor of  $\alpha_a$ . Otherwise, the minimum is rejected and the  $E_{\text{diff}}$  is increased by multiplying a factor of  $\alpha_r$ . If the current minimum has already been found in the past, the temperature is increased by multiplying a factor

of  $\beta_0$ . Otherwise, the minimum is added to the history and the temperature is reduced by multiplying  $\beta_n$ . The whole loop is completed when the target number of found minima is reached or the simulation becomes unstable due to ever increasing escape temperatures.

The choice of parameter values affects the overall performance of the algorithm. The global minimum is found faster with larger values. However, some cases the ground state structure can be missed. Detailed information about the minima hopping can be found in Ref. [137]. The reliability of minima, which are obtained by minima hopping, depends on the accuracy of the PES. MLPs are tailor-made for running such simulations, since they provide excellent accuracy and are computationally efficient for modeling large-scale systems at numerous number of time steps. Many applications based on minima hopping algorithm driven by MLPs for structure prediction have been reported in recent years [133, 144, 145].



# Chapter 3

## Computational Details

### 3.1 Overview

The capabilities of 4G-HDNNP are demonstrated on benchmark systems as diverse as a long linear carbon chain ( $C_{10}H_2/C_{10}H_3^+$ ), a small silver trimer ( $Ag_3^+/Ag_3^-$ ), a sodium chloride cluster fragment ( $Na_8Cl_8^+/Na_9Cl_8^+$ ) and a magnesium oxide surface-supported gold dimer with or without Al doping ( $Au_2-MgO/Al$ -doped  $Au_2-MgO$ ). The data set of sodium chloride and a gold dimer on a magnesium oxide slab were generated by Jonas Finkler.

Apart from that, the considerable improvement obtained from the ee4G-HDNNP model when compared to 4G-HDNNPs is revealed on a data set containing both neutral and negatively charged sodium chloride clusters with large structural diversity. In this chapter, the computational details for the generation of reference data sets, construction of HDNNPs and settings of the minima hopping algorithm driven by the ee4G-HDNNP are presented.

### 3.2 Reference Data Generation

All DFT data points were generated using the electronic structure code Fritz Haber Institute ab initio molecular simulations package (FHI-aims) [146], which is an all-electron, full-potential electronic structure code for simulating bulk systems and molecules. The code supports DFT calculations including semi-local and hybrid functionals based on atom-centered basis functions.

The PBE exchange-correlation functional was used to take electron exchange and correlation interaction into account. The "light" setting of basis sets and integration grid density were applied to all testing systems. The SCF convergence criteria including the charge density, sum of eigenvalues and the total energy for all systems except  $Au_2-MgO/Al$ -doped  $Au_2-MgO$ , were set to  $10^{-4}$  eV,  $10^{-2}$  e, and  $10^{-5}$  eV, respectively. A

tighter convergence for the Au<sub>2</sub>-MgO/Al-doped Au<sub>2</sub>-MgO system was applied by multiplying each criterion used for the other systems by a factor of 0.1. Furthermore, a 3×3×1 k-space integration grid was employed to evenly distributed along the three reciprocal lattice axis of the first Brillouin zone.

A treatment of spin collinearity was taken into account for the Ag<sub>3</sub>, NaCl and Au<sub>2</sub>-MgO systems. The zero-order regular approximation (ZORA) [147] was used to take relativistic effects into account for all elements heavier than 20 u. Reference atomic charges were integrated using the Hirshfeld charge partitioning scheme [113]. The DFT-based geometry optimizations were performed using Broyden-Fletcher-Goldfarb-Shanno (BFGS) algorithm [148]. A Nosé-Hoover thermostat was applied to all BOMD simulations under the canonical (NVT) ensemble [149], and the thermostat parameter was set to 1700 cm<sup>-1</sup>.

The data sets of C<sub>10</sub>H<sub>2</sub>/C<sub>10</sub>H<sub>3</sub><sup>+</sup> and Ag<sub>3</sub><sup>+</sup>/Ag<sub>3</sub><sup>-</sup> were constructed by performing BOMD simulations for each system at 300 K with 5000 time steps. The step size for numerically integrating the equations of motion was chosen to be 0.5 fs. The initial structure of the system for MD simulations was obtained by geometry optimization. The structures generated at each step of the geometry relaxation, which employed a force threshold of 0.001 eV/Å, were also added to the data set in order to make sure that the region close to the equilibrium structure had been well sampled. The geometry optimization of the Ag<sub>3</sub><sup>-</sup> was terminated when reaching forces below 0.0015 eV/Å.

The data set of Na<sub>8</sub>Cl<sub>8</sub><sup>+</sup>/Na<sub>9</sub>Cl<sub>8</sub><sup>+</sup> clusters was constructed based on the optimized Na<sub>9</sub>Cl<sub>8</sub><sup>+</sup> displayed in Fig. 4.10 and the structure with the brown sodium atom removed. Each system was used to generate half of the data points. These data points were generated by performing a random sampling along the moving direction shown in Fig. 4.10 and further displacement was added according to a Gaussian distribution with a standard deviation of 0.05 Å to sufficiently sample the PES in the region of interest.

For the data set of Au<sub>2</sub>-MgO/Al-doped Au<sub>2</sub>-MgO, there are two different optimized geometries of the Au<sub>2</sub> on the unrelaxed ideal MgO and the Al-doped MgO slabs. These geometries are separated into wetting and non-wetting configurations as illustrated in Fig. 4.14. This way, a total of four different geometries can be obtained by permuting the wetting and non-wetting geometries of the Au dimer with the unrelaxed Al-doped and undoped MgO surfaces. The data generation for each geometry is similar to the NaCl system and the standard deviation for the substrate and gold dimer were chosen to be 0.02 Å and 0.1 Å, respectively. The total number of data points for the NaCl cluster and Au<sub>2</sub>-MgO system is 5000 while the carbon chain and Ag trimer contain 10019 and 11013 data points, respectively.

The data set for demonstrating the improvement achieved by the ee4G-HDNNP consists of Na<sub>n</sub>Cl<sub>n</sub>/Na<sub>n</sub>Cl<sub>n+1</sub><sup>-</sup> with  $n = 16, 24$  and the generation of the data set is divided into two stages. The first stage was to generate high energy structures by performing BOMD simulations in the NVT ensemble for 10 structures with  $n = 16$  and 5 structures

with  $n = 24$  per each charge state at 1000 K with 5000 steps and one trajectory snapshot was taken every five time steps and included in the data set. The step size for all BOMD simulations was set to 1.0 fs. All these initial structures provided by Prof. Dr. Stefan Goedecker were obtained from minima hopping using BigDFT [150] and then re-optimized with FHIaims up to the force threshold of 0.01 eV/Å. Apart from that, the trajectory paths during the geometry relaxation were also added to the data set to have configurations close to the equilibrium structures.

The second stage was to explore the extrapolated structures that were not well sampled in the low temperature region by running MD simulations driven by the preliminary PES with a time step of 0.5 fs to achieve relatively stable MD simulations. Moreover, initial minimum geometries were generated from the Coulomb Lennard Jones empirical force field [151] using the ABCluster program [152], which performs global optimization of clusters based on the artificial bee colony algorithm [153]. Consecutively, these structures were optimized with the preliminary HDNNP. If the optimized geometry exhibits a large structural deviation indicated by performing not less than 10 geometry optimization steps when subjecting the HDNNP-optimized structures to DFT-optimized geometries, the structures will be also included in the data set. The total number of data points including both stages is 33592.

### 3.3 Construction of Neural Network Potentials

All HDNNPs reported in this thesis were constructed using the neural network potential package RuNNer [154–156]. ACSFs were utilized to describe the atomic environment within a cutoff radius, which was set to 8–12 Bohr depending on the system. The same parameters of the ACSFs and the same ANN architectures for a given system were applied to construct different generations of HDNNPs for a fair comparison. The cutoff function is chosen to be the hyperbolic tangent (see Eq. 2.28) and the functional form of radial and angular symmetry functions is given in Eq. 2.25 and Eq. 2.26, respectively. The values of ACSFs are scaled and centered by the following expression:

$$G'_i = \frac{G_i - G_{i,\text{mean}}}{G_{i,\text{max}} - G_{i,\text{min}}} \quad , \quad (3.1)$$

where  $G_{i,\text{max}}$  and  $G_{i,\text{min}}$  denote the maximum and minimum value of  $G_i$  given in the training set.  $G_{i,\text{mean}}$  is the average of all values of  $G_i$  calculated in the training set. Such treatment prevents extreme input values for the forward propagation in the ANNs, which improves the quality of the fit. The parameters and cutoff radii of the ACSFs for all systems are provided in the Appendix, Sec. A.1.

The ANNs used in all testing systems are composed of an input layer with a number of nodes equal to the number of ACSFs with possible other descriptors for the respective

element depending on the generations of HDNNPs, two hidden layers with 15 hidden neurons for each layer, and an output layer with an output neuron, which is either the atomic energy or the electronegativity. 90% of the reference data was taken for training the HDNNPs, while the remaining 10% of the data points were used as an independent test set to validate the reliability of the constructed PESs and identify possible over-fitting. Both energies and forces were used for the training of short-range ANNs. To accelerate the process of the training, only 2.5 % of the force component were randomly chosen in each epoch for training.

Furthermore, short-range Coulombic interactions were screened using Eq. 2.37 to facilitate the fitting of the short-range energies and forces. The inner spatial cutoff that removes all electrostatic interactions was set to 1.69-2.54 Å depending on the model system while the outer spatial cutoff that takes the full electrostatic contributions into account was set to the cutoff radius used in ACSFs respectively.

The ANN weights were first randomly initialized between  $-1.0$  and  $1.0$ , then further optimized employing the Nguyen-Widrow scheme [157] to ensure that there were no unrealistically large values to mitigate the risk of an exploding gradient during training. In addition, the initial error of the potentials was reduced by a preconditioning scheme, which adjusted the weights connected between the last hidden layer and the output layer so that the initial model predicted the same average and standard deviation of the atomic energies as calculated from the training set. Such treatment for the initialization of the weights was essential to provide a good starting point for searching the minimum of the high-dimensional loss function during the optimizations, which could significantly reduce the fitting error.

The weights of all ANNs were adjusted to minimize the error of training energies, forces and charges using the global, adaptive, extended Kalman filter. The parameters of the Kalman Filter were set to  $\lambda = 0.98$  and  $\nu = 0.9987$ . The early stopping algorithm was applied to detect the overfitting of the potentials by observing the error in the test set, which slightly increase after already reaching a minimum while the error of training error is further reduced after certain training epochs. All details of the training process and validation strategies for constructing HDNNPs in general can be found in recent reviews [155, 156].

### 3.4 Settings of Minima Hopping

The parameters for minima hopping explained in Sec. 2.3.4 were set to  $\alpha_1 = 0.9$ ,  $\alpha_2 = 1.1$ ,  $\beta_1 = 1.1$ ,  $\beta_2 = 1.1$ ,  $\beta_3 = 0.909$ , and  $E_{\text{diff}} = 2 \times 10^{-3}$  Ha. Some modifications for the algorithm were made in order to increase the stability of the simulations. The safety threshold for high temperature was set to 1000 K. If the temperature is higher than the safety threshold and new minima are not found, the number of time steps is increased by

a factor of 2 until the number of time step is larger than the maximum of number of time steps  $n_{\max} = 6400$ . The temperature is increased after  $n > n_{\max}$  if no minimum can be found. Apart from that, the possibility that minima are accepted is increased by taking the absolute value of the energy difference between the current minimum and past minimum and comparing to the acceptance threshold  $E_{\text{diff}}$ .

Such modifications can effectively avoid unrealistically high temperatures during the MD simulations in the microcanonical (NVE) ensemble, to prevent the collapse of clusters caused by the excessively large repulsive forces. Moreover, the minimum temperature and number of time step were set to 500 K and 100 during the simulation to make the simulations more efficient. Once a minimum is accepted, the temperature and number of time steps are reduced by a factor of 0.5 if the temperature is above the safety threshold and the number of time steps is greater than the initial number of time step. The initial number of time step and temperature during the MD simulations were 100 and 100K, respectively. A smaller step size of 0.5 fs was used for performing stable MD simulations. The force threshold for the geometry relaxation was set to 0.01 eV/Å after MD simulations. All geometry optimizations driven by HDNNPs were performed using a gradient descent algorithm. Softening of velocities was used to ensure that the structure tends to go towards low-curvature directions in PESs. The softening parameters  $d$  and  $\alpha$  were set to 0.1 and 0.015, respectively. The number of iterations for softening was 40 and more detailed information on velocity softening can be found in Ref. [158].



## Part II

# Results and Discussion



# Chapter 4

## Fourth-Generation HDNNP

### 4.1 Method

After giving a concise overview of 2G-HDNNP, 3G-HDNNP and CENT including their strengths and limitations in chapter 2, a novel model, namely the fourth-generation high-dimensional neural network potential (4G-HDNNP) [34], is proposed. The model is inspired by combining the flexible short-range energy in 2G-HDNNP, and the accurate description of global charge distributions in CENT with two essential modifications. First, the training part in CENT is reformulated so that the predicted atomic charges are physical and these charges are used to calculate the electrostatic energies and forces. Second, the architecture of short-range ANNs in 2G-HDNNP is modified such that the model can include additional information, i.e., the atomic charges, to describe non-local effects.

The 4G-HDNNP is able to capture long-range charge transfer and describe local bonding due to the global changes in the electronic structure. This novel method is generally applicable to both ionic and covalent systems. The 4G-HDNNP is a two-step approach, which consists of two different sets of ANNs for the non-local long-range electrostatic part and the short-range part, respectively. These two sets of ANNs are used to calculate electrostatic  $E_{\text{elec}}$  and short-range  $E_{\text{short}}$  contributions, yielding the total energy of the system liked in 3G-HDNNPs (i.e.,  $E_{\text{total}} = E_{\text{elec}} + E_{\text{short}}$ ). The general structure of a 4G-HDNNP for a binary system is shown in Fig. 4.1. The framework and technical details of the 4G-HDNNP are presented in the following subsections.

#### 4.1.1 Non-Local Long-Range Electrostatic Part

##### 4.1.1.1 Charge and Energy Calculations

The goal of the non-local electrostatic part is to reproduce the reference charges through a charge equilibration (Qeq) scheme that relies on environment-dependent atomic elec-

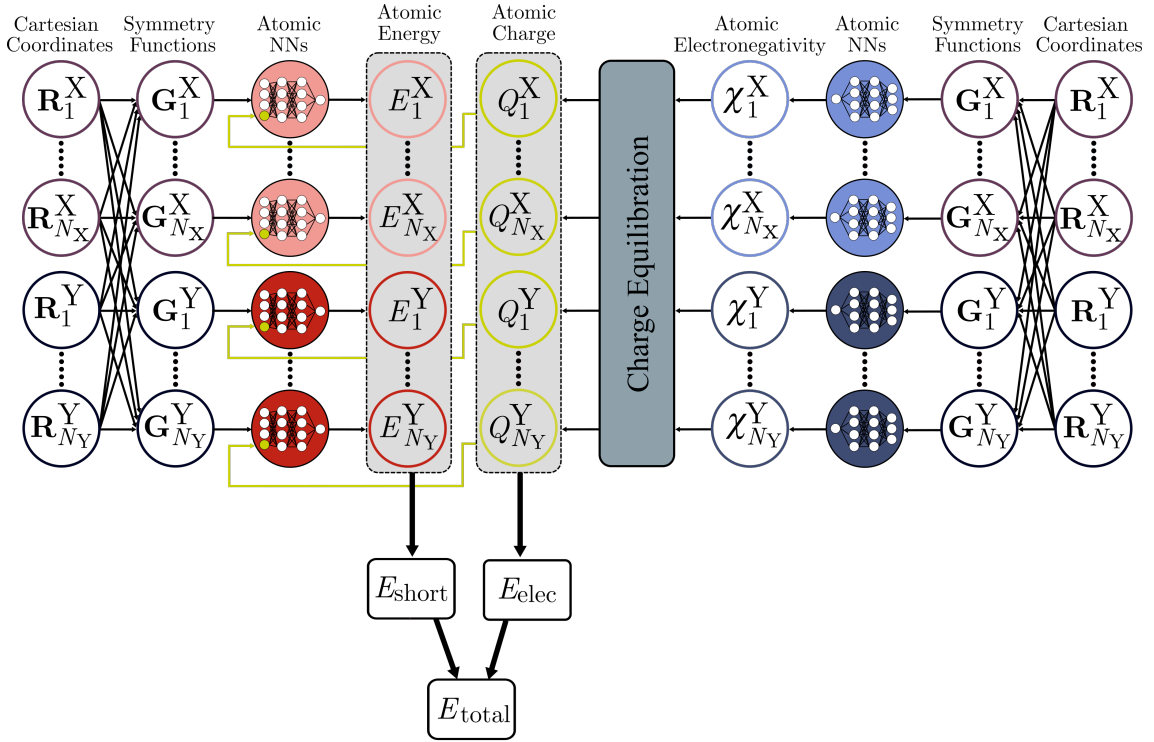


**Fig. 4.1:** A schematic structure of a 4G-HDNNP for a binary system containing  $N_X$  atoms of element X and  $N_Y$  of element Y. In the long-range electrostatic part, a set of Cartesian coordinates  $\mathbf{R}_i$  is transformed into atom-centered symmetry functions  $\{G_i\}$ , which serves as input for atomic neural networks (right) to predict environment-dependent electronegativities  $\chi_i$ . The partial charges  $Q_i$  are then calculated according to a charge equilibration scheme. These charges are used to compute the long-range electrostatic energy  $E_{\text{elec}}$ . In the short-range part, not only symmetry functions  $\{G_i\}$  but also atomic charges  $Q_i$  are fed into the atomic neural networks (left) to determine the short-range atomic energies  $E_i$ . The structure of 4G-HDNNP and corresponding implementations are jointly developed with Jonas Finkler. Reprinted (adapted) with permission from Ref. [79]. Copyright 2021 American Chemical Society.

tronegativities. In this case, the electronegativities are trained such that the partial charges are redistributed in an optimal way to reproduce reference charges according to the Qeq scheme. The Qeq scheme redistributes the atomic charges by minimizing the following energy expression with respect to atomic charges

$$E_{\text{Qeq}} = E_{\text{elec}} + \sum_{i=1}^{N_{\text{atoms}}} \left( \chi_i Q_i + \frac{1}{2} \eta_i Q_i^2 \right) \quad , \quad (4.1)$$

where  $E_{\text{elec}}$  is the electrostatic energy calculated using Gaussian charges and  $\eta_i$  represents the element-dependent hardness. It is noted that  $\eta_i$  is independent of the local environment and is also optimized for each element during the training. The atomic electronegativities  $\chi_i$  are assumed to be local physical properties that are expressed as a function of the chemical environment using ANNs. The atomic environments are represented by ACSFs to ensure that the resulting electronegativities are invariant under translation, rotation, and permutation of the atoms. The expression for the electrostatic energy  $E_{\text{elec}}$  differs for periodic and non-periodic systems as presented in the following subsections.

### Non-Periodic Systems

The long-range electrostatic energy in 3G-HDNNPs is calculated using point charges. Due to the function form of  $\frac{1}{r}$ , the electrostatic interaction becomes unrealistically large, when two charged atoms move closer. To address this problem in the framework of 4G-HDNNPs, the charge densities are assumed to be Gaussian distributed. The general expression for the electrostatic energy of a non-periodic system based on Gaussian charges is given by Coulomb's law as

$$E_{\text{elec}} = \sum_{i>j}^{N_{\text{atoms}}} \frac{\text{erf}\left(\frac{R_{ij}}{\sqrt{2}\gamma_{ij}}\right)}{R_{ij}} Q_i Q_j + \sum_{i=1}^{N_{\text{atoms}}} \frac{Q_i^2}{2\sigma_i\sqrt{\pi}} \quad \text{with } \gamma_{ij} = \sqrt{\sigma_i^2 + \sigma_j^2} \quad , \quad (4.2)$$

where the first term represents the pairwise electrostatic interactions between the Gaussian charge on atom  $i$  and  $j$ . The second term is the self-interaction of the Gaussian charge densities. Here  $\sigma_i$  denotes the element-dependent width of the Gaussian charge densities, which were set to the corresponding covalent radii for all potentials reported in this thesis. In this way, the problem of unrealistically large electrostatic energy can be alleviated by the error function in Eq. 4.2.

The implicit dependence of  $Q_i$  can be obtained by minimizing the energy expression of Eq. 4.1 with respect to the atomic charges  $Q_i$  under the constraint that the sum of all partial charges must be equal to the total charge of the system. This constrained minimization problem can be solved by applying a Lagrange multiplier  $\lambda$

$$\mathcal{L}(\{Q_i\}, \lambda) = E_{\text{Qeq}} - \lambda \left( Q_{\text{total}} - \sum_{i=1}^{N_{\text{atoms}}} Q_i \right) \quad (4.3)$$

and by setting the partial derivative  $\frac{\partial \mathcal{L}}{\partial Q_i} = 0$ ,

$$\frac{\partial \mathcal{L}}{\partial Q_i} = 0, \forall i = 1, \dots, N_{\text{atoms}} \implies \sum_{j=1}^{N_{\text{atoms}}} A_{ij} Q_j + \chi_i + \lambda = 0 \quad , \quad (4.4)$$

where the corresponding elements  $A_{ij}$  of a  $N_{\text{atoms}}$  by  $N_{\text{atoms}}$  matrix  $\mathbf{A}$  are given by:

$$A_{ij} = \begin{cases} \eta_i + \frac{1}{\sigma_i \sqrt{\pi}}, & \text{if } i = j \\ \frac{\text{erf}\left(\frac{R_{ij}}{\sqrt{2}\gamma_{ij}}\right)}{R_{ij}}, & \text{otherwise} \end{cases} \quad (4.5)$$

With this constraint, the equilibrated charges can be obtained by solving the following set of linear equations:

$$\left( \begin{array}{c|c} \mathbf{A} & \begin{pmatrix} 1 \\ \vdots \\ 1 \end{pmatrix} \\ \hline 1 & \dots & 1 & 0 \end{array} \right) \begin{pmatrix} Q_1 \\ \vdots \\ Q_{N_{\text{atoms}}} \\ \lambda \end{pmatrix} = \begin{pmatrix} -\chi_1 \\ \vdots \\ -\chi_{N_{\text{atoms}}} \\ Q_{\text{total}} \end{pmatrix} \quad (4.6)$$

In principle, solving a set of linear equations scales  $O(N^3)$  with the number of atoms in standard algorithms. Although this still can be efficiently solved for systems containing up to around 10,000 atoms in a few seconds with highly optimized libraries such as Lapack [94] or ScaLAPACK [95], it can pose a bottle neck for much larger systems. Efficient iterative solvers [159] have been proposed to significantly reduce the computational time for solving such systems of linear equations by applying incomplete factorization and sparse inverse (SAI) preconditioners [160]. The detailed difference of charge calculations between CENT and 4G-HDNNP is given in the last part of Sec. 4.1.1.1.

## Periodic Systems

The charge calculations for periodic systems based on the Qeq scheme is similar to the non-periodic case. The main difference between them is the calculation of the matrix  $\mathbf{A}$ . In the periodic case, the Ewald Summation [131] is used to calculate  $E_{\text{elec}}$ . The general idea of the Ewald Summation is to place the Gaussian distributed charge density of the opposite sign on each point charge. The remaining electrostatic energy is calculated in real space  $E_{\text{real}}$ . In order to obtain the desired total energy of the point charges, the electrostatic energy of the compensated Gaussian charge density of the same sign is also included, which can be efficiently computed in reciprocal space  $E_{\text{recip}}$  using Fourier transform. An extra term  $E_{\text{self}}$  is needed to cancel the self-interaction of the Gaussian charge density. In this way, the calculation of a conditionally convergent direct summation of  $\frac{1}{r}$  can be replaced by just calculating two rapidly convergent summations and a constant term. The energy expression of the point charges  $E_{\text{pc,elec}}$  is written as:

$$E_{\text{pc,elec}} = E_{\text{real}} + E_{\text{recip}} + E_{\text{self}} \quad (4.7)$$

with

$$\begin{aligned}
 E_{\text{real}} &= \frac{1}{2} \sum_{\mathbf{n}} \sum_{i=1}^{N_{\text{atoms}}} \sum_{j=1}^{N_{\text{atoms}}}{}' Q_i Q_j \frac{\text{erfc}\left(\frac{|R_{ij} + \mathbf{nL}|}{\sqrt{2}\beta}\right)}{|R_{ij} + \mathbf{nL}|} \quad , \\
 E_{\text{recip}} &= \frac{2\pi}{V} \sum_{\mathbf{k} \neq 0} \frac{e\left(-\frac{\beta^2 \mathbf{k}^2}{2}\right)}{|\mathbf{k}|^2} |S(\mathbf{k})|^2 \quad \text{with } S(\mathbf{k}) = \sum_{i=1}^{N_{\text{atoms}}} Q_i e^{i\mathbf{k} \cdot \mathbf{r}_i} \quad , \\
 E_{\text{self}} &= - \sum_{i=1}^{N_{\text{atoms}}} \frac{Q_i^2}{\sqrt{2\pi}\beta} \quad .
 \end{aligned}$$

Here,  $\beta$  defines the width of Gaussian charge density, which controls the convergence of the two summations in the real and reciprocal space.  $V$  and  $\mathbf{L}$  represent the volume and a set of lattice vectors of the unit cell, respectively. The symbol ' means that the term  $j = i$  in the summation is not included if and only if  $\mathbf{n} = 0$ . The vectors  $\mathbf{n}$  create a series of replicated unit cells along the x, y and z-direction.  $\mathbf{k}$  is a set of reciprocal lattice vectors.

$E_{\text{real}}$  is computed by summing the pairwise electrostatic contribution over other atoms for the atom  $i$  within the spatial cutoff in real space.  $E_{\text{recip}}$  is calculated by summing over all reciprocal lattice points within the cutoff of the reciprocal space represented by reciprocal lattice vector  $\mathbf{k}$ , which can be written as a linear combination of three primitive translational reciprocal lattice vectors.  $E_{\text{self}}$  is obtained by solving the Poisson equation for a Gaussian charge density centered at the origin of each point charge. Detailed deviations of the Ewald Summation can be found in the literature [131, 161].

The convergence of the Ewald summation mainly relies on three parameters including  $\beta$ ,  $R_{\text{c,real}}$  and  $R_{\text{c,recip}}$ . The last two terms denote the cutoff used in real and reciprocal spaces, which determine the maximum number of replicated image cells in each space. Typically, the Ewald summation scales  $O(N^2)$  with the number of atoms  $N$  and therefore can be very computationally intensive when a system contains more than a few thousand atoms. Still, the computational scaling can be reduced to  $O(N^{1.5})$  by choosing an optimal setting of  $\beta$ ,  $R_{\text{c,real}}$  and  $R_{\text{c,recip}}$  [162] and the parameter values are given by the following equations:

$$\begin{aligned}
 \beta &= \left( \frac{(V^2/N_{\text{atoms}})^{\frac{1}{6}}}{\sqrt{2\pi}} \right) \quad , \\
 R_{\text{c,real}} &= \sqrt{2}\beta \sqrt{-\log \epsilon_{\text{prec}}} \quad , \\
 R_{\text{c,recip}} &= \frac{\sqrt{2} \sqrt{-\log \epsilon_{\text{prec}}}}{\beta} \quad .
 \end{aligned} \tag{4.8}$$

Here, the  $V$  denotes the volume of the unit cell and  $\epsilon_{\text{prec}}$  defines the convergence of the sum, which is typically set to  $10^{-6}$ . Apart from the standard Ewald summation, other much more efficient algorithms such as the fast multipole [163] and particle mesh Ewald [164] have been developed. These algorithms scale  $O(N \log N)$  with the number of atoms  $N$ , which significantly reduces the computational time in comparison with standard

Ewald summation, but these methods have not been used in the present work.

The Ewald summation of point charges is easily extended to Gaussian distributed charges by adding the following terms which account for the different interactions in the real space part and express the self-interaction of Gaussian charges [165],

$$E_{\text{Gauss,elec}} = E_{\text{pc,elec}} - \frac{1}{2} \sum_{i=1}^{N_{\text{atoms}}} \sum_{j=1}^{N_{\text{atoms}}} Q_i Q_j \frac{\text{erfc}\left(\frac{|R_{ij} + \mathbf{nL}|}{\sqrt{2}\gamma_{ij}}\right)}{|R_{ij} + \mathbf{nL}|} + \sum_{i=1}^{N_{\text{atoms}}} \frac{Q_i^2}{2\sqrt{\pi}\sigma_i}. \quad (4.9)$$

By following the same procedure to calculate the equilibrated charges by minimizing  $E_{\text{Qeq}}$  with respect to  $Q_i$  that was presented for non-periodic systems, a set of linear equations like Eq. 4.6 are established. The difference lies in the matrix elements  $A_{ij}$ , which are given by:

$$A_{ij} = \begin{cases} \eta_i + \left(\frac{-\sqrt{2}}{\sqrt{\pi}\beta} + \frac{1}{\sigma_i\sqrt{\pi}}\right) + \frac{4\pi}{V} \sum_{\mathbf{k} \neq 0} \frac{e^{-\frac{\beta^2|\mathbf{k}|^2}{2}}}{|\mathbf{k}|^2} + \sum_{\mathbf{n}} \left( \frac{\text{erfc}\left(\frac{|\mathbf{nL}|}{\sqrt{2}\beta}\right) - \text{erfc}\left(\frac{|\mathbf{nL}|}{2\sigma_i}\right)}{|\mathbf{nL}|} \right), & \text{if } i = j \\ \sum_{\mathbf{n}} \frac{\text{erfc}\left(\frac{|R_{ij} + \mathbf{nL}|}{\sqrt{2}\beta}\right) - \text{erfc}\left(\frac{|R_{ij} + \mathbf{nL}|}{\sqrt{2}\gamma_{ij}}\right)}{|R_{ij} + \mathbf{nL}|} + \frac{4\pi}{V} \sum_{\mathbf{k} \neq 0} \cos(\mathbf{k} \cdot (R_{ij} + \mathbf{nL})) \frac{e^{-\frac{\beta^2|\mathbf{k}|^2}{2}}}{|\mathbf{k}|^2}, & \text{otherwise} \end{cases} \quad (4.10)$$

### Comparison to CENT

The calculation of charges and electrostatic energies for non-periodic and periodic systems in CENT and 4G-HDNNP is basically the same except the energy expression for the minimization (see Eq. 2.41 and Eq. 4.1 for the non-periodic case in Eq.4.2). The energy of an isolated atom  $E_i^0$  is removed in Eq. 4.1 and  $\sigma_i$  in 4G-HDNNP is equal to  $\frac{\alpha_i}{\sqrt{2}}$  in Eq. 2.41. The main difference between 4G-HDNNP and CENT is the training part. In CENT, the electronegativities predicted by ANNs are trained to minimize the error between the predicted total energy calculated and reference total energy. Consequently, the atomic charges obtained from CENT have no direct physical meaning. In contrast to that, in 4G-HDNNP the electronegativities are adjusted to reproduce the reference charges, which are physical and can be used to describe local bonding caused by global changes in the electronic structure.

#### 4.1.1.2 Training Phase

In the training process, the ANN weights that predict the environment-dependent electronegativities and element-dependent hardnesses are optimized to minimize the loss

function

$$\Gamma_{\text{charge}} = \frac{1}{N_{\text{atoms}}} \sum_{i=1}^{N_{\text{atoms}}} (Q_{i,\text{ref}} - Q_{i,4\text{G-HDNNP}})^2, \quad (4.11)$$

where  $Q_{i,\text{ref}}$  and  $Q_{i,4\text{G-HDNNP}}$  are the reference charges and the 4G-HDNNP charges, respectively. All free parameters including different ANN weights and hardness values are both optimized simultaneously using a global, adaptive and extended Kalman filter [166], which is well suited for highly non-linear regression problems. The optimization of weights and hardnesses requires the following derivatives using the chain rule:

$$\frac{\partial \Gamma_{\text{charge}}}{\partial \eta_j} = \sum_{i=1}^{N_{\text{atoms}}} \frac{\partial \Gamma_{\text{charge}}}{\partial Q_i} \cdot \frac{\partial Q_i}{\partial \eta_j}, \quad (4.12)$$

$$\frac{\partial \Gamma_{\text{charge}}}{\partial W_k} = \sum_{i=1}^{N_{\text{atoms}}} \sum_{j=1}^{N_{\text{atoms}}} \frac{\partial \Gamma_{\text{charge}}}{\partial Q_i} \cdot \frac{\partial Q_i}{\partial \chi_j} \cdot \frac{\partial \chi_j}{\partial W_k}, \quad (4.13)$$

where  $\frac{\partial \Gamma_{\text{charge}}}{\partial \eta_j}$  and  $\frac{\partial \Gamma_{\text{charge}}}{\partial W_k}$  denote the partial derivative of the loss function with respect to the atomic hardness  $\eta_j$  and weight  $W_k$ , respectively.  $\frac{\partial \Gamma_{\text{charge}}}{\partial Q_i}$  can be derived from Eq. 4.11 while  $\frac{\partial Q_i}{\partial \eta_j}$  can be obtained by taking the partial derivative of Eq. 4.6 with respect to the atomic hardness  $\eta_j$  and solving the respective system of linear equations

$$\left( \begin{array}{c|c} \mathbf{A} & \begin{matrix} 1 \\ \vdots \\ 1 \end{matrix} \\ \hline 1 & \dots & 1 & 0 \end{array} \right) \begin{pmatrix} \frac{\partial Q_1}{\partial \eta_j} \\ \vdots \\ \frac{\partial Q_{N_{\text{atoms}}}}{\partial \eta_j} \\ \lambda \end{pmatrix} = \begin{pmatrix} -\delta_{1,j} Q_1 \\ \vdots \\ -\delta_{N_{\text{atoms}},j} Q_{N_{\text{atoms}}} \\ 0 \end{pmatrix} \quad (4.14)$$

and  $\frac{\partial Q_i}{\partial \chi_j}$  can also be computed in a similar way

$$\left( \begin{array}{c|c} \mathbf{A} & \begin{matrix} 1 \\ \vdots \\ 1 \end{matrix} \\ \hline 1 & \dots & 1 & 0 \end{array} \right) \begin{pmatrix} \frac{\partial Q_1}{\partial \chi_j} \\ \vdots \\ \frac{\partial Q_{N_{\text{atoms}}}}{\partial \chi_j} \\ \lambda \end{pmatrix} = \begin{pmatrix} \delta_{1,j} \\ \vdots \\ \delta_{N_{\text{atoms}},j} \\ 0 \end{pmatrix}, \quad (4.15)$$

where  $\delta$  stands for the Kronecker delta meaning that  $\delta_{ij}$  is equal to 1 if  $i = j$ , and 0 otherwise. The  $\frac{\partial \chi_j}{\partial W_k}$  are evaluated through the back-propagation in ANNs. All these derivatives are accumulated by looping over all atoms in every training structure and utilized to update the weights and hardnesses through the Kalman filter.

### 4.1.1.3 Force Calculations

The electrostatic force acting on the atom  $k$  with respect to the coordinate  $R_{k,\alpha}$  can be calculated by

$$F_{k,\alpha}^{\text{elec}} = -\frac{\partial E_{\text{elec}}}{\partial R_{k,\alpha}} - \sum_{i=1}^{N_{\text{atoms}}} \frac{\partial E_{\text{elec}}}{\partial Q_i} \frac{\partial Q_i}{\partial R_{k,\alpha}} \quad (4.16)$$

Here, the partial derivative of the electrostatic energy with respect to the atomic charge  $Q_i$  is not equal to zero, which is different from CENT in Eq. 2.45. As a consequence, the calculations of the partial derivative  $\frac{\partial Q_i}{\partial R_{k,\alpha}}$  are required to obtain the force contributions. These quantities can be derived from Eq. 4.6:

$$\left( \begin{array}{c|c} \mathbf{A} & \begin{matrix} 1 \\ \vdots \\ 1 \end{matrix} \\ \hline 1 & \dots & 1 & 0 \end{array} \right) \begin{pmatrix} \frac{\partial Q_1}{\partial R_{k,\alpha}} \\ \vdots \\ \frac{\partial Q_{N_{\text{atoms}}}}{\partial R_{k,\alpha}} \\ \lambda \end{pmatrix} = \begin{pmatrix} \frac{\partial \chi_1}{\partial R_{k,\alpha}} \\ \vdots \\ \frac{\partial \chi_{N_{\text{atoms}}}}{\partial R_{k,\alpha}} \\ 0 \end{pmatrix} - \left( \begin{array}{c|c} \frac{\partial \mathbf{A}}{\partial R_{k,\alpha}} & \begin{matrix} 1 \\ \vdots \\ 1 \end{matrix} \\ \hline 1 & \dots & 1 & 0 \end{array} \right) \begin{pmatrix} Q_1 \\ \vdots \\ Q_{N_{\text{atoms}}} \\ 0 \end{pmatrix} \quad (4.17)$$

However, the calculation of  $\frac{\partial Q_i}{\partial R_{k,\alpha}}$  for all atomic coordinates typically involves solving  $3N_{\text{atoms}}$  systems of linear equations. This is very computationally demanding for systems with more than thousands of atoms. An efficient trick suggested by Jonas Finkler, which is exploiting a method proposed from Ref. [167], can be used to address the problem by only solving the linear equations once instead of many times. For simplicity, Eq. 4.6 is rewritten to

$$\mathbf{A}'\mathbf{Q}' = \mathbf{b} \quad (4.18)$$

with

$$\mathbf{A}' = \left( \begin{array}{c|c} \mathbf{A} & \begin{matrix} 1 \\ \vdots \\ 1 \end{matrix} \\ \hline 1 & \dots & 1 & 0 \end{array} \right), \quad \mathbf{Q}' = \begin{pmatrix} Q_1 \\ \vdots \\ Q_{N_{\text{atoms}}} \\ \lambda \end{pmatrix} \quad \text{and} \quad \mathbf{b} = \begin{pmatrix} \chi_1 \\ \vdots \\ \chi_{N_{\text{atoms}}} \\ Q_{\text{total}} \end{pmatrix} \quad (4.19)$$

An auxiliary function  $\mathcal{L}$  is defined as:

$$\mathcal{L} = E_{\text{elec}} + \sum_{i=1}^{N_{\text{atoms}}+1} \Lambda_i \left( \sum_{j=1}^{N_{\text{atoms}}+1} A'_{ij} Q'_j - b_i \right), \quad (4.20)$$

where  $\sum_{j=1}^{N_{\text{atoms}}} (A'_{ij} Q'_j - b_i)$  is obtained by subtracting  $\mathbf{b}$  on both sides in Eq. 4.18. These terms are always equal to zero and therefore  $\mathcal{L}$  is equal to  $E_{\text{elec}}$ . The parameter  $\Lambda_i$  is

chosen such that the partial derivative  $\frac{\partial \mathcal{L}}{\partial Q'_i}$  is equal to zero.

$$\frac{\partial \mathcal{L}}{\partial Q'_i} = \frac{\partial E_{\text{elec}}}{\partial Q'_i} + \sum_{l=1}^{N_{\text{atoms}}+1} A'_{il} \Lambda_l = 0 \quad . \quad (4.21)$$

Hence,  $\{\Lambda_i\}$  can be obtained by solving the following system of linear equations:

$$\left( \begin{array}{c|c} \mathbf{A} & \begin{matrix} 1 \\ \vdots \\ 1 \end{matrix} \\ \hline 1 & \dots & 1 & 0 \end{array} \right) \begin{pmatrix} \Lambda_1 \\ \vdots \\ \Lambda_{N_{\text{atoms}}} \\ \Lambda_{N_{\text{atoms}}+1} \end{pmatrix} = \begin{pmatrix} -\frac{\partial E_{\text{elec}}}{\partial Q_1} \\ \vdots \\ -\frac{\partial E_{\text{elec}}}{\partial Q_{N_{\text{atoms}}}} \\ 0 \end{pmatrix} \quad . \quad (4.22)$$

Here,  $\mathbf{A}$  is a symmetric matrix. Now the partial derivative  $\frac{\partial Q'_i}{\partial R_{k,\alpha}}$  can be calculated by taking the partial derivative of Eq. 4.20 with respect to  $R_{k,\alpha}$

$$\begin{aligned} \frac{dE_{\text{elec}}}{dR_{k,\alpha}} &= \frac{\partial \mathcal{L}}{\partial R_{k,\alpha}} \\ &= \frac{\partial E_{\text{elec}}}{\partial R_{k,\alpha}} + \sum_{j=1}^{N_{\text{atoms}}+1} \frac{\partial E_{\text{elec}}}{\partial Q'_j} \cdot \frac{\partial Q'_j}{\partial R_{k,\alpha}} \\ &+ \sum_{i=1}^{N_{\text{atoms}}+1} \Lambda_i \left( \sum_{j=1}^{N_{\text{atoms}}+1} \left( \frac{\partial A'_{ij}}{\partial R_{k,\alpha}} Q'_j + A'_{ij} \frac{\partial Q'_j}{\partial R_{k,\alpha}} \right) - \frac{\partial b_i}{\partial R_{k,\alpha}} \right) \quad . \quad (4.23) \end{aligned}$$

Rearranging the equations yields

$$\begin{aligned} \frac{dE_{\text{elec}}}{dR_{k,\alpha}} &= \frac{\partial E_{\text{elec}}}{\partial R_{k,\alpha}} + \sum_{j=1}^{N_{\text{atoms}}+1} \left( \frac{\partial E_{\text{elec}}}{\partial Q'_j} + \sum_{i=1}^{N_{\text{atoms}}+1} A'_{ij} \Lambda_i \right) \frac{\partial Q'_j}{\partial R_{k,\alpha}} \\ &+ \sum_{i=1}^{N_{\text{atoms}}+1} \Lambda_i \left( \sum_{j=1}^{N_{\text{atoms}}+1} \frac{\partial A'_{ij}}{\partial R_{k,\alpha}} Q'_j - \frac{\partial b_i}{\partial R_{k,\alpha}} \right) \quad . \quad (4.24) \end{aligned}$$

The second term vanishes due to Eq. 4.21, which leads to the resulting expression

$$\frac{dE_{\text{elec}}}{dR_{k,\alpha}} = \frac{\partial E_{\text{elec}}}{\partial R_{k,\alpha}} + \sum_{i=1}^{N_{\text{atoms}}+1} \Lambda_i \left( \sum_{j=1}^{N_{\text{atoms}}+1} \frac{\partial A'_{ij}}{\partial R_{k,\alpha}} Q'_j - \frac{\partial b_i}{\partial R_{k,\alpha}} \right) \quad . \quad (4.25)$$

The  $\frac{\partial E_{\text{elec}}}{\partial R_{k,\alpha}}$  is the usual electrostatic force according to Coulomb's law. The  $\frac{\partial A'_{ij}}{\partial R_{k,\alpha}}$  can be calculated analytically and  $\frac{\partial b_i}{\partial R_{k,\alpha}}$  depends on the employed ACSFs and the architecture of ANNs. Once the  $\{\Lambda_i\}$  is calculated by solving a set of linear equations in Eq. 4.22, electrostatic forces can be then calculated efficiently, which avoids solving  $3 N_{\text{atoms}}$  linear systems.

## 4.1.2 Short-Range Part

### 4.1.2.1 Energy and Force Calculations

The total energy expression of the 4G-HDNNP consists of an electrostatic and a short-range parts. Once the electrostatic energy has been calculated, the short-range energy can be obtained by removing the electrostatic part from the total energy. The expression of short-range energy is thus given by

$$E_{\text{short}} = \sum_{i=1}^{N_{\text{atoms}}} E_i(\{G_i\}, Q_i) \quad , \quad (4.26)$$

where the  $E_{\text{short}}$  is expressed as a sum of atomic energies as common in 2G-HDNNPs. An important difference to 2G-HDNNP is that the atomic energies in 4G-HDNNP do not only depend on the ACSF values describing the local atomic environments, but also on the atomic charges determined in the non-local electrostatic part (see Fig. 4.1). In this way, the atomic energy contributions enable describing physical effects caused by non-local charge transfer. The atomic force acting on the atom  $k$  with respect to the coordinate  $R_{k,\alpha}$  can be calculated analytically using the chain rule yielding the following expression:

$$\begin{aligned} F_{k,\alpha}^{\text{short}} &= -\frac{dE_{\text{short}}}{dR_{k,\alpha}} \\ &= -\left( \sum_{i=1}^{N_{\text{atoms}}} \sum_{j=1}^{N_{i,\text{sym}}} \frac{\partial E_i}{\partial G_{i,j}} \frac{\partial G_{i,j}}{\partial R_{k,\alpha}} + \sum_{i=1}^{N_{\text{atoms}}} \frac{\partial E_i}{\partial Q_i} \frac{\partial Q_i}{\partial R_{k,\alpha}} \right) \quad , \quad (4.27) \end{aligned}$$

where the  $\frac{\partial E_i}{\partial G_{i,j}}$  and  $\frac{\partial E_i}{\partial Q_i}$  are the partial derivatives of atomic energy  $E_i$  with respect to the ACSF  $G_{i,j}$  of atom  $i$  and its atomic charge  $Q_i$ , respectively. These quantities can be computed directly in neural networks, while the partial derivatives  $\frac{\partial Q_i}{\partial R_{k,\alpha}}$  are calculated from the non-local electrostatic part. Physically, the first term in Eq. 4.27 describes the force contributions due to changes of the local atomic environments represented by ACSFs as in 2G-HDNNPs, and the second term incorporates global changes in the electronic structure.

The workflow of energy and force predictions in 4G-HDNNP is as follows. The geometrical information of the structure is transformed into ACSFs. The atomic charges are then determined by the charge equilibration process using the electronegativities predicted by ANNs. These charges are used to compute the electrostatic energy using Coulomb's law and fed into short-range ANNs with ACSFs to predict the atomic energies and the corresponding short-range forces. Finally the total energy and forces of the system is equal to the sum of the short-range part and the electrostatic part.

### 4.1.2.2 Training Phase

The training procedure of the short-range part is very similar to 2G-HDNNP except for the atomic charge, which serves as additional input to the ANNs. As explained above, the target values for the short-range energies and forces can be obtained by removing the electrostatic contributions from the reference total energy and forces. The energies used for the training are binding energies, which are given by removing the sum of energies of the isolated atoms. The neural network weights are optimized to minimize the error of the loss function [16]:

$$\begin{aligned} \Gamma_{\text{short}} = & \frac{1}{N_{\text{energies}}} \sum_{i=1}^{N_{\text{energies}}} \left( \frac{E_{i,\text{ref}} - E_{i,4\text{G-HDNNP}}}{N_{\text{atoms}}} \right)^2 \\ & + \gamma \frac{1}{N_{\text{forces}}} \sum_{j=1}^{N_{\text{forces}}} (F_{i,\text{ref}} - F_{i,4\text{G-HDNNP}})^2 \end{aligned} \quad (4.28)$$

where  $E_{i,\text{ref}}$  is the reference energy and  $E_{i,4\text{G-HDNNP}}$  is the short-range energy predicted by 4G-HDNNP.  $F_{i,\text{ref}}$  and  $F_{i,4\text{G-HDNNP}}$  denote the reference and the 4G-HDNNP short-range force component. Apart from that,  $\gamma$  denotes the scaling factor for adjusting the relative importance of force accuracy for the training of ANNs. Energies and forces training requires the partial derivatives of the energies and forces with respect to neural network weights. The energy derivatives are simply calculated through back-propagation, which fully depending on the architecture of ANNs. The partial derivatives of force component  $F_{k,\alpha}$  in 4G-HDNNP with respect to the weight  $W_l$  can be derived from the following:

$$\begin{aligned} \frac{\partial F_{k,\alpha}}{\partial W_l} = & \frac{\partial}{\partial W_l} \left( - \sum_{i=1}^{N_{\text{atoms}}} \left( \sum_{j=1}^{N_{\text{sym},i}} \frac{\partial E_i}{\partial G_{i,j}} \cdot \frac{\partial G_{i,j}}{\partial R_{k,\alpha}} + \frac{\partial E_i}{\partial Q_i} \cdot \frac{\partial Q_i}{\partial R_{k,\alpha}} \right) \right) \\ = & - \sum_{i=1}^{N_{\text{atoms}}} \sum_{j=1}^{N_{\text{sym},i}} \left( \frac{\partial G_{i,j}}{\partial R_{k,\alpha}} \cdot \frac{\partial}{\partial W_l} \frac{\partial E_i}{\partial G_{i,j}} + \frac{\partial E_i}{\partial G_{i,j}} \frac{\partial}{\partial W_l} \frac{\partial G_{i,j}}{\partial R_{k,\alpha}} \right) \\ & - \sum_{i=1}^{N_{\text{atoms}}} \left( \frac{\partial Q_i}{\partial R_{k,\alpha}} \cdot \frac{\partial}{\partial W_l} \frac{\partial E_i}{\partial Q_i} + \frac{\partial E_i}{\partial Q_i} \cdot \frac{\partial}{\partial W_l} \frac{\partial Q_i}{\partial R_{k,\alpha}} \right) . \end{aligned} \quad (4.29)$$

Here, the partial derivatives  $\frac{\partial G_{i,j}}{\partial R_{k,\alpha}}$  and  $\frac{\partial Q_i}{\partial R_{k,\alpha}}$  are independent of the weights and their derivatives are thus equal to zero. Eventually Eq. 4.29 can be simplified to

$$\frac{\partial F_{k,\alpha}}{\partial W_l} = - \left( \sum_{i=1}^{N_{\text{atoms}}} \sum_{j=1}^{N_{\text{sym},i}} \frac{\partial G_{i,j}}{\partial R_{k,\alpha}} \cdot \frac{\partial}{\partial W_l} \frac{\partial E_i}{\partial G_{i,j}} + \sum_{i=1}^{N_{\text{atoms}}} \frac{\partial Q_i}{\partial R_{k,\alpha}} \cdot \frac{\partial}{\partial W_l} \frac{\partial E_i}{\partial Q_i} \right) , \quad (4.30)$$

where  $\frac{\partial}{\partial W_l} \frac{\partial E_i}{\partial G_{i,j}}$  and  $\frac{\partial}{\partial W_l} \frac{\partial E_i}{\partial Q_i}$  can be obtained from the architecture of short-range ANNs. The second term in Eq. 4.30 is additional compared to 2G-HDNNPs. It involves the partial derivatives of charges with respect to the atomic position  $\frac{\partial Q_i}{\partial R_{k,\alpha}}$ .

## 4.2 Comparisons with Local Methods for Benchmark Systems

In the following subsections, detailed comparisons between 2G-HDNNPs, 3G-HDNNPs constructed with unscaled charges (unscaled 3G-HDNNPs) and scaled charges (scaled 3G-HDNNPs), and 4G-HDNNPs in reproducing DFT results for a series of benchmark systems are presented. The learning curves of these HDNNPs are provided in Sec. A.2

### 4.2.1 Organic Molecule

The first model system is a linear organic molecule, which consists of ten sp-hybridized carbon atoms terminated by two hydrogen atoms, as displayed in Fig. 4.2. This type of molecules has been extensively investigated using ab-initio calculations [168–170], due to the increasing interest in studies of carbon materials. The protonation of the terminal carbon atom induces long-range charge transfer along the whole molecule, which changes the equilibrium structure and the total charge of the system. Such chemical interactions can be described by fourth-generation MLPs, which contain explicit information about the total charge and corresponding global charge distribution. In contrast, second- and third-generation MLPs fail to study systems with multiple charge states due to the lack of these non-local information.

To show the capabilities of the new method, 2G-, 3G- and 4G-HDNNPs are constructed using a cutoff radius  $R_c = 4.23 \text{ \AA}$  based on a data set containing both configurations generated from MD simulations and geometry optimizations. The details of data generation are given in chapter 3. Fig. 4.3 shows the correlation plots of binding energies and atomic force components obtained from 2G- and 4G-HDNNPs with respect to DFT in the training and test sets. Both potentials predict binding energies in similar agreement with DFT, while a noticeable improvement of 4G-HDNNP over 2G-HDNNP can be found in the

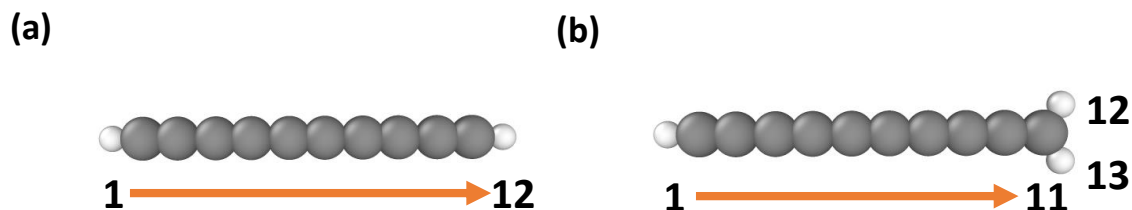


**Fig. 4.2:** DFT-optimized structures of  $C_{10}H_2$  (a) and  $C_{10}H_3^+$  (b) with atom IDs. Reprinted (adapted) with permission from Ref. [34]. Copyright 2021 Springer Nature.

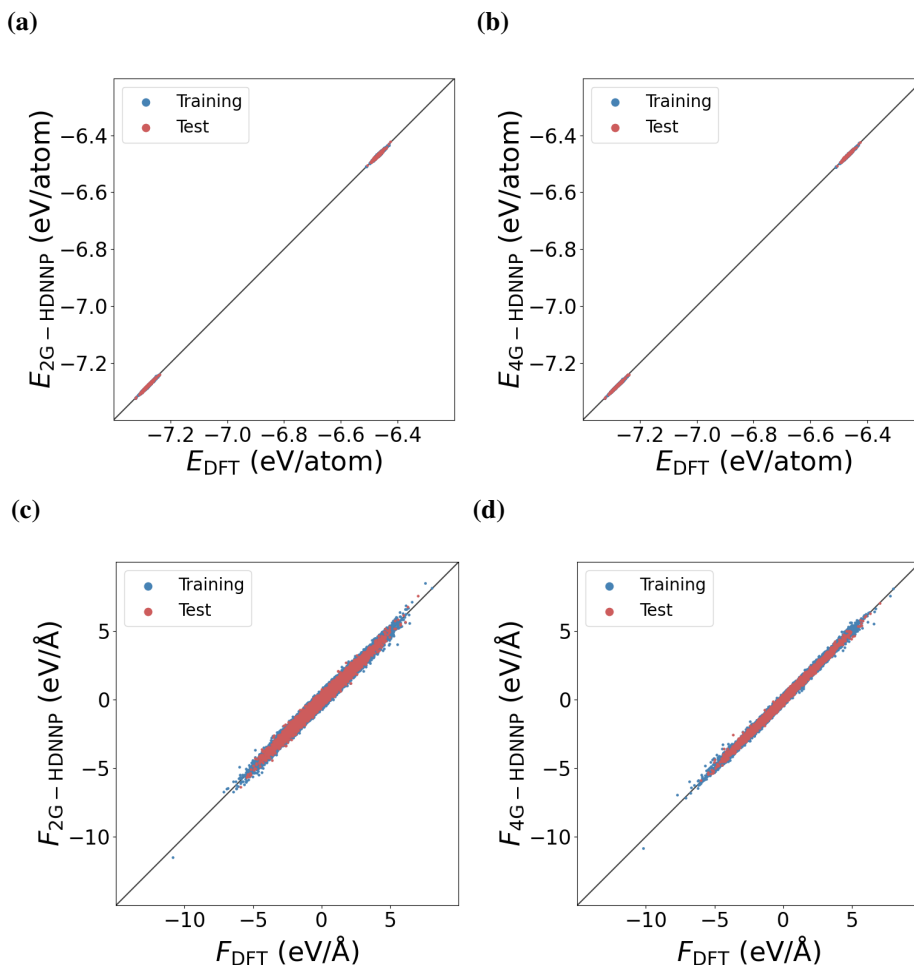


**Fig. 4.3:** Correlation plots of binding energies predicted by the 2G-HDNNP (a), 4G-HDNNP (b), and atomic force components predicted by the 2G-HDNNP (c), 4G-HDNNP (d) in the training and test sets for  $C_{10}H_2/C_{10}H_3^+$  systems. Reprinted (adapted) with permission from Ref. [34]. Copyright 2021 Springer Nature.

correlation plots of force component as illustrated in Fig. 4.3 (c) and (d).

Furthermore, the correlation of the unscaled 3G-HDNNP and 4G-HDNNP charges in the training and test sets compared to DFT charges is plotted in Fig. 4.4. It can be clearly seen that the 4G-HDNNP is considerably more accurate than the unscaled 3G-HDNNP in reproducing DFT charges.

To provide statistics for the overall performance of different potentials, the root mean square errors (RMSEs) of charges, binding energies and force components for different generations of HDNNPs compared to DFT in the training and test sets are given in Tab. 4.1. The 4G-HDNNP obtains below  $7.0 \times 10^{-3}$  e, 1.2 meV/atom and 0.08 eV/Å,

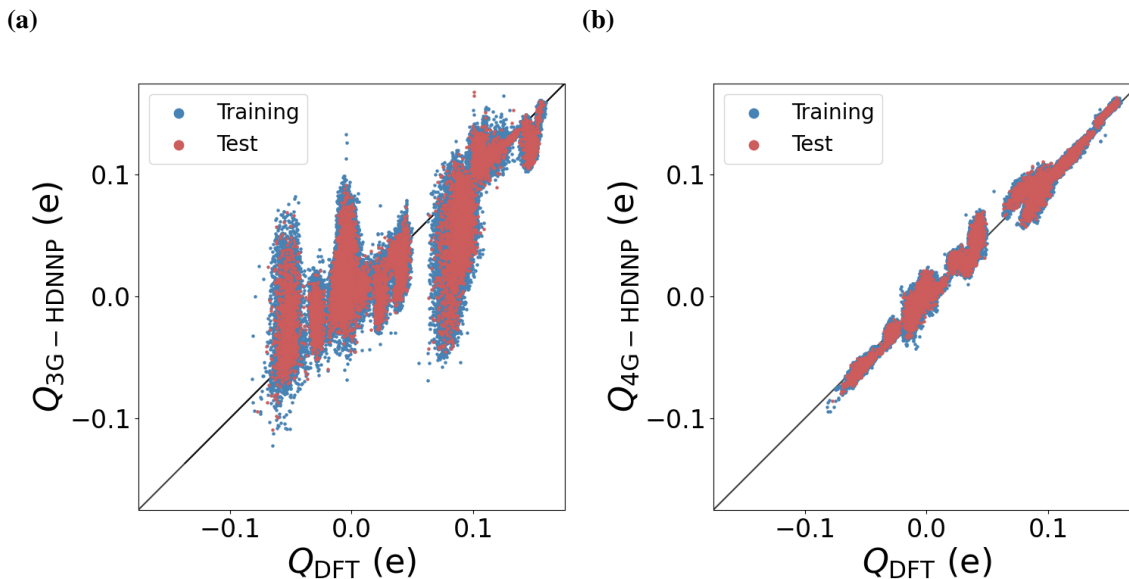


**Fig. 4.4:** Correlation plots of partial charges predicted by the unscaled 3G-HDNNP (a) and 4G-HDNNP (b) in the training and test sets for  $C_{10}H_2/C_{10}H_3^+$  systems. Reprinted (adapted) with permission from Ref. [34]. Copyright 2021 Springer Nature.

respectively. All these RMSE values show that the 4G-HDNNP reproduces DFT results with state-of-the-art accuracy for all reported properties while previous generations of HDNNPs are unable to reach such accuracy.

**Tab. 4.1:** Root mean square errors of charges ( $10^{-3}$  e), binding energies (meV/atom) and force components (meV/Å) for the  $C_{10}H_2/C_{10}H_3^+$  data set. The training and test sets contain 9035 and 984 structures, respectively. Numbers in brackets indicate the errors of the test set. Reprinted (adapted) with permission from Ref. [34]. Copyright 2021 Springer Nature.

methods	charges	binding energies	force components
2G-HDNNP	—	1.583 (1.619)	130.7 (129.5)
3G-HDNNP (unscaled)	27.36 (27.35)	3.192 (3.197)	652.5 (658.3)
3G-HDNNP (scaled)	19.98 (20.08)	2.017 (2.045)	229.9 (231.0)
4G-HDNNP	5.78 (6.58)	1.148 (1.194)	77.7 (78.0)

To investigate the low accuracy of 3G-HDNNPs on the partial charges in more detail, the partial charges of DFT-optimized  $C_{10}H_2$  and  $C_{10}H_3^+$  are computed with DFT, 3G- and 4G-HDNNPs. After protonation, the hybridization state of the terminal carbon atom is

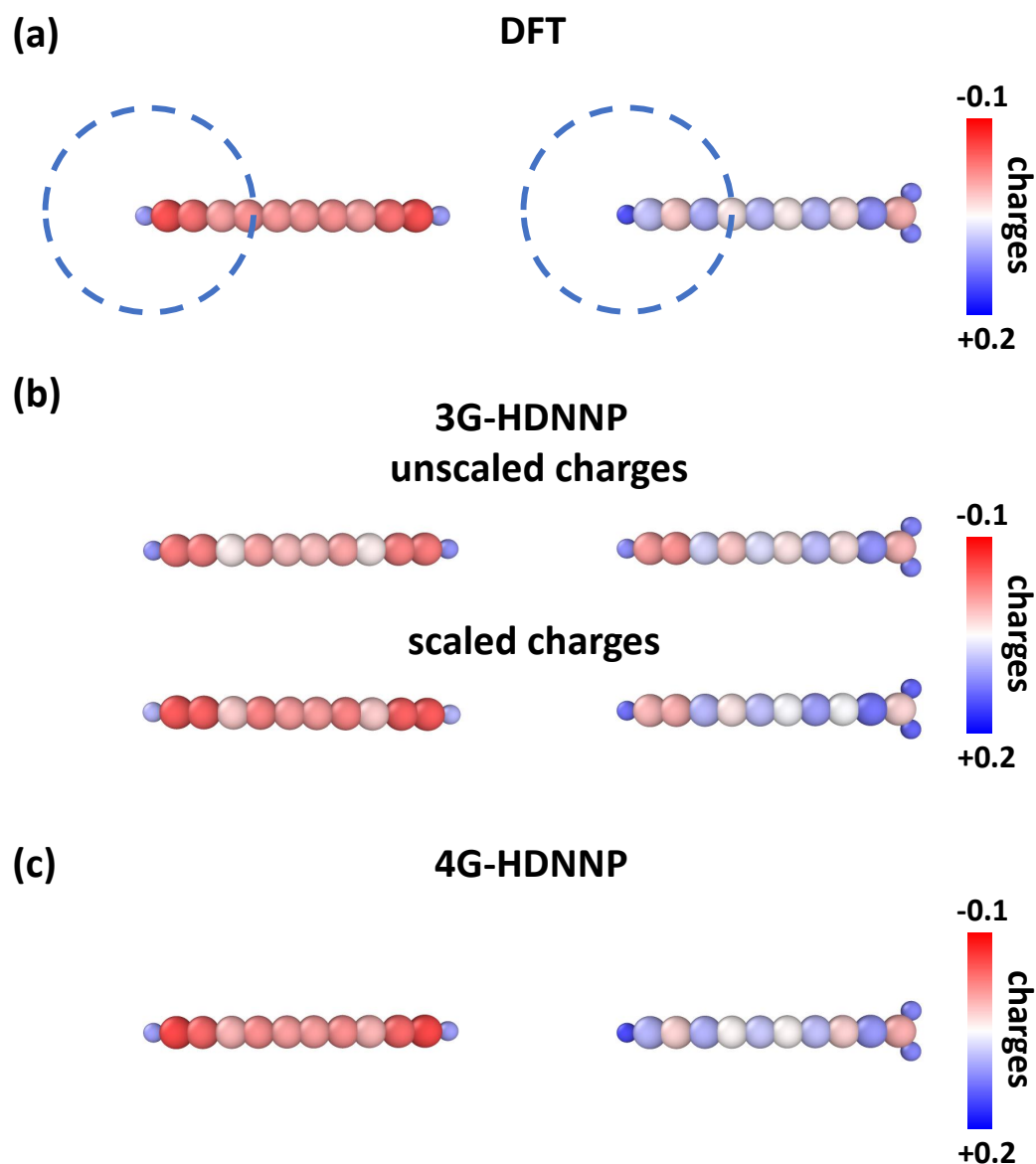


**Fig. 4.5:** Atomic Hirshfeld charges on the DFT-optimized  $C_{10}H_2$  and  $C_{10}H_3^+$  obtained with DFT (a), the unscaled and scaled 3G-HDNNPs (b), and 4G-HDNNP (c). The hydrogen and carbon atoms are labeled as small and large spheres, respectively. The atomic environment of the hydrogen atom is indicated as a dashed circle for illustration of the cutoff radius for constructing HDNNPs. Reprinted (adapted) with permission from Ref. [34]. Copyright 2021 Springer Nature.

changed to  $sp^2$ . Hence, the electronic structure of  $C_{10}H_3^+$  is modified accordingly over the whole molecule. This electronic change can be indicated by the DFT charges of both molecules, as displayed in Fig. 4.5 (a).

Atomic charges predicted by the 3G-HDNNPs are shown in Fig. 4.5 (b). The first case is the unscaled version and the second case is the scaled version, where the atomic charges are corrected using Eq. 2.35 to enforce charge conservation. It can be clearly seen that both unscaled and scaled 3G-HDNNPs provide qualitatively incorrect charge predictions for the left half of the molecule. This is expected since the distance of the added proton is far beyond the cutoff sphere of the left carbon atom in the left half of the molecule. In addition, the atomic environments after the DFT optimization for the left half of both molecules differ only slightly between the two different charge states. Hence, the resulting unscaled 3G-HDNNP charges are very similar as shown in Fig. 4.5 (c). The scaling does not significantly improve the accuracy of partial charges.

Further, most of the atomic environments for the left half of the molecules in the training set are basically identical. However, both molecules have completely different charge distributions, which yields a large fitting error due to the contradictory information. These atomic charges correspond to the region with large deviations in the correlation plot (see Fig. 4.4 (a)). To obtain a lower fitting error in the 3G-HDNNP, ANNs assign the average charges on the atoms for both molecules, which are qualitatively different with DFT charges. For instance, the partial charges on atom 2, i.e., the left carbon atom, predicted by the unscaled 3G-HDNNP are indistinguishable for both cases while the DFT charges are remarkably different. It is noted that the unscaled 3G-HDNNP would predict identical charges on atoms 1-6 in  $C_{10}H_2$  and  $C_{10}H_3^+$  if their chemical environments were exactly the same before and after the protonation. In addition, the scaled 3G-HDNNP would have similar but not the same charges due to the correction of scaling. On the other hand, the 4G-HDNNP reproduces DFT charges for both molecules with excellent agreement as shown in Fig. 4.5 (d). This is due to the Qeq scheme in 4G-HDNNP, which accurately distributes the partial charges over the whole molecule depending on flexible environment-dependent electronegativities and the given total charge of the system.

The inaccurate 3G-HDNNP charges lead to poor energy and force predictions for  $C_{10}H_2$  and  $C_{10}H_3^+$ . The errors of the total energies, mean errors of atomic charges and forces of different generation of HDNNPs for the DFT-optimized structures are given in Tab. 4.2. The unscaled 3G-HDNNP predicts large force errors of more than  $0.4 \text{ eV/\AA}$  with respect to DFT. The scaled 3G-HDNNP improves certain accuracy of forces although it is still far away from the state-of-the-art accuracy. Interestingly, the 2G-HDNNP is even generally better than both versions of 3G-HDNNP in terms of energies and forces since the accuracy of 3G-HDNNPs is deteriorated due to the non-physical charge predictions. This also explains the larger RMSE of binding energies and force components obtained by the 3G-HDNNPs compared to the 2G-HDNNP in the training and test sets (see Tab. 4.1). In contrast, the 4G-HDNNP achieves outstanding accuracy of energies, charges and forces for both DFT-optimized molecules as shown in Tab. 4.2 because of its ability to capture non-local effects. A comparable performance can be observed from the correlation plots and RMSE values of binding energies and forces in the training and test sets for the same reason.

**Tab. 4.2:** Binding energy error (meV/atom) and mean errors of the partial charges ( $10^{-3}$  e) and atomic forces (eV/Å) for the two DFT-optimized structures of  $C_{10}H_2$  and  $C_{10}H_3^+$ . Reprinted (adapted) with permission from Ref. [34]. Copyright 2021 Springer Nature.

	methods	binding energy	charges	forces
$C_{10}H_2$	2G-HDNNP	0.684	—	0.095
	3G-HDNNP (unscaled)	1.255	19.72	0.430
	3G-HDNNP (scaled)	2.193	10.76	0.138
	4G-HDNNP	0.463	4.82	0.032
$C_{10}H_3^+$	2G-HDNNP	0.922	—	0.127
	3G-HDNNP (unscaled)	0.046	17.82	0.658
	3G-HDNNP (scaled)	1.425	17.72	0.259
	4G-HDNNP	0.176	5.05	0.042

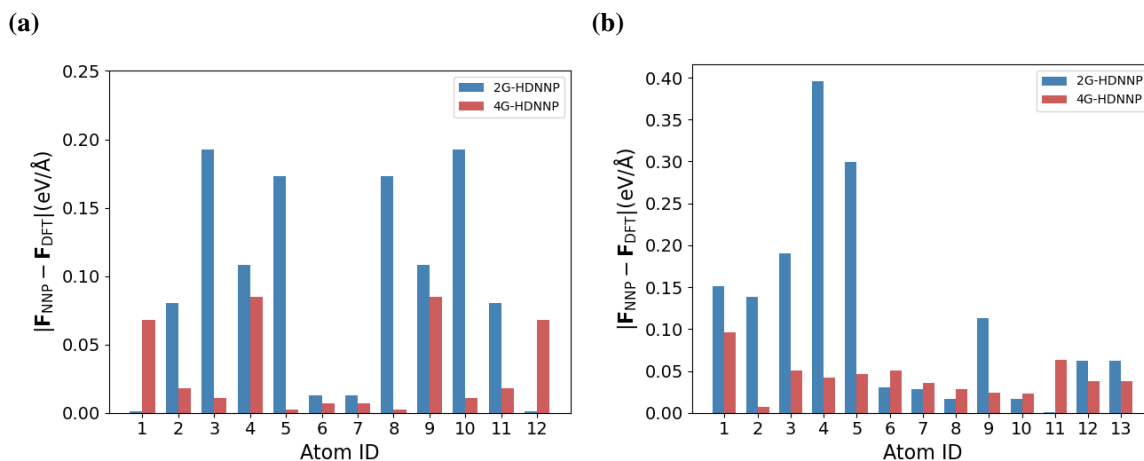


**Fig. 4.6:** Force errors of the 2G- and 4G-HDNNPs in the two DFT-optimized structures of  $C_{10}H_2$  (a) and  $C_{10}H_3^+$  (b). Reprinted (adapted) with permission from Ref. [34]. Copyright 2021 Springer Nature.

To find out the reason causing large force errors for the 2G-HDNNP, the absolute error of the force acting on each atom predicted by 2G- and 4G-HDNNPs for  $C_{10}H_2$  and  $C_{10}H_3^+$  is plotted in Fig 4.6. The 4G-HDNNP predicts the DFT forces with an average error of only 0.037 eV/Å for all atoms in both molecules. In contrast, the 2G-HDNNP yields large force errors for the atoms in the middle of  $C_{10}H_2$  and in the left half of  $C_{10}H_3^+$ . These phenomena are consistent with the charge errors of 3G-HDNNPs for both molecules. It shows that 2G- and 3G-HDNNPs, which rely only on the locality approximation, are unable to distinguish both molecules.

Notably, the low energy errors of 2G-HDNNP are inconsistent with the relatively high force errors. This is attributed to the error compensation in the distribution of atomic energies. The atoms on the right side of the molecule are able to detect the changes of the electronic structure, caused by protonation based on the corresponding modification of the atomic environment. Consequently, the atomic energy contributions in the right half of molecule are adjusted to reduce the error of the total energy caused by the problematic atomic energies in the left half of the molecule, which are independent of protonation due to the limited cutoff sphere. Such distribution of atomic energies based on the wrong reason leads to large force errors.

## 4.2.2 Metal Clusters

The equilibrium structure of metal clusters depends on the total charge of the system [171–173], which can significantly change the shape of the PES. Here, the small metal cluster  $\text{Ag}_3$  is evaluated in two different charge states. The 2G-HDNNP should, in principle, accurately reproduce the PES of this trimer with respect to DFT due to the small system size, which does not have any long-range effect since the whole system is fully covered by each atomic environment, but 2G-HDNNPs are restricted to a single charge state.

To illustrate the limitations, 2G-, 3G- and 4G-HDNNPs with a cutoff radius  $R_c = 5.29$  Å are trained to a data set containing both configurations of  $\text{Ag}_3^-$  and  $\text{Ag}_3^+$ , which are generated from MD simulations and geometry optimizations. The correlation of binding energies and force components for 2G- and 4G-HDNNPs compared to DFT is plotted in Fig. 4.7. As expected, the 2G-HDNNP fail even at the qualitative level as shown in Fig. 4.8 (a) and (c). This is attributed to the fact that the 2G-HDNNP does not contain explicit information about the global charge distribution according to the total charge of the systems. The configurations of  $\text{Ag}_3^-$  and  $\text{Ag}_3^+$  in the data set are very similar while the corresponding PES is completely different. Hence, this introduces contradictory information in the data set for the construction of the 2G-HDNNP, resulting in large fitting errors. In contrast, the 4G-HDNNP, which takes the global charge distribution of the system into account, agrees very well with the DFT binding energies and forces. Similarly, the unscaled 3G-HDNNP is inaccurate in reproducing DFT charges with large errors as can be clearly seen in Fig. 4.8 (a). This can be explained by the same reasons as the poor energy and force predictions of the 2G-HDNNP. However, the 4G-HDNNP predicts atomic charges in good agreement with the DFT charges, as can be seen in Fig. 4.8 (b). This illustrates that the 4G-HDNNP can handle a wide range of charge values using the Qeq scheme with flexible electronegativities expressed by ANNs.

In addition to the correlation plots, the RMSE values of 2G-, 3G- and 4G-HDNNPs are presented in Tab. 4.3. The errors of binding energies and force components obtained with the 4G-HDNNP are only approximately 1.3 meV and 30 meV/Å, which are significantly lower than the 2G-HDNNP. Besides, the charge errors predicted by the 4G-HDNNP are

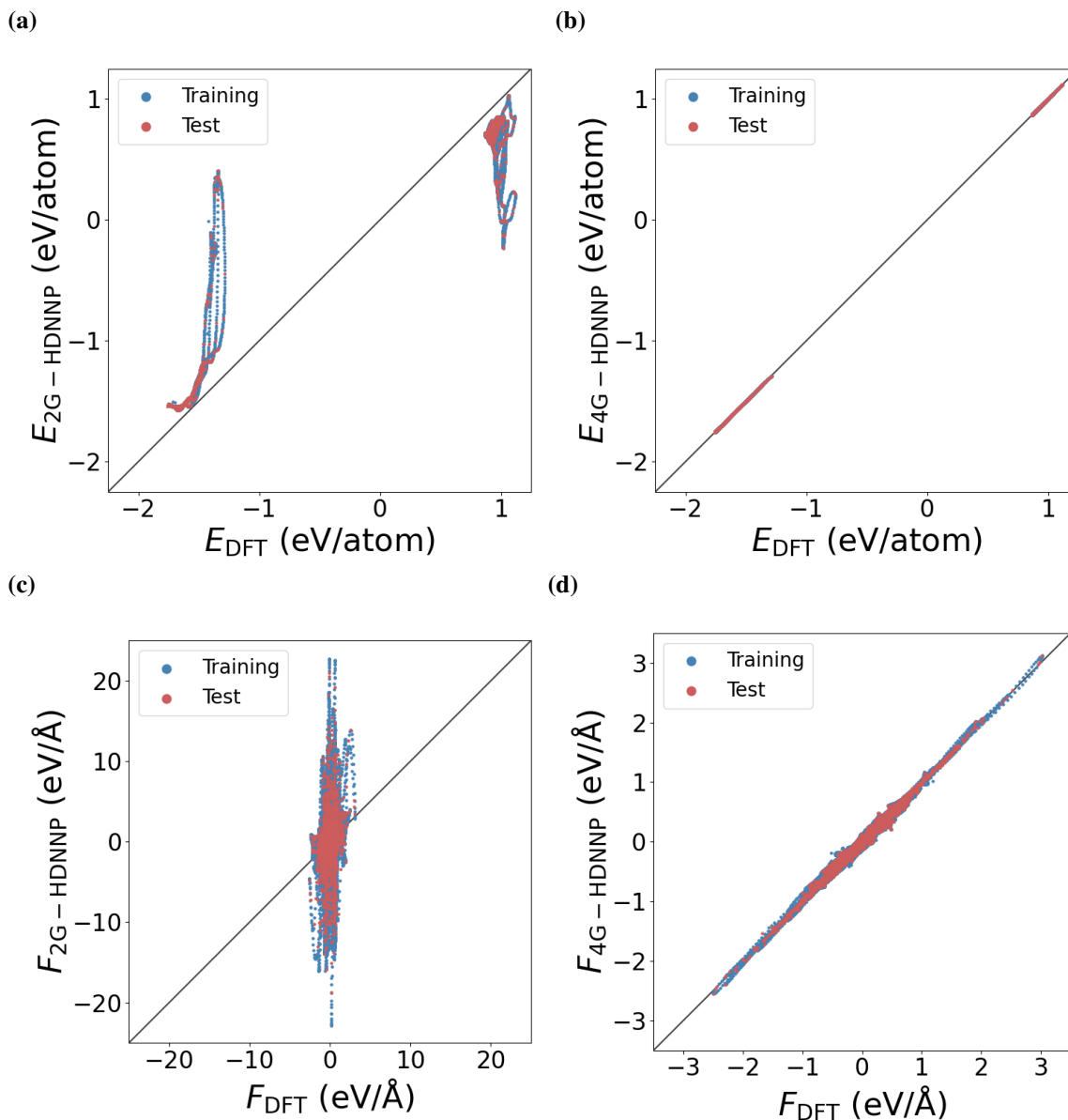


**Fig. 4.7:** Correlation plots of binding energies predicted by the 2G-HDNNP (a), 4G-HDNNP (b), and atomic force components predicted by the 2G-HDNNP (c), 4G-HDNNP (d) in the training and test sets for  $Ag_3^+/Ag_3^-$  systems. Reprinted (adapted) with permission from Ref. [34]. Copyright 2021 Springer Nature.

around 0.01 e while the errors of both unscaled and scaled 3G-HDNNPs are far from the accuracy of state-of-the-art MLPs. Apart from that, these 3G-HDNNPs also yield large fitting errors in terms of binding energies and forces although the scaling improves the accuracy of charges. These observations can be accounted for the non-physical electrostatic energies and forces calculated from the qualitatively incorrectly predicted charges, which

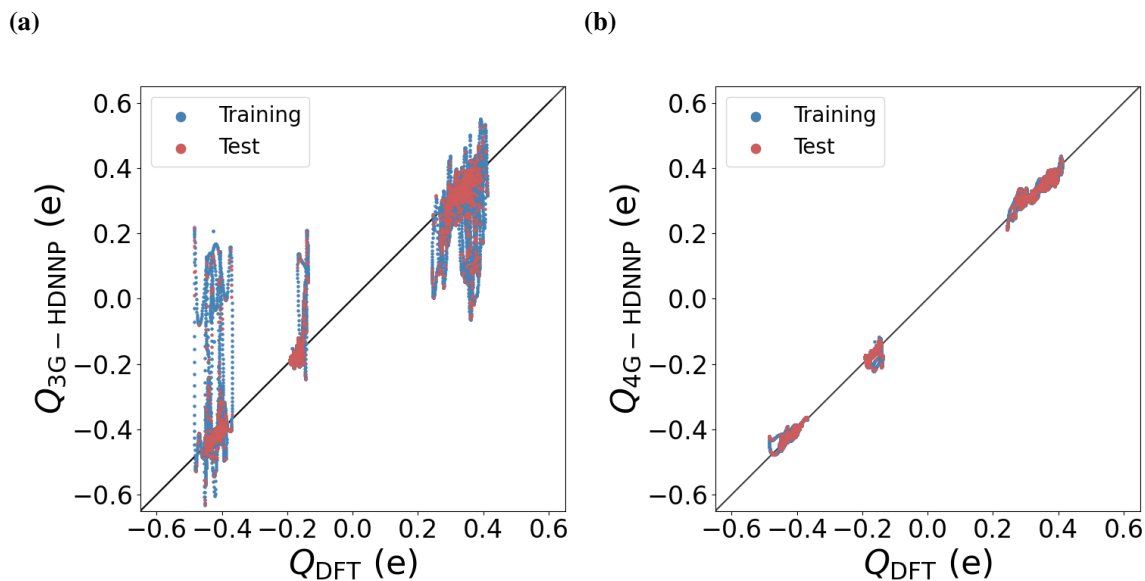


**Fig. 4.8:** Correlation plots of partial charges predicted by the unscaled 3G-HDNNP (a) and 4G-HDNNP (b) in the training and test sets for  $\text{Ag}_3^+/\text{Ag}_3^-$  systems. Reprinted (adapted) with permission from Ref. [34]. Copyright 2021 Springer Nature.

**Tab. 4.3:** Root mean square errors of charges ( $10^{-3}$  e), binding energies (meV/atom) and force components (meV/Å) for the  $\text{Ag}_3^-/\text{Ag}_3^+$  data set. The training and test sets contain 9930 and 1083 structures, respectively. Numbers in brackets indicate the errors of the test set. Reprinted (adapted) with permission from Ref. [34]. Copyright 2021 Springer Nature.

methods	charges	binding energies	force components
2G-HDNNP	—	355.0 (352.0)	1812 (1803)
3G-HDNNP (unscaled)	75.50 (77.55)	345.0 (340.0)	1909 (1963)
3G-HDNNP (scaled)	26.24 (26.48)	321.1 (320.2)	1912 (1913)
4G-HDNNP	10.61 (9.98)	1.3 (1.3)	32 (32)

deteriorate the fitting of the short-range part.

To further demonstrate the limitations of 2G-HDNNPs, the initial DFT-optimized geometry of the neutral Ag trimer is relaxed in two different charge states using 2G- and 4G-HDNNPs. The root mean square deviation (RMSD) with respect to the DFT-optimized geometry of the respective charge state is compared. As expected, the minima predicted by 2G-HDNNP are identical for both charge states because both cases are indistinguish-

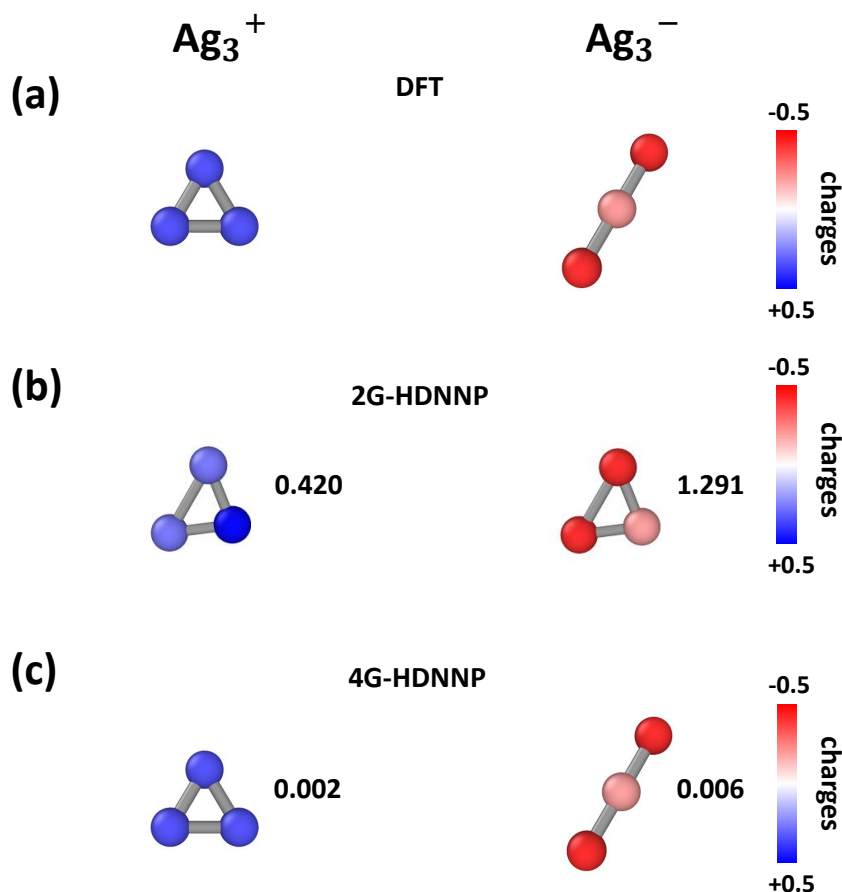


**Fig. 4.9:** Optimized structures of  $\text{Ag}_3^+/\text{Ag}_3^-$  and corresponding atomic charges predicted by DFT (a), the 2G-HDNNP (b) and 4G-HDNNP (c). The root mean square deviation for minima predicted by 2G- and 4G-HDNNPs in Å with respect to the respective DFT minima are given in numbers. The scaled 3G-HDNNP charges are displayed in (b) for illustrative purposes only. The tool for calculating the root mean square deviation of structures was provided by Jonas Finkler [174]. Reprinted (adapted) with permission from Ref. [34]. Copyright 2021 Springer Nature.

able. This is due to the loss of a unique mapping from atomic positions to short-range energy contributions for a data set containing different total charges. As a consequence, the resulting geometries do not match any minima predicted by DFT with a large RMSD as displayed in Fig. 4.9. However, the 4G-HDNNP is able to reproduce DFT minima with a very small RMSD, which is below 0.01 Å for both charge states. Moreover, the corresponding energy errors calculated from the 4G-HDNNP are only about 1.166 meV/atom and 0.320 meV/atom for  $\text{Ag}_3^-$  and  $\text{Ag}_3^+$ , respectively. The errors of the 2G-HDNNP are 0.605 and 2.017 eV/atom and significantly larger than the 4G-HDNNP, which is consi-

tent with the large structural deviation of the minima with respect to DFT. Moreover, the energy errors obtained from the scaled 3G-HDNNP are 0.713 and 5.721 eV/atom, which is even worse than the 2G-HDNNP because of the non-physical electrostatic contributions calculated using inaccurate scaled charges.

### 4.2.3 Ionic Fragments

The first two examples show the inability of 2G- and 3G-HDNNPs to describe systems with multiple charge states. Ionic systems, on the other hand, can exhibit long-range charge transfer without changing the total charge of the system. In this example, the changes of the PES for a positively charged  $\text{Na}_9\text{Cl}_8^+$  cluster after the removal of a neutral sodium atom is studied. The DFT-optimized structure of  $\text{Na}_9\text{Cl}_8^+$  is shown in Fig. 4.10. To redistribute the atomic charges over the whole system, the neutral brown sodium atom is removed, while other atomic positions remain fixed.

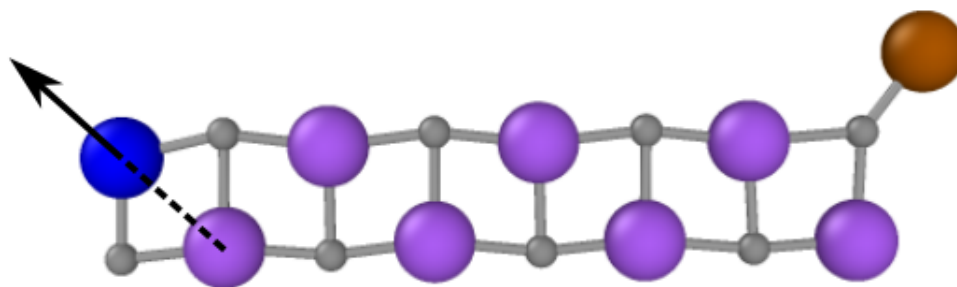


**Fig. 4.10:** DFT-optimized structure of the  $\text{Na}_9\text{Cl}_8^+$  cluster. The sodium atoms are colored in purple, blue and brown color while the chlorine atoms are shown in grey. The arrow indicates the moving direction of the blue sodium atom. The structure of  $\text{Na}_8\text{Cl}_8^+$  is constructed by removing the brown sodium atom. This example is proposed by Jonas Finkler. Reprinted (adapted) with permission from Ref. [34]. Copyright 2021 Springer Nature.

To investigate non-local effects caused by removing the sodium atom on the PES, 2G-, 3G- and 4G-HDNNPs with  $R_c = 5.29 \text{ \AA}$  are constructed based on the data set containing both configurations.

The correlation plot of binding energies, atomic forces and charges for different generations of HDNNPs and DFT are displayed in Fig. 4.11 and Fig. 4.12. The fitting errors of 2G- and 3G-HDNNPs are relatively low compared to the first two examples in terms of all quantities due to two reasons. First, the configurations in the data set have the same total charge, and therefore contain less contradictory information for the construction of 2G- and 3G-HDNNPs. Second, the errors of binding energies caused by the global redistribution of the charges after removing the brown sodium atom are reduced by the neighboring

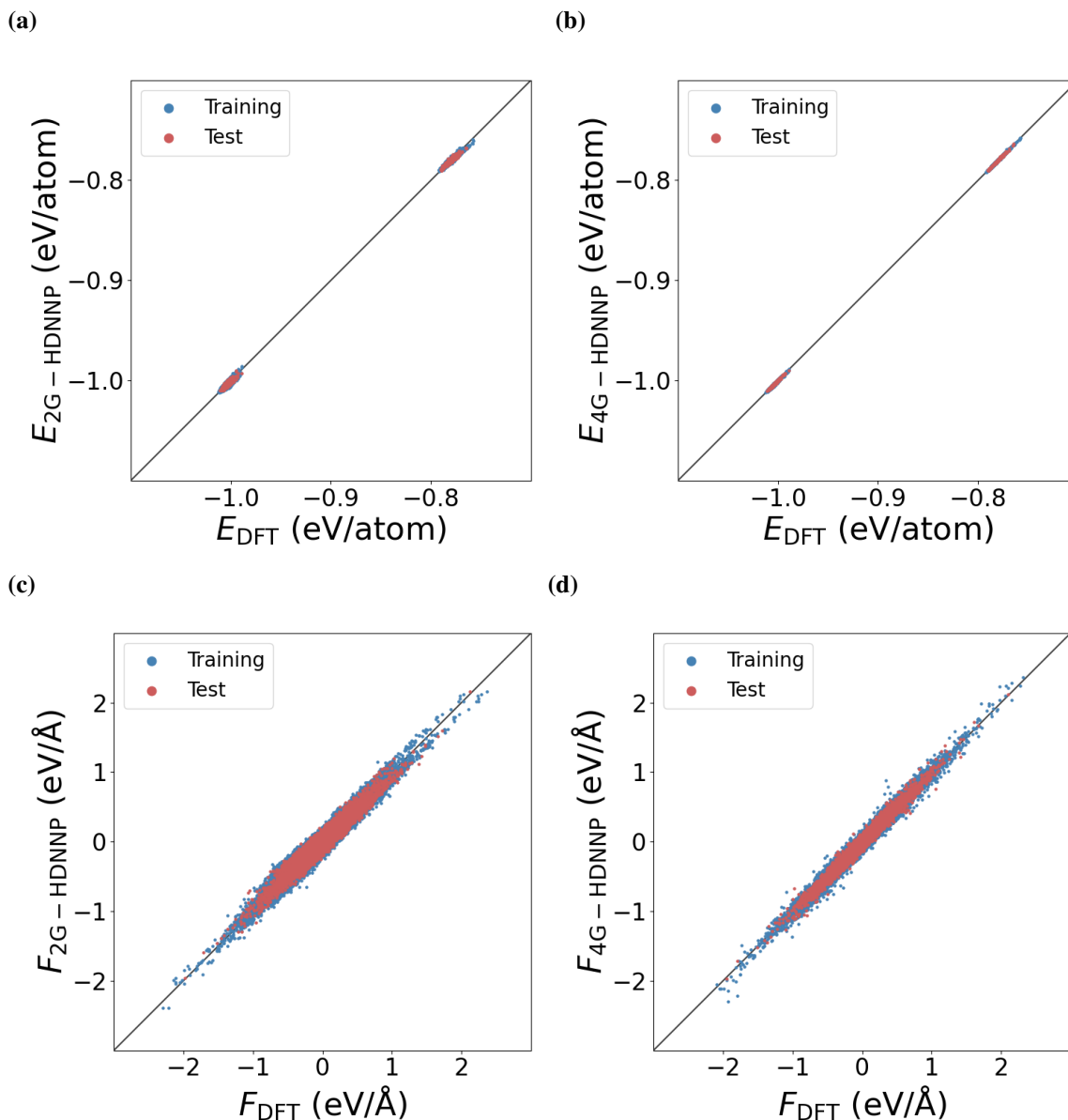


**Fig. 4.11:** Correlation plots of binding energies predicted by the 2G-HDNNP (a), 4G-HDNNP (b), and atomic force components predicted by 2G-HDNNP (c), 4G-HDNNP (d) in the training and test sets for  $\text{Na}_8\text{Cl}_8^+/\text{Na}_9\text{Cl}_8^+$  systems. Reprinted (adapted) with permission from Ref. [34]. Copyright 2021 Springer Nature.

atoms of the brown sodium atom. They are able to distinguish between the two cases and their atomic energies are adjusted to yield an acceptable agreement with reference calculations. Still, 4G-HDNNP significantly improves the accuracy in terms of all quantities compared with previous generations of HDNNPs. Notably, the 4G-HDNNP charge errors in the range of DFT charges from  $-0.28$  to  $-0.5$  e are relatively large. This is attributed

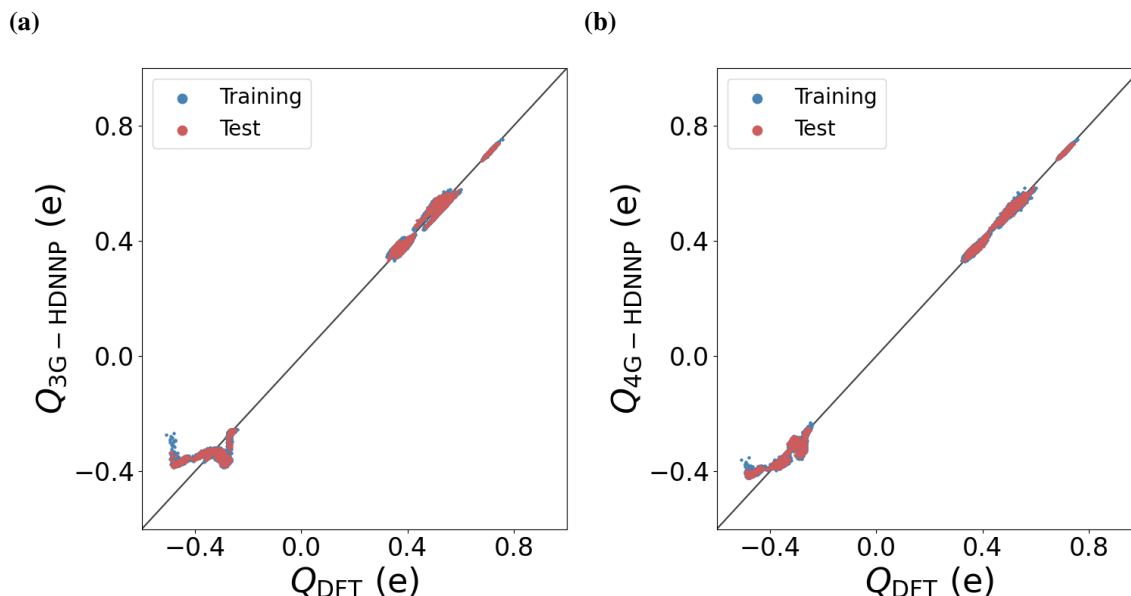


**Fig. 4.12:** Correlation plots of partial charges predicted by the unscaled 3G-HDNNP (a) and 4G-HDNNP (b) in the training and test sets for  $\text{Na}_8\text{Cl}_8^+/\text{Na}_9\text{Cl}_8^+$  systems. Reprinted (adapted) with permission from Ref. [34]. Copyright 2021 Springer Nature.

to the chlorine atom located below the blue sodium atom. The DFT charge on that chlorine atom changes significantly ( $\approx 0.2$  e) depending on the removal of the brown sodium atom. Due to the very similar atomic environments of the chlorine atom for both clusters in the data set, the resulting electronegativity is not flexible enough to reproduce the large charge difference according to the Qeq scheme.

**Tab. 4.4:** Root mean square errors of charges ( $10^{-3}$  e), binding energies (meV/atom) and force components (meV/Å) for the  $\text{Na}_8\text{Cl}_8^+/\text{Na}_9\text{Cl}_8^+$  data set. The training and test sets contain 4493 and 507 structures, respectively. Numbers in brackets indicate the errors of the test set. Reprinted (adapted) with permission from Ref. [34]. Copyright 2021 Springer Nature.

methods	charges	binding energies	force components
2G-HDNNP	—	1.690 (1.692)	57.54 (57.39)
3G-HDNNP (unscaled)	28.28 (28.52)	1.426 (1.470)	57.69 (59.49)
3G-HDNNP (scaled)	20.75 (20.80)	2.058 (2.042)	73.47 (76.67)
4G-HDNNP	15.87 (15.83)	0.474 (0.481)	32.45 (32.78)

The RMSE values calculated from different generations of HDNNPs in the training

and test sets are reported in Tab. 4.4. Interestingly, the scaled 3G-HDNNP performs even worse than its unscaled counterpart in terms of binding energies and force components. This is because the scaling deteriorates the accuracy of the overall charge distribution and thus degrades the fitting quality of the short-range part. At first glance, the reported error of the scaled 3G-HDNNP charges is lower, since the scaling improves the charge errors at the range of  $-0.4 e$  (see Fig. 4.12). This effectively reduces the RMSE values due to the larger contributions from the outliers. However, the scaling also reduces the accuracy of other atomic charges, which are already in agreement with DFT. The PES relies on the accuracy of all charges in the system, and its accuracy is thus deteriorated by this procedure. On the other hand, the 4G-HDNNP achieves the RMSE of 0.016 e, 0.5 meV/atom and 0.035 eV/Å in terms of charges, binding energies and force components, which show noticeable improvements compare to previous generations of HDNNPs.

The inability to capture non-local charge transfer by 2G- and 3G-HDNNPs is illustrated in the relative energies of the systems and the atomic forces acting on the blue sodium atom when moving the atom along the one-dimensional path indicated by the arrow in Fig. 4.10. Fig. 4.13 shows the energies obtained with 2G-, 3G- and 4G-HDNNPs and DFT for both systems. All energies are relative to the minimum of the DFT total energy of the corresponding clusters. The difference in the equilibrium Na-Na distance for  $\text{Na}_8\text{Cl}_8^+$  and  $\text{Na}_9\text{Cl}_8^+$  predicted by DFT is larger than 0.1 Å, arising from the removal of the distant brown sodium atom.

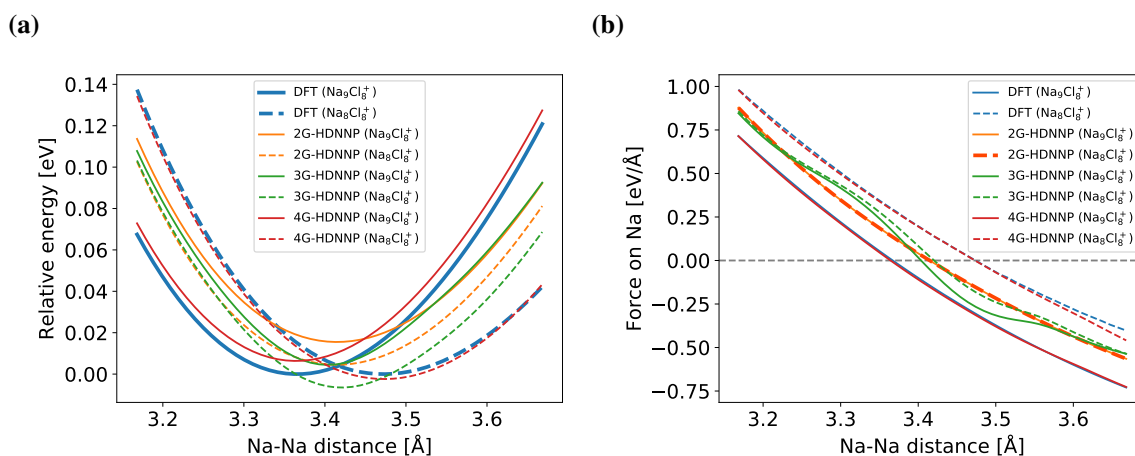


**Fig. 4.13:** Relative energies corresponding to the moving path of the blue sodium atom in Fig. 4.10 obtained with different generations of HDNNPs and DFT (a). The energies are shifted to the lowest DFT energy of the respective clusters. The corresponding atomic forces acting on the blue sodium atom during the scan are shown in (b). The plotted 3G-HDNNP curves are based on the unscaled charges. Reprinted (adapted) with permission from Ref. [34]. Copyright 2021 Springer Nature.

The 2G-HDNNP is unable to capture the long-range charge transfer caused by the brown sodium atom, which is far beyond the local chemical environment of the blue sodium atom. The atomic energies of the sodium atom and its neighboring atoms are exactly the same for both cases, which leads to the same equilibrium position with roughly the mean value of the two minima predicted by DFT. The energy offset for the 2G-HDNNP energy curves of both clusters exists due to some constant atomic energies on the right side of the clusters, since their atomic environments are unchanged when moving the blue sodium atom.

The unscaled 3G-HDNNP predicts very similar minima but not identical to 2G-HDNNP due to the additional long-range electrostatic interactions. The energy offset is not a constant anymore, which is attributed to the same reason. Even though the energy curves predicted by 2G- and 3G-HDNNPs only deviate about 1 meV/atom with respect to DFT results, the physical properties extracted from the potentials, i.e., the equilibrium bond lengths, are still qualitatively wrong. On the other hand, the energy curves predicted by 4G-HDNNP match DFT results with excellent accuracy including the equilibrium Na-Na bond distance for both clusters. Such example reveals that the 4G-HDNNP is able to describe non-local effects caused by long-range charge transfer, which is not covered by most of established MLPs.

The corresponding atomic forces acting on the blue sodium atom for  $\text{Na}_8\text{Cl}_8^+$  and  $\text{Na}_9\text{Cl}_8^+$  are displayed in Fig. 4.13 (b). All results are consistent with the behavior of the energy curves. The DFT forces acting on the moving sodium atom are different for both clusters and the equilibrium positions indicated by the zero atomic force match with the position of the energy minimum shown in Fig. 4.13 (a). The 4G-HDNNP almost exactly reproduces the DFT forces for  $\text{Na}_8\text{Cl}_8^+$  and  $\text{Na}_9\text{Cl}_8^+$  while 2G-HDNNP predicts the same forces for both cases, which correspond to the constant energy offset between both energy curves. The forces obtained with the unscaled 3G-HDNNP are just slightly different due to the additional electrostatic contributions computed from the unscaled 3G-HDNNP charges.

#### 4.2.4 Gold Dimer on an Oxide Surface

The final benchmark system is chosen to be a Au dimer adsorbed on a periodic MgO(001) slab. This type of systems has attracted a great deal of attention due to its interesting catalytic properties for water-gas shift reactions [175, 176], hydrogenation of unsaturated hydrocarbons [177], and the oxidation of carbon monoxide [178]. The orientation of clusters supported on such oxides can be modified through substitutional doping on the oxide surface. The catalytic activity of the system can be enhanced by controlling the cluster morphology using such techniques. 2G-HDNNPs have been constructed to study the properties of copper clusters adsorbed on a ideal zinc oxide slab [119, 179]. However, all these reported potentials are not applicable doped substrates, which involve long-range

charge transfer between the adsorbate and the dopant. Such non-local effects can be only captured by fourth-generation MLPs.

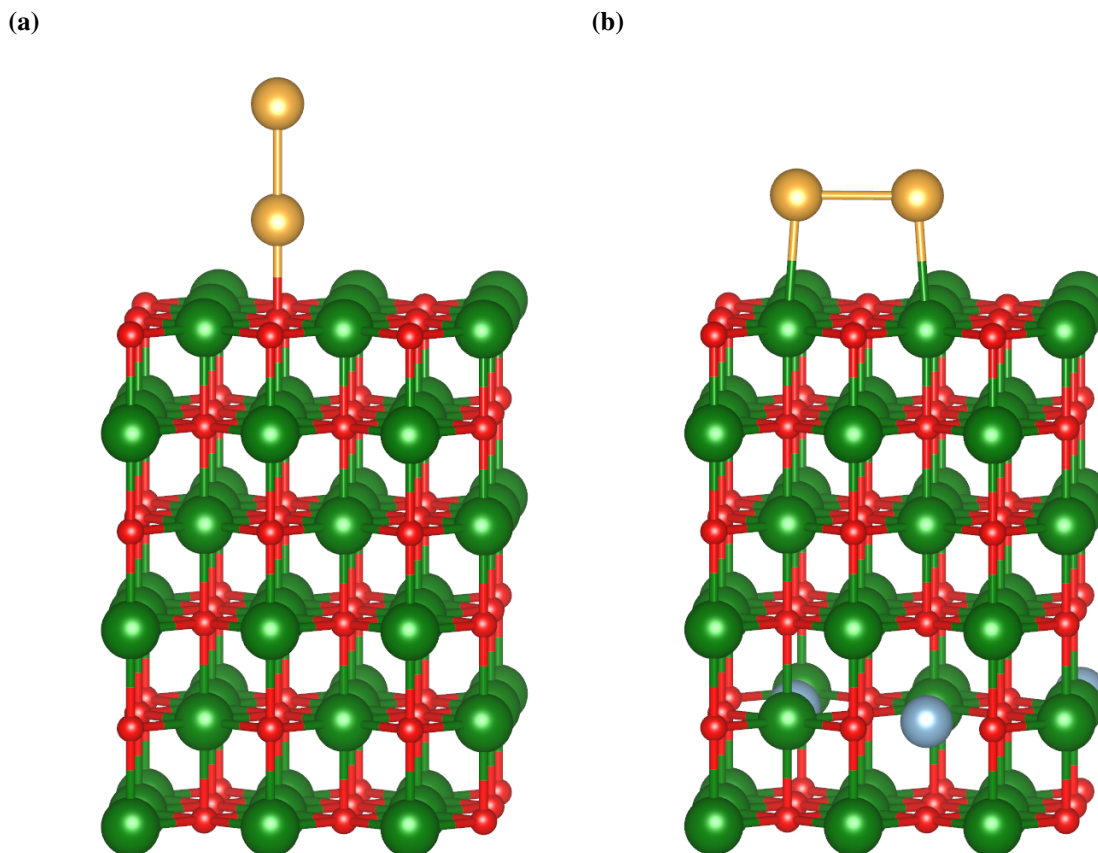


**Fig. 4.14:** DFT-optimized geometry of an Au dimer on the undoped and Al-doped MgO substrate. Panel (a) shows the non-wetting orientation of a Au dimer adsorbed on the O atom for the undoped case. The wetting orientation of the Au dimer adsorbed on Mg atoms for the Al-doped substrate is displayed in panel (b). The MgO(001) surface is constructed by replicating ( $3 \times 3$ ) super cell. The O, Mg, Al and Au atoms are colored in red, green, light grey and yellow, respectively. The structures are visualized using VESTA [180]. This example was proposed by Jonas Finkler. Reprinted (adapted) with permission from Ref. [34]. Copyright 2021 Springer Nature.

In the case of  $\text{Au}_2$  at MgO(001), two energetically favorable adsorption geometries of the gold dimer predicted by DFT are studied. The geometries are either the upright "non-wetting" orientation, where the dimer adsorbs on an oxygen atom at the top surface, or the "wetting" orientation, where two gold atoms attach on top of two Mg atoms. The relative stability of both orientations changes depending on whether the undoped or doped unrelaxed surfaces are considered. Fig. 4.14 (a) shows the DFT-optimized geometry of a gold dimer on the pure MgO support, which is the "non-wetting" orientation. The ground

state structure of a gold dimer changes to a "wetting" orientation when the MgO is doped by three aluminum atoms, as can be seen in Fig. 4.14 (b). The doped Al atoms are introduced into the fifth layer, which is far away from the gold atoms ( $> 10 \text{ \AA}$ ). In spite of the large separation, the gold atoms still experience the non-local effects arising from long-range charge transfer. The partial charges on the gold dimer are significantly reduced by around 0.2 e compared to the same orientation of the gold dimer on the undoped surface.

To examine the performance of the potentials for describing non-local effects, 2G-, 3G- and 4G-HDNNPs are constructed on a data set containing all four configurations.

Fig. 4.15 and Fig. 4.16 show the correlation plots of target properties obtained by different generations of HDNNPs with respect to DFT. The 4G-HDNNP predicts the correlation of binding energies and force components in much better agreement with DFT than the 2G-HDNNP. Besides, the 2G-HDNNP predicts very similar binding energies for some structures, while the DFT binding energies are very different as can be seen in Fig. 4.15 (a). These inconsistencies illustrate that the 2G-HDNNP is unable to distinguish between all four geometries. For the comparison of charges, the accuracy of the unscaled 3G-HDNNP is not satisfactory and the region of large errors shown in Fig. 4.16 (a) corresponds to the partial charges on the gold atoms. This illustrates that the unscaled 3G-HDNNP fails to distinguish the doped and undoped substrate that are far beyond the local environment of the gold atoms. The 4G-HDNNP in general reproduces all quantities with close-to-DFT quality since the Qeq scheme in 4G-HDNNP accurately describes the global charge distribution of the system and the corresponding PES.

**Tab. 4.5:** Root mean square errors of charges ( $10^{-3} e$ ), binding energies (meV/atom) and force components (meV/Å) for the  $\text{Au}_2\text{-MgO/Al-doped Au}_2\text{-MgO}$  data set. The training and test sets contain 4468 and 532 structures, respectively. Numbers in brackets indicate the errors of the test set. Reprinted (adapted) with permission from Ref. [34]. Copyright 2021 Springer Nature.

methods	charges	binding energies	force components
2G-HDNNP	—	2.299 (2.287)	155.4 (153.1)
3G-HDNNP (unscaled)	10.48 (10.84)	—	—
4G-HDNNP	5.66 (5.70)	0.209 (0.219)	81.1 (66.0)

The corresponding RMSE values for different generations of HDNNPs are provided in Tab. 4.5. The 4G-HDNNP predicts charges, binding energies and forces in excellent agreement with DFT, with RMSEs below  $6.0 \times 10^{-3} e$ , 0.5 meV/atom and 0.1 eV/Å. Previous generations of HDNNPs fall significantly behind these values.

The electronic change induced by doping with Al atoms switch the energetic order of

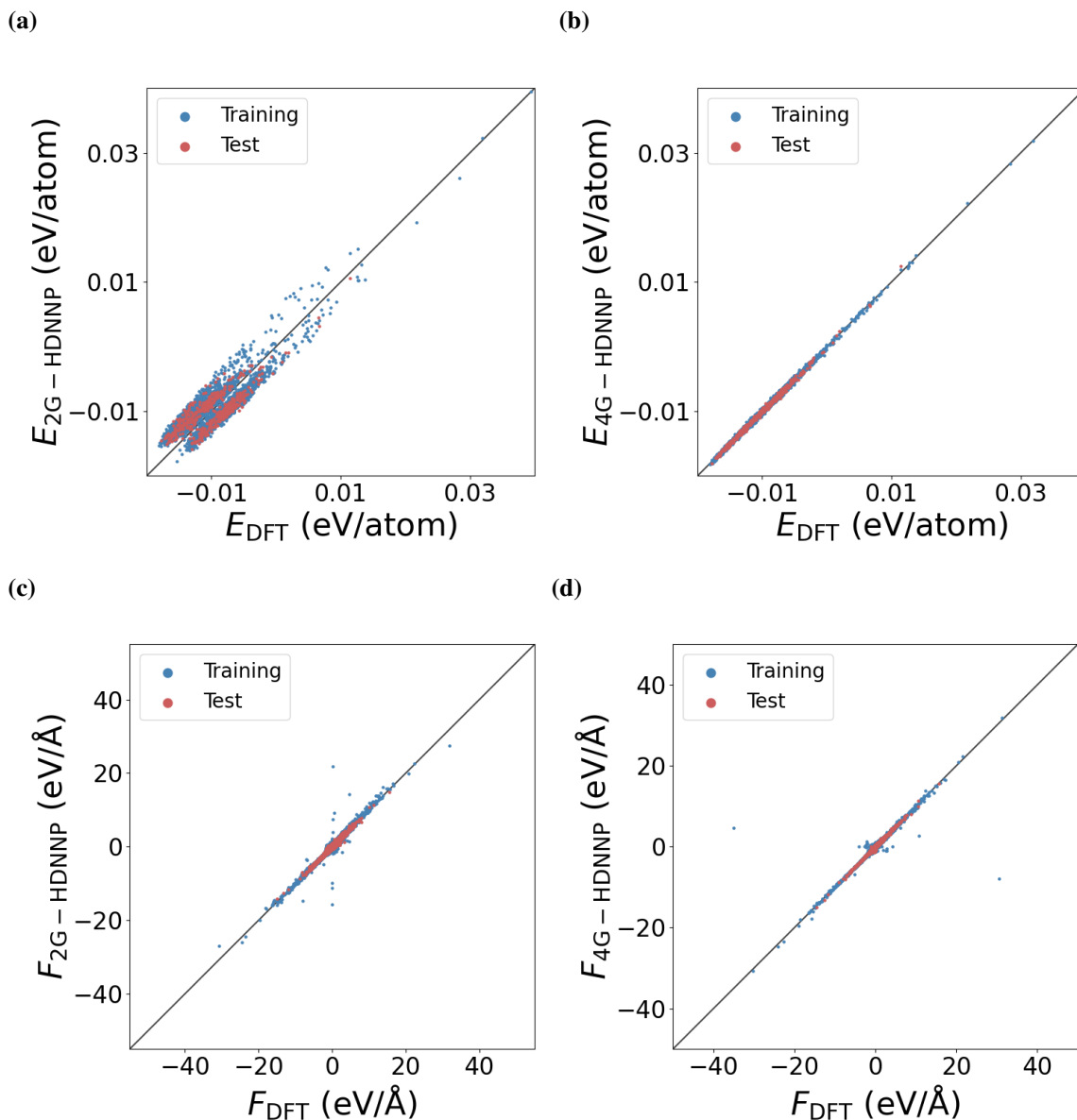


**Fig. 4.15:** Correlation plots of binding energies predicted by the 2G-HDNNP (a), 4G-HDNNP (b), and atomic force components predicted by the 2G-HDNNP (c), 4G-HDNNP (d) in the training and test sets for  $\text{Au}_2\text{-MgO/Al-doped Au}_2\text{-MgO}$  systems. Reprinted (adapted) with permission from Ref. [34]. Copyright 2021 Springer Nature.

the respective geometries. The energy difference ( $E_{\text{wetting}} - E_{\text{non-wetting}}$ ) between the wetting and non-wetting geometries on an undoped substrate and a doped substrate obtained with DFT is 929 meV and  $-2.7$  meV, respectively. However, the 2G-HDNNP predicts the same energy difference 375 meV for both substrates since the dopant atoms are far

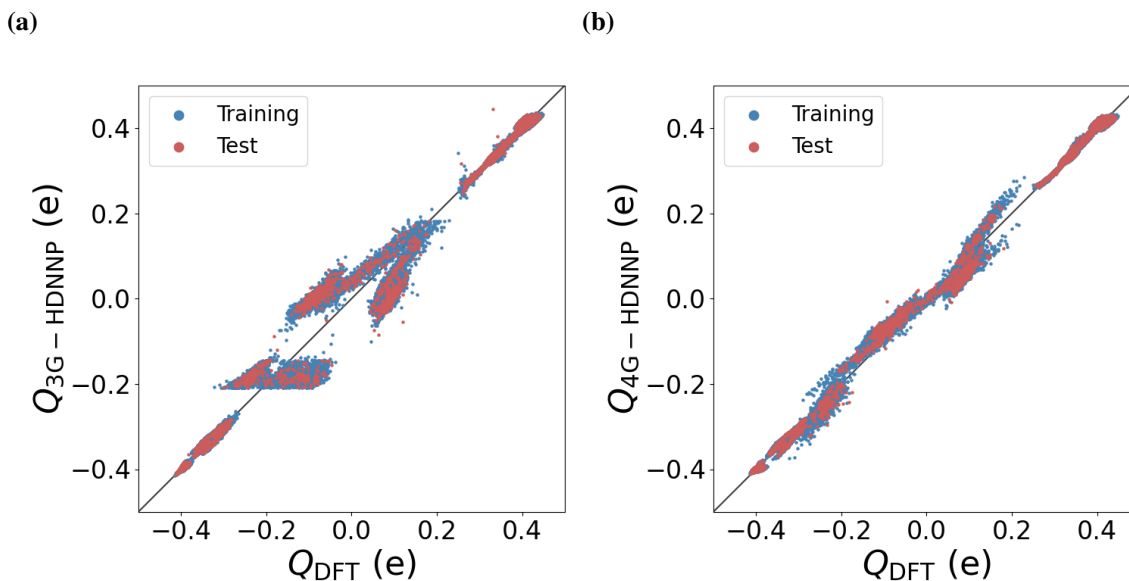


**Fig. 4.16:** Correlation plots of partial charges predicted by the unscaled 3G-HDNNP (a) and 4G-HDNNP (b) in the training and test sets for Au-MgO/Al-doped Au<sub>2</sub>-MgO systems. Reprinted (adapted) with permission from Ref. [34]. Copyright 2021 Springer Nature.

away from the local chemical environments of the the gold atoms. As a result, the 2G-HDNNP fails to capture the long-range charge transfer caused by the aluminium atoms. The energy difference calculated from 4G-HDNNP on an undoped slab and a doped slab is 975 meV and  $-41$  meV, which match DFT results with only a small deviation. Both the 4G-HDNNP and DFT results agree that the wetting orientation for the doped substrate is slightly energetically favorable and the non-wetting orientation for the undoped substrate is much more stable.

Apart from the energetic order, the electronic change caused by the doping also change the equilibrium bond distance of gold atoms to the adsorption site is also changed. A particular analysis of 2G- and 4G-HDNNPs has been done for the non-wetting orientation of the gold dimer attached on the undoped and doped surfaces. The relative energies of the respective systems with respect to the minimum of DFT energy, and the sum of atomic forces acting on the gold dimer, are plotted as a function of the bond distance between the oxygen atom and its closest neighboring Au atom. The 2G-HDNNP energy curves displayed in Fig. 4.17 (a) differ by just a constant energy shift caused by the dopant atoms, which is analogous to the absence or presence of the additional sodium atom in the positively NaCl clusters. The resulting equilibrium bond length is  $2.26$  Å marked by a dot in Fig. 4.17 (a) for both cases, which is not in agreement with DFT results. In contrast, the 4G-HDNNP not only matches the equilibrium bond lengths with DFT for the undoped (4G-HDNNP:  $2.18$  Å; DFT:  $2.19$  Å) and doped (4G-HDNNP:  $2.34$  Å;

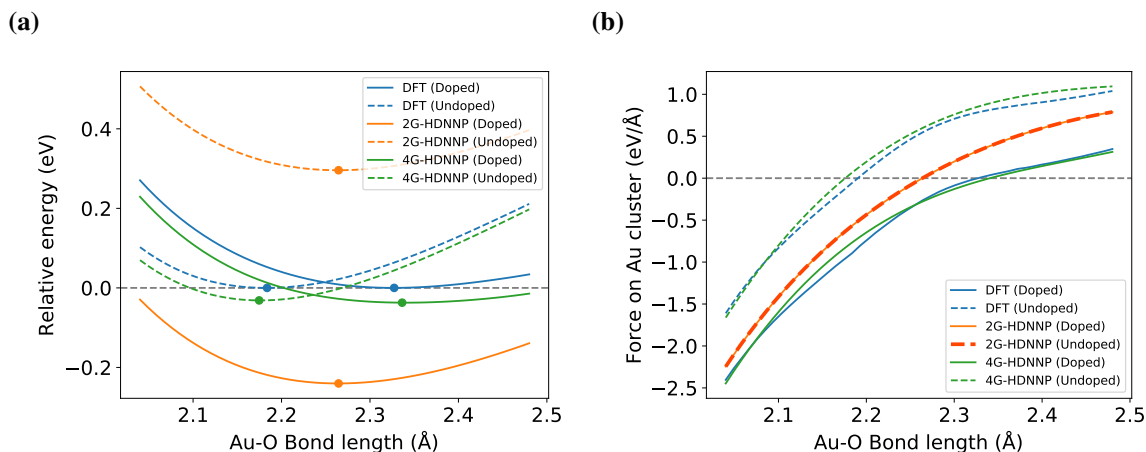


**Fig. 4.17:** Relative energies (a) and sum of atomic forces acting on an Au dimer (b) attached on the MgO(001) slab for the non-wetting geometry with the undoped and Al-doped cases. The equilibrium bond length are marked with a dot. The energies are shifted to the minimum of DFT total energy of the respective geometry. The bond length of Au-O refers to the bond distance between the O atom and the closest Au atom. Reprinted (adapted) with permission from Ref. [34]. Copyright 2021 Springer Nature.

DFT: 2.33 Å) cases, but also reproduces with DFT energy and force curves in excellent accuracy. Both results reveal the 4G-HDNNP is able to describe the non-local effects caused by long range charge transfer from the dopant atoms to the gold dimer.



# Chapter 5

## Electrostatically Embedded Fourth-Generation HDNNP

### 5.1 Motivation

The inability of MLPs relying on the concept of locality to describe non-local effects caused by long-range charge transfer and multiple charge states, is being solved by the emerging fourth-generation MLPs, which incorporate information about the global charge distribution. Despite a lot of improvements in the description of electrostatic interactions from second-generation to fourth-generation MLPs, a set of effective descriptors that accurately describe the electronic changes is currently missing. This leaves a large space for further improvements in accuracy and transferability of potentials. In the framework of 4G-HDNNPs, non-local effects arising from global changes in the electronic structure are mainly captured by the partial charge on the central atom, which serves as an input for a short-range ANN.

However, in some cases, this is still insufficient to describe changes of the electronic structure within the local environments. To illustrate this, the long carbon chain from Fig. 4.2 is investigated further (see Fig. 5.1 (a)). The fourth carbon atom from the left is slightly negatively charged. When the hydrogen atom is substituted by a lithium atom, as shown in Fig. 5.1 (b), the second carbon atom on the left side becomes positively charged while the partial charge on the fourth carbon is nearly unchanged. If the 4G-HDNNP is trained to a data set containing both configurations, the resulting atomic energy of the carbon atom predicted by the 4G-HDNNP will be very similar for both cases. It means that the 4G-HDNNP fails to describe the changes of the electronic structure in the local atomic environments due to the substitution.

A further example is the replacement of a hydrogen atom by a fluorine atom, while only relaxing the bond distance between the fluorine and carbon atoms as displayed in Fig. 5.1 (c). The second carbon atom on the left side becomes strongly negatively charged while the fourth carbon atom is very similar compared with panel (a). Due to lack of the

electronic structure information in the local atomic environment, the 4G-HDNNP is also unable to describe such non-local effects. Such illustrative examples show that there is still room for further improvements of 4G-HDNNPs in the description of non-local electronic changes, which are crucial for the construction of highly accurate potential energy surfaces.

Apart from the description of non-local effects, a more general limitation for the majority of MLPs is the limited transferability to unknown structures outside the training set. Some preliminary works have been done to address this problem such as the combination of pairwise potentials and MLPs [181]. The target energy of the MLPs is expressed as the difference between the reference total energy and two-body part by performing an iterative fitting for these two contributions separately. Apart from that, the simple two-body and three-body descriptors, which capture explicit two-body and three-body contributions, can be also included in the total energy expression of MLPs [182–184] as well. All these methods improve the transferability of the potentials such as providing a proper repulsion, when atoms are getting too close even though such atomic environments are not covered in the data set.

Based on these two possible improvements, a modified framework of the 4G-HDNNP, called the electrostatically embedded 4G-HDNNP (ee4G-HDNNP) is proposed. In the following sections, the methodology and technical details of the ee4G-HDNNP are introduced. Furthermore, the capabilities of the method demonstrated on a benchmark system including systematic comparisons to the original 4G-HDNNP implementation are also presented.

## 5.2 Method

### 5.2.1 Energy and Force Calculations

In the framework of ee4G-HDNNPs, two essential modifications have been done compared to the 4G-HDNNP. These are the improvement of the transferability by including two-body physical potentials, and the description of non-local effects by introducing a new set of non-local descriptors. The architecture of an ee4G-HDNNP for an arbitrary binary system is displayed in Fig. 5.2. The expression of the total energy contains the short-range energy  $E_{\text{short}}$ , the electrostatic energy  $E_{\text{elec}}$  without any truncation and the two-body potential  $E_{2b}$ ,

$$E_{\text{total}} = E_{\text{short}} + E_{\text{elec}} + E_{2b} \quad . \quad (5.1)$$

The electrostatic part of the ee4G-HDNNP is equivalent to the original 4G-HDNNP described in Sec. 4.1.1. The environment-dependent atomic electronegativities and element-dependent hardnesses are trained to reproduce the reference charges according to the Qeq scheme. These Gaussian charges are used to calculate electrostatic energies and forces

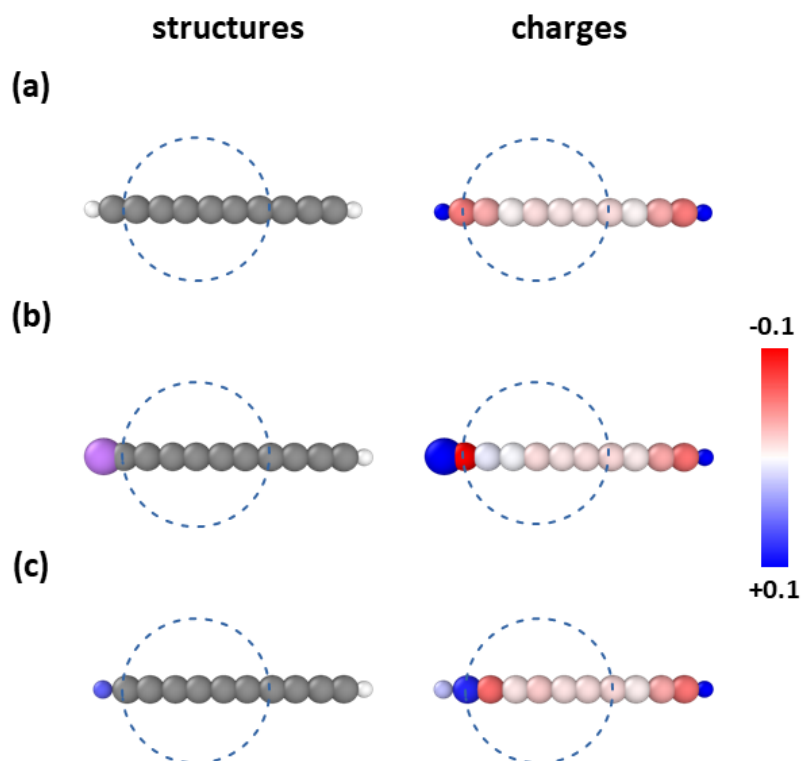


**Fig. 5.1:** Illustrative examples demonstrating the inability of 4G-HDNNPs to describe electronic changes in local atomic environments. The DFT-optimized geometry of  $C_{10}H_2$  and corresponding Hirshfeld charges are shown in panel (a). When the left hydrogen atom is replaced by a Li atom, the partial charge on the fourth C atom is almost the same but its neighboring charges are different as shown in panel (b). Another example is the substitution of the hydrogen atom by a F atom, while only relaxing the F-C bond, as displayed in panel (c). Again, the atomic charge on the fourth C atom is nearly unchanged but neighboring charges change. In both cases, the atomic energy of the fourth C atom obtained by the 4G-HDNNP is almost identical, due to the same atomic environment indicated by a dashed circle. These example show that 4G-HDNNPs cannot properly describe non-local effects arising from the changes of the electronic structure in the local atomic environment. The H, Li, C, F, atoms are colored in white, purple, grey and blue, respectively.

using Coulomb's law.

The first modification is to introduce an additional two-body term, which is inspired by the Tosi-Fumi potential [185, 186]. The functional form of the two-body term  $E_{2b}$  is

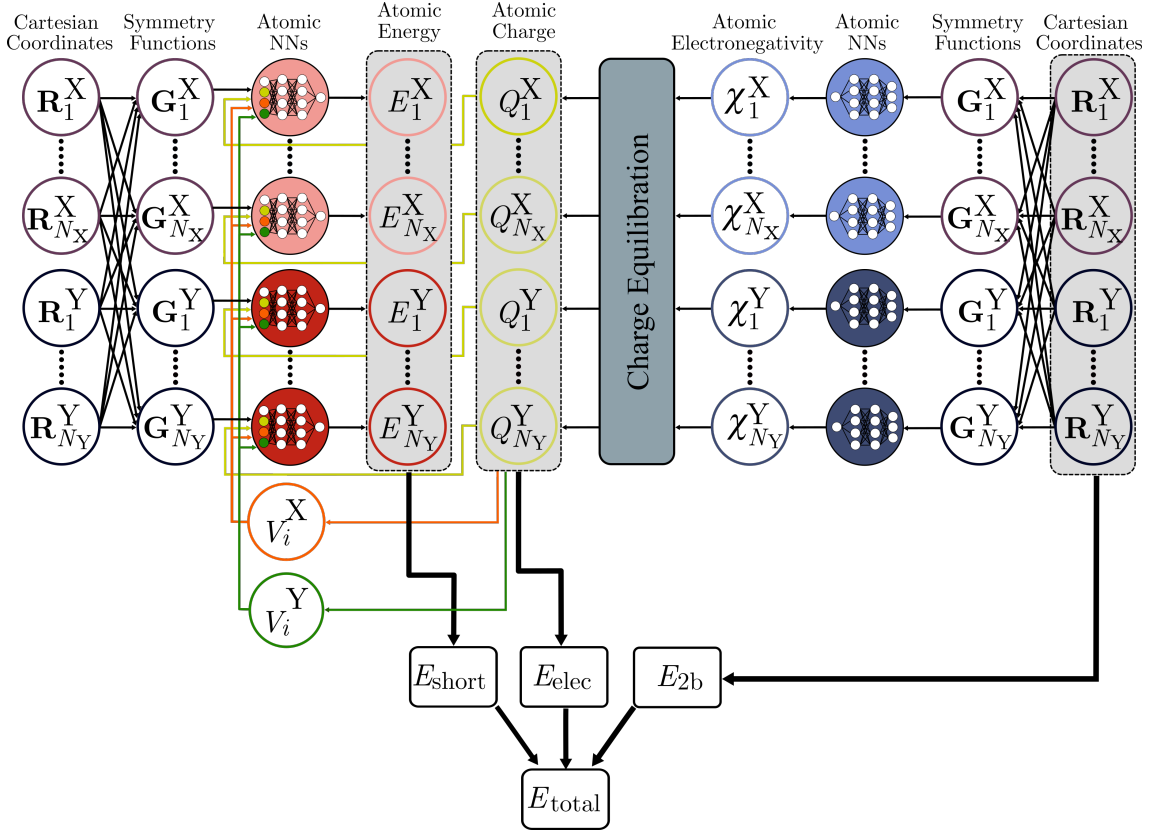


**Fig. 5.2:** Schematic diagram of an ee4G-HDNNP for a binary system. The total energy of the system containing  $N_X$  and  $N_Y$  atoms that belong to element  $X$  and  $Y$  respectively, consists of a short-range energy  $E_{\text{short}}$ , which is expressed as a sum of atomic energies  $E_i$ , an empirical two-body contribution  $E_{2b}$ , and the long-range electrostatic energy  $E_{\text{elec}}$ . The atomic charges  $Q_i$  are globally distributed according to the charge equilibration scheme employing environment-dependent electronegativities  $\chi_i$  predicted by atomic neural networks (right). These charges are used to calculate the electrostatic energy and element-dependent electrostatic potentials  $\{V_i\}$ , which serve as additional non-local inputs for the short-range atomic neural networks (left) yielding  $E_i$ . The local atomic environment are represented by atom-centered symmetry functions  $\{G_i\}$ , which depend on a set of Cartesian coordinates  $\mathbf{R}_i$  and serve as geometrical inputs for the atomic neural networks.

given by

$$E_{2b} = \sum_{i>j}^{N_{\text{atoms}}} \left( A_{ij} e^{B_{ij}(\mu_{ij}-R_{ij})} - \frac{C_{ij}}{R_{ij}^6} - \frac{D_{ij}}{R_{ij}^8} \right) \cdot f_{\text{cut}}(R_{ij}) \quad , \quad (5.2)$$

where  $A_{ij}, B_{ij}, C_{ij}, D_{ij}$ , and  $\mu_{ij}$  denote element-pair dependent training parameters that are extracted from a fit to binding energies for the dissociation of a dimer. The hyperbolic tangent cutoff function  $f_{\text{cut}}$  in Eq. 2.28 is employed to ensure the two-body energies and

forces smoothly decay to zero at the cutoff radius  $R_c$ . The cutoff radius for the two-body part can be larger than the cutoff used for the short-range part. This type of pairwise physical potential takes the Pauli repulsion, the dipole-dipole and the dipole-quadrupole van der Waals (vdW) interactions into account, which are not included in the framework of 4G-HDNNPs.

For the improvement of the description of non-local effects compared to the 4G-HDNNP, additional input information for the short-range part is considered. In the 4G-HDNNP approach, an accurate global distribution of charges over the system is already obtained by the Qeq scheme. However, the description of local bonding caused by the electronic changes still mainly relies on a single partial charge of the central atom. This means that the resulting atomic energies are independent of the neighboring charges, which describe the changes of the electronic structure within the local atomic environment.

To address this problem, a new kind of non-local descriptors is developed. These descriptors serve as additional non-local inputs for the short-range ANNs. The short-range energy in the framework of the 4G-HDNNP is expressed as the energy difference between the total energy and electrostatic energy. In contrast, the short-range energy  $E_{\text{short}}$  in the ee4G-HDNNP is expressed as the remaining energy after removing the two-body  $E_{2b}$  and electrostatic part  $E_{\text{elec}}$  from the total energy,

$$E_{\text{short}} = E_{\text{total}} - E_{\text{elec}} - E_{2b} = \sum_{i=1}^{N_{\text{atoms}}} E_i(\{G_i\}, Q_i, \{V_i\}) \quad . \quad (5.3)$$

Here  $E_i$  depends not only on the local atomic environment, which is described by ACSFs  $\{G_i\}$ , and its atomic charge  $Q_i$  but also on a new set of non-local descriptors  $\{V_i\}$ , which takes the electronic structure information from local atomic environments into account.

The functional form of the new descriptor is inspired by the Coulomb potential acting on the central atom arising from neighboring Gaussian charges within its local atomic environment. The electrostatic potentials are considered as local properties, which are consistent with short-range atomic energies. This means that the contribution of electrostatic potentials are only up to the range of the cutoff sphere.

Apart from that, the descriptors are calculated for each element individually. Otherwise, the contributions to the Coulomb potential of positive and negative partial charges within the cutoff radius would vanish, which reduces the resolution of the descriptors. Based on all these requirements, the expression of non-local descriptor  $V_i^j$  is written as

$$V_i^j = \sum_{k=1}^{N_{\text{neig},j}} \frac{\text{erf}\left(\frac{R_{ik}}{\sqrt{2}\gamma_{ik}}\right) Q_k}{R_{ik}} f_{\text{cut}}(R_{ik}) \quad , \quad (5.4)$$

where  $V_i^j$  is defined as the total electrostatic potential acting on the central atom  $i$  caused by all neighboring atoms  $k$  of element  $j$ . The contribution of the electrostatic potential

does not only depend on the distance between atom  $i$  and  $k$ , but also depend on the  $\gamma_{ik}$ , which is calculated using the width of Gaussian charge densities in Eq. 4.2. These novel non-local descriptors provide the information about the local charge distribution. They serve as additional inputs for short-range ANNs to describe local chemical bonding, which involves the changes of the electronic structure in the local atomic environment. Here  $f_{\text{cut}}$  employs the same functional form with a two-body part and  $R_c$  is set to the cutoff, which is used for the calculation of ACSFs. The total number of input neurons in the short-range part is equal to the sum of  $N_{\text{sym}}$  for the number of ACSFs, 1 for the atomic charge and  $N_{\text{elems}}$  for the number of elements in the system.

The short-range forces acting on atom  $k$  along the direction  $\alpha$  is

$$F_{k,\alpha}^{\text{short}} = - \left( \sum_{i=1}^{N_{\text{atoms}}} \sum_{j=1}^{N_{i,\text{sym}}} \frac{\partial E_i}{\partial G_{i,j}} \frac{\partial G_{i,j}}{\partial R_{k,\alpha}} + \sum_{i=1}^{N_{\text{atoms}}} \frac{\partial E_i}{\partial Q_i} \frac{\partial Q_i}{\partial R_{k,\alpha}} + \sum_{i=1}^{N_{\text{atoms}}} \sum_{j=1}^{N_{\text{elems}}} \frac{\partial E_i}{\partial V_i^j} \frac{\partial V_i^j}{\partial R_{k,\alpha}} \right), \quad (5.5)$$

where  $\frac{\partial V_i^j}{\partial R_{k,\alpha}}$  denotes the gradient of the electrostatic potential with respect to atomic positions, which can be calculated analytically using Eq. 5.4 by the chain rule. Such calculations do not cause much computational cost since the required physical quantities such as the partial derivatives of the charges with respect to atomic positions are already computed from the original framework of 4G-HDNNP.

## 5.2.2 Training Stage

The training phase of ee4G-HDNNP can be separated into three steps. The first step is to train the atomic electronegativities expressed by ANNs and hardnesses to reproduce the reference charges. This is the same as for 4G-HDNNP. The second step is to construct the empirical two-body potentials by fitting the dissociation curves of a dimer. The third step is to train the short-range ANNs to reproduce the remaining energy after removing the two-body and electrostatic contributions from the target total energies and forces.

In this way the training of the short-range part is analogous to the  $\Delta$ -learning approach [187, 188] that aims to predict accurate but computationally intensive properties based on cheaper baseline methods by learning the difference between both methods through machine learning. For instance, the difference between the high level DFT and the baseline level density functional tight binding method with self-consistent charges can be accurately reproduced by a MLP [189]. Another example is to predict the expensive hybrid functional or non-local vdW functionals in DFT by learning the difference with HDNNPs based on the cheap PBE functional with a minimal atomic basis set [190]. These  $\Delta$ -learning approaches are able to considerably improve the transferability and

accuracy by using a smaller amount of data points. In this work, DFT is the high-level method and the two-body empirical potential is the low-level method. The difference between the two methods is reproduced by the short-range and electrostatic part in the ee4G-HDNNP.

The energy training requires the partial derivatives of the energy with respect to the neural network weights, which can be directly calculated through back-propagation depending on the architecture of the ANNs. The force training requires the following derivatives:

$$\begin{aligned} \frac{\partial F_{k,\alpha}}{\partial W_l} = & - \left( \sum_{i=1}^{N_{\text{atoms}}} \sum_{j=1}^{N_{\text{sym},i}} \frac{\partial G_{i,j}}{\partial R_{k,\alpha}} \cdot \frac{\partial}{\partial W_l} \frac{\partial E_i}{\partial G_{i,j}} + \sum_{i=1}^{N_{\text{atoms}}} \frac{\partial Q_i}{\partial R_{k,\alpha}} \cdot \frac{\partial}{\partial W_l} \frac{\partial E_i}{\partial Q_i} \right. \\ & \left. + \sum_{i=1}^{N_{\text{atoms}}} \sum_{j=1}^{N_{\text{elems}}} \frac{\partial V_i^j}{\partial R_{k,\alpha}} \cdot \frac{\partial}{\partial W_l} \frac{\partial E_i}{\partial V_i^j} \right) , \end{aligned} \quad (5.6)$$

where the first two terms are equivalent with 4G-HDNNP and the last term is used to optimize the weights for the non-local force contributions depending on the electrostatic potentials.

In order to have a systematic investigation on the role of both methodical extensions in the framework of 4G-HDNNPs, a 4G-HDNNP with only two-body empirical potentials (4G-HDNNP+ $E_{2b}$ ) is also developed for comparison. The short-range target energy is the same as for ee4G-HDNNP, except that the local electrostatic potential descriptor does not enter its functional form:

$$E_{\text{short}} = E_{\text{total}} - E_{\text{elec}} - E_{2b} = \sum_{i=1}^{N_{\text{atoms}}} E_i(\{G_i\}, Q_i) . \quad (5.7)$$

Here, the main difference between ee4G-HDNNP and 4G-HDNNP+ $E_{2b}$  is the functional form of the short-range atomic energies. In 4G-HDNNP+ $E_{2b}$ , the atomic energies only depend on ACSFs and atomic charges while ee4G-HDNNP depends on additional non-local descriptors  $\{V_i\}$  arising from the electrostatic potentials. It is noted that the training of short-range part in 4G-HDNNP+ $E_{2b}$  is equal to 4G-HDNNP except for the target short-range energies and forces, which are the difference after removing two-body and electrostatic parts from the reference total energies and forces.

## 5.3 Comparison of Fourth-Generation MLPs on Sodium Chloride Clusters

Finding a proper system to systematically compare the performance between 4G-HDNNP and ee4G-HDNNP is crucial. Here, sodium chloride clusters were chosen as a benchmark system due to their large structural diversity and electrostatic interactions, which changes

significantly depending on the total charge of the system. The details of reference data generation are described in chapter 3. To compare the individual improvements on the accuracy and transferability of the potential made by the two different modifications in ee4G-HDNNP, the 4G-HDNNP, 4G-HDNNP+ $E_{2b}$  and ee4G-HDNNP were constructed on the same training set. Moreover, the same settings for the ANNs including the number of hidden layers and neurons, the activation function, and other training details, as provided in chapter 3, were chosen. Parameters for the ACSFs are given in Tab. A.5.

All two-body potential parameters were extracted by fitting to the dimer dissociation curves of Na-Na, Cl-Cl, and Na-Cl through the non-linear least squares method. It is noted that the interactions of Na-Cl in the framework of ee4G-HDNNP and 4G-HDNNP+ $E_{2b}$  involve electrostatic contributions during the dissociation which need to be removed to avoid double counting of the electrostatic interactions. In this work, the electrostatic interaction between Na and Cl atoms was simply calculated using Coulomb's law based on fixed point charges by setting Na = +1 and Cl = -1. The details of the fitting process and parameters are given in Sec. A.3. The detailed comparisons of 4G-HDNNP, 4G-HDNNP+ $E_{2b}$  and ee4G-HDNNP in different aspects are presented in the following subsections.

### 5.3.1 Accuracy of Fourth-Generation MLPs

A straight forward estimation for the accuracy of the constructed potentials is to compare the errors in the training and test set. The correlation of binding energies, atomic forces and charges between different potentials and DFT is plotted in Fig. 5.3. The 4G-HDNNP achieves overall state-of-the-art accuracy with respect to the binding energies, force components, and atomic charges. However, certain data points in the correlation plot of the force components (see Fig. 5.3 (d)) are scattered, often reaching several eV/Å with respect to DFT. Notably, the settings in the non-local electrostatic part of the 4G-HDNNP, 4G-HDNNP+ $E_{2b}$  and ee4G-HDNNP are identical. As a consequence, the calculation of charges, electrostatic energies and forces is exactly the same for all methods, which provide a fair comparison for evaluating the improvement of each modification.

In contrast, the 4G-HDNNP+ $E_{2b}$  predicts a significantly improved correlation of force components and binding energies compared to the 4G-HDNNP as shown in Fig. 5.3 (b) and (e). Nevertheless, some force components still deviate strongly from the reference. Finally, the ee4G-HDNNP predicts DFT binding energies and force components in excellent agreement with DFT and only a few force components are scattered as shown in the correlation plot. These remaining outliers of force components can be explained by very close neighboring atoms with relatively large charge errors, which give an inaccurate input for the short-range part yielding large force errors. In summary, these correlation plots show that the accuracy of the training and test set is gradually improved from 4G-HDNNP over 4G-HDNNP+ $E_{2b}$  to ee4G-HDNNP.

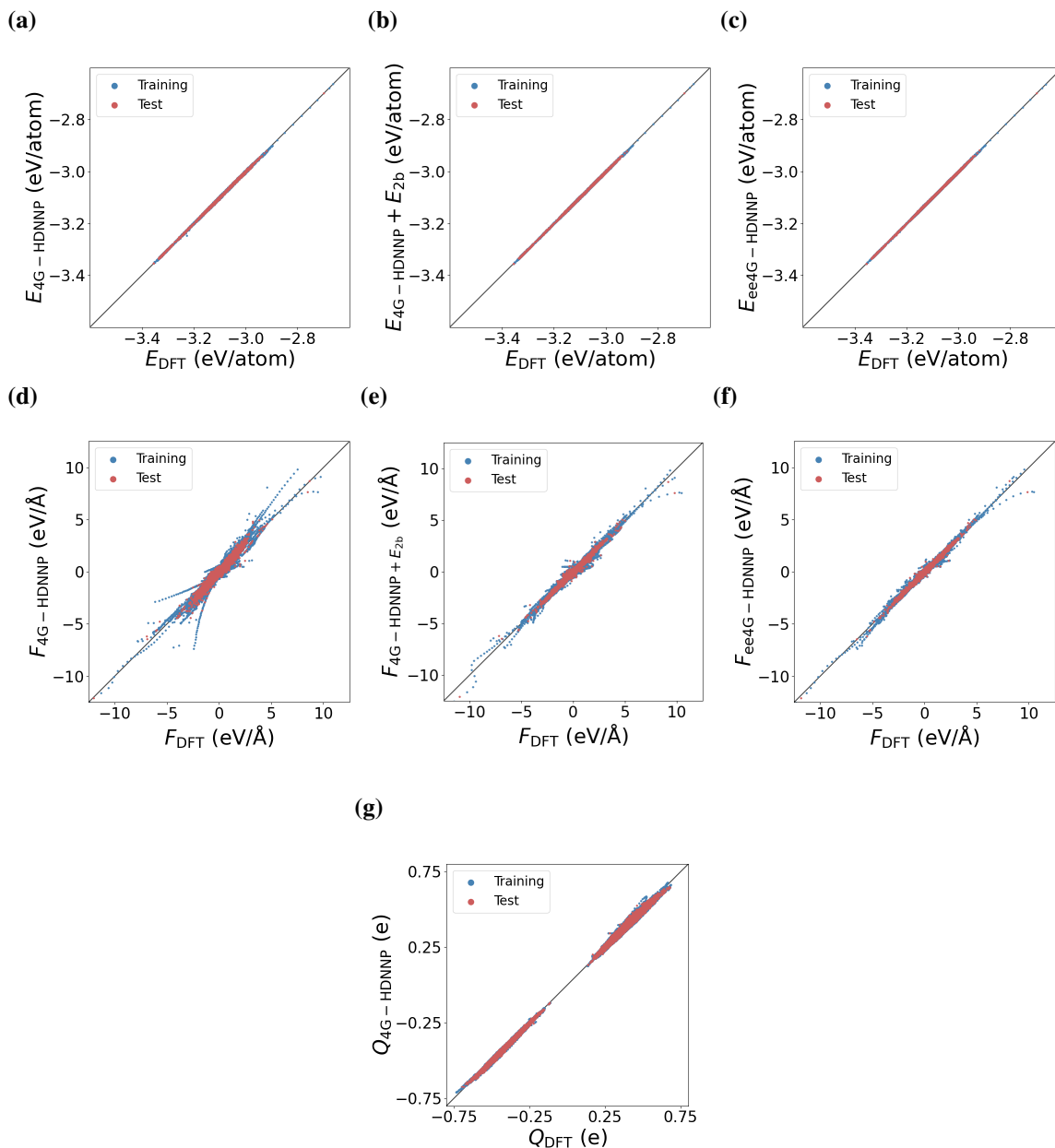


**Fig. 5.3:** Correlation plots of binding energies obtained from the 4G-HDNNP (a), 4G-HDNNP+ $E_{2b}$  (b), ee4G-HDNNP (c), atomic force components obtained from the 4G-HDNNP (d), 4G-HDNNP+ $E_{2b}$  (e), ee4G-HDNNP (f), and atomic charges obtained from 4G-HDNNP (g) in the training and test set for sodium chloride clusters. The charge calculations are the same for all methods.

More statistical information about the accuracy of the different fourth-generation potentials can be extracted from the RMSEs of charges, binding energies and force components as reported in Tab. 5.1. The 4G-HDNNP is in agreement with DFT for all target

**Tab. 5.1:** Root mean square errors of charges ( $10^{-3}$  e), binding energies (meV/atom) and force components (meV/Å) for the data set of NaCl clusters. The training and test sets contain 30196 and 3396, respectively. Numbers in brackets indicate the errors of the test set. The 4G-HDNNP+ $E_{2b}$  and ee4G-HDNNP share same settings with the 4G-HDNNP for charge calculations.

method	charges	binding energies	force components
4G-HDNNP	6.904 (6.912)	1.779 (1.796)	64.78 (63.70)
4G-HDNNP+ $E_{2b}$	6.904 (6.912)	1.391 (1.381)	39.45 (39.38)
ee4G-HDNNP	6.904 (6.912)	1.250 (1.267)	34.76 (34.94)

properties, which are below  $7.0 \times 10^3$  e, 1.8 meV/atom and 0.065 eV/Å, respectively. The errors of 4G-HDNNP+ $E_{2b}$  are reduced by roughly 30% compared to 4G-HDNNP in terms of binding energies and force components, while the ee4G-HDNNP is further decreased by 10%. The learning curve of potentials are provided in Fig. A.6. At first glance, the significant improvement is attributed to the empirical two-body potentials, which can be also seen in the correlation plots. However, only including the two-body potential is still insufficient for describing non-local effects, which arise from dramatic changes of the electronic structure in the local atomic environments. Such situations are further investigated in the next subsection.

### 5.3.2 A Benchmark for Ionic Clusters

To demonstrate the capabilities of ee4G-HDNNP, the non-local effects caused by an additional chloride ion attached on the DFT-optimized structure of  $\text{Na}_6\text{Cl}_6$  with a bond distance of 2.7 Å (see Fig. 5.4) are investigated with different potentials. It is noteworthy that these two structures are not included in the training set. The charge distribution of both structures obtained by 4G-HDNNP are shown in Fig. 5.4 (a).

The partial charge on the additional chloride ion is around  $-0.66$  e and its nearest sodium atom becomes less positively charged from 0.47 e to 0.30 e while the nearest chlorine atom remains nearly unchanged. The additional chloride ion considerably changes the electronic structure of the neighboring atoms and the corresponding chemical interactions. To compare the performance of different potentials in describing such electronic changes, the force errors for each atom obtained by different potentials with respect to DFT for both clusters are displayed in the color plot from Fig. 5.4 (b) to (d).

For the case of  $\text{Na}_6\text{Cl}_6$ , the RMSEs of the forces obtained with the 4G-HDNNP, 4G-HDNNP+ $E_{2b}$  and ee4G-HDNNP compared to DFT are 0.055, 0.037 and 0.032 eV/Å. All of them are in very good agreement with DFT and their force error for each atom is also similar. For the case of  $\text{Na}_6\text{Cl}_7^-$ , the RMSEs of atomic forces are generally higher than for  $\text{Na}_6\text{Cl}_6$  (4G-HDNNP: 0.121 eV/Å; 4G-HDNNP+ $E_{2b}$ : 0.131 eV/Å; ee4G-HDNNP:

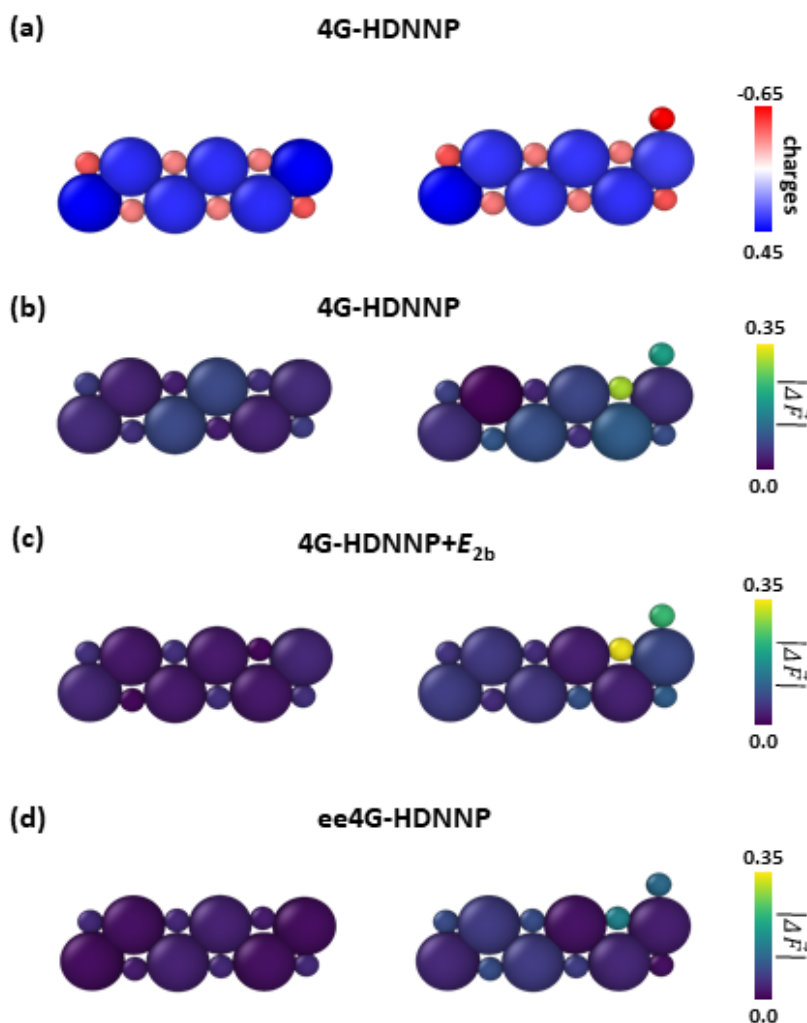


**Fig. 5.4:** Investigation of non-local effects arising from the additional  $\text{Cl}^-$  ion attached on the DFT-optimized structure of  $\text{Na}_6\text{Cl}_6$ . Atomic charges for both structures predicted by 4G-HDNNP are displayed in (a). The force error of 4G-HDNNP (b), 4G-HDNNP+ $E_{2b}$  (c), ee4G-HDNNP (d) for the atoms in both structures are plotted with respect to DFT. The Na and Cl atoms are indicated as large and small spheres, respectively.

0.078 eV/Å). This can be explained by a very small number of training structures which contain a highly negatively charged chlorine atom. Therefore, such chemical interactions between neighboring atoms within the atomic environment are not well described by the ANNs compared to the neutral system.

The force error for each atom is also investigated to identify other possible reasons. The 4G-HDNNP predicts a large force error of the additional chlorine ion and its nearest chlo-

rine atom with respect to DFT (0.2 and 0.307 eV/Å, respectively). The 4G-HDNNP+ $E_{2b}$  is even worse than the 4G-HDNNP with RMSEs of 0.24 and 0.344 eV/Å. In contrast, the ee4G-HDNNP significantly reduces the force error for the additional chlorine ion and its nearest chlorine atom to 0.123 and 0.158 eV/Å.

This benchmark example reveals that the ee4G-HDNNP significantly improves the description of non-local effects, which are caused by the electronic changes in the surroundings of the central atom. This is attributed to the novel descriptors, which incorporate electrostatic potentials arising from the atomic environment. However, the 4G-HDNNP and 4G-HDNNP+ $E_{2b}$  cannot be properly adjusted to the electronic changes in the atomic environment. It can be explained by the lack of explicit information about the neighboring charges in these models, which cannot identify the partial charge on the additional chlorine ion. Such short coming leads to a unrealistically large short-range force between these two chlorine atoms, resulting in a higher force error with respect to DFT.

The even higher force error obtained from the 4G-HDNNP+ $E_{2b}$  compared to the 4G-HDNNP in this particular configuration is attributed to the pairwise potential of Cl-Cl. In the training of the short-range part of 4G-HDNNP+ $E_{2b}$ , the target values of energies and forces are obtained by subtracting the electrostatic and two-body contributions from the reference data. As the two-body potential has very strong covalent interactions, which increases the range of the target forces. This also increases the complexity of the fitting in the short-range part, which results in a higher force error.

### 5.3.3 Structural Analysis and Energetic Ordering of Local Minima

After showing the improved description of non-local electronic effects on a benchmark example, several analyses are performed for a set of local minima for both neutral and charged sodium chloride clusters obtained from different methods. The structures of minima and corresponding energetic orders are investigated with different methods to evaluate the general accuracy of the potentials in diverse configuration spaces. The minima hopping algorithm [137] was applied to explore different minima on the PESs. Moreover, small clusters have been chosen for the simulations, since the normalized relative energy difference per atom between two energetically similar minima for large clusters is extremely small, which is even lower than the typical energy error ( $\sim 1$  meV/atom) of MLPs.

The minima hopping simulations were driven by the ee4G-HDNNP and the detected minima were re-optimized with 4G-HDNNP, 4G-HDNNP+ $E_{2b}$  and DFT. In this way, the same initial structure is relaxed to the closest minimum on the respective PESs. Various sizes of sodium chloride cluster including  $\text{Na}_n\text{Cl}_n$ ,  $\text{Na}_n\text{Cl}_{n+1}^-$ , and  $\text{Na}_{n+1}\text{Cl}_n^+$  with  $n = 24, 62$  are studied. Here, the positively charged clusters were also included to test the

transferability of potentials for describing systems with the unknown charge state. The first 50 minima found in the minima hopping simulation were used for performing the analysis. Fig. 5.5 shows the RMSD in terms of the structures and DFT forces for the 50

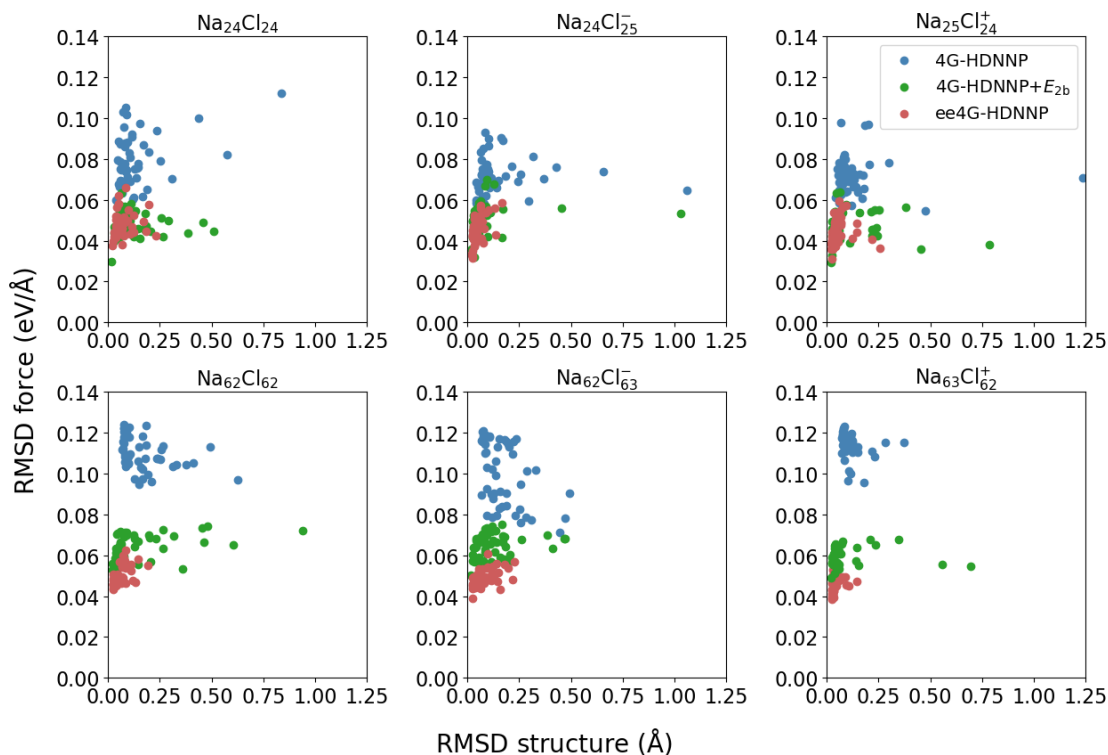


**Fig. 5.5:** Root mean square deviation of the structures and DFT forces for 50 minima obtained with 4G-HDNNP, 4G-HDNNP+ $E_{2b}$  and ee4G-HDNNP compared to the respective DFT minima. The tool for calculating the root mean square deviation of structures was provided by Jonas Finkler [174].

minima in each system size found by different potentials, compared to the respective DFT minima. If the data points are located at the bottom left region in the correlation plot, it means that the minima predicted by the potentials are in excellent agreement with DFT, energetically and structurally.

About 50% of the minima for smaller clusters obtained from the 4G-HDNNP reach state-of-the-art accuracy, which is below  $0.09 \text{ eV/\AA}$  and  $0.1 \text{ \AA}$ . Notably, the quality of the 4G-HDNNP for positively charged clusters is similar to neutral and negatively charged clusters, which reveals the excellent transferability of the 4G-HDNNP to the unknown charge state. Still, some minima predicted by the 4G-HDNNP deviate more than  $0.5 \text{ \AA}$  with respect to the DFT, which means the shape of PESs at the respective configuration space is different. Moreover, the average force deviation is increased by about  $0.03 \text{ eV/\AA}$  for larger clusters compared to smaller clusters, since some atomic environments for large clusters are not covered in the training set, which results in large force deviations.

The significant improvement of 4G-HDNNP+ $E_{2b}$  in regard to the deviation of structures and DFT forces can be observed in Fig. 5.5. More than 70% of minima show less than 0.1 Å structural deviation and around 80% of minima deviate below 0.065 eV/Å from the DFT forces. Additionally, the average DFT force deviation for larger clusters predicted by 4G-HDNNP+ $E_{2b}$  is slightly increased by 0.013 eV/Å compared to the case of smaller clusters. This shows that the transferability of the model can be substantially increased by including two-body potentials. However, a few minima still have large structural deviations, which are more than 0.5 Å, with respect to DFT.

Finally, the ee4G-HDNNP demonstrates outstanding accuracy and transferability compared to the other potentials. More than 80% of minima are below 0.1 Å in terms of structural deviations, and for above 95% the average DFT force deviation is lower than 0.06 eV/Å. Besides, the average force deviation from smaller to larger clusters is just increased by up to 0.005 eV/Å. These results show that the accuracy and transferability of the potentials for describing systems with larger sizes and different charge states are further enhanced by introducing electronic structure information in the local atomic environments.

Apart from the statistical comparison of minima in terms of structures and forces, the energetic ordering of minima is also studied. This is a meaningful comparison of the performance of 4G- and ee4G-HDNNPs, since the prediction of the correct energetic ordering of minima requires an accurate representation of the PES. The minima of  $\text{Na}_{25}\text{Cl}_{24}^+$  and  $\text{Na}_{63}\text{Cl}_{62}^+$  found in the minima hopping simulation were used to evaluate the accuracy of the energetic ordering predicted by 4G- and ee4G-HDNNPs compared to DFT.

Fig. 5.6 (a) shows the five lowest energies of  $\text{Na}_{25}\text{Cl}_{24}^+$  predicted by 4G-HDNNP, ee4G-HDNNP and DFT relative to the respective lowest energy of the minimum. It also depicts the corresponding structural differences as indicated by the RMSD compared to DFT. The 4G-HDNNP predicts qualitatively incorrect relative energies compared to DFT, which can be seen in the energy level given in Fig. 5.6 (a). Even though three out of five minima are accurately reproduced with structural deviations of approximately 0.06-0.07 Å with respect to DFT, only two minima are in exactly the same energetic order as DFT, while other minima either have large structural deviation or are not among the five lowest minima predicted by DFT. In contrast to that, the energetic ordering of minima predicted by the ee4G-HDNNP is equivalent to DFT. The corresponding relative energies are also in excellent agreement with DFT, which are even below the training accuracy of the potential. Moreover, all structures deviate less than 0.05 Å with respect to DFT minimum structures.

For the larger clusters  $\text{Na}_{63}\text{Cl}_{62}^+$ , the normalized relative energy difference per atom between minima can be very small and therefore the minima with the highest relative energies are included for comparisons. Fig. 5.6 (b) shows energetic ordering of the two lowest and the three highest energy minima obtained from DFT, 4G- and ee4G-HDNNPs. Three out of five minima obtained from the 4G-HDNNP agree with the energetic order

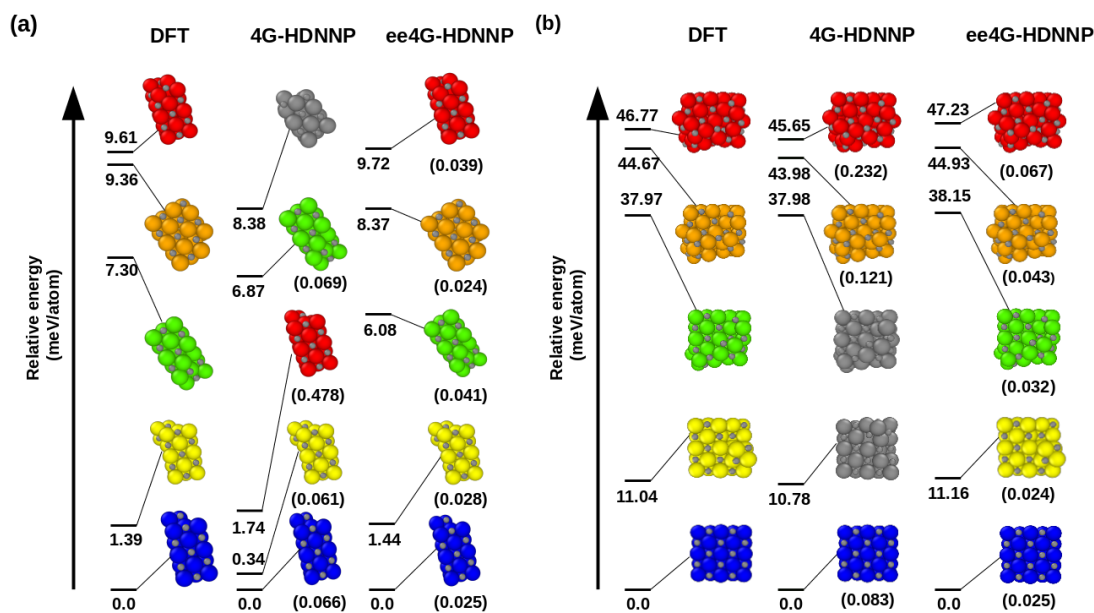


**Fig. 5.6:** Energetic ordering of minima predicted by 4G-HDNNP, ee4G-HDNNP and DFT. The five lowest energy minima of  $\text{Na}_{25}\text{Cl}_{24}^+$  are shown in (a). The three highest energy and two lowest energy minima of  $\text{Na}_{63}\text{Cl}_{62}^+$  are shown in (b). All minima are obtained from minima hopping simulations driven by the ee4G-HDNNP and then re-optimized with the respective methods. The numbers indicate the relative energy to the lowest energy minima predicted by the respective method. The numbers in brackets show the corresponding root mean square deviation (in Å) of the structure compared to the respective DFT minima. Mismatched structures with respect to DFT are colored in grey. The sodium and chlorine atoms are indicated as large and small spheres, respectively.

of DFT and all relative energy differences are within 1 meV/atom, although the structural deviation with respect to DFT is more than 0.1 Å for the high energy minima. In contrast, the ee4G-HDNNP predicts the DFT energetic order of minima very well with relative energy differences below 0.5 meV/atom. Besides, the structural deviation for all minima with respect to DFT is still significantly lower than 0.1 Å, which demonstrate the excellent transferability of the model from small to large systems. This analysis reveals that the ee4G-HDNNP is not only able to accurately reproduce the curvature of DFT-based PESs but also the corresponding energies.

### 5.3.4 Transferability to Crystals

The final comparison between 4G-HDNNP and ee4G-HDNNP is to evaluate the transferability of potentials to a periodic system based on the data set, which only contains

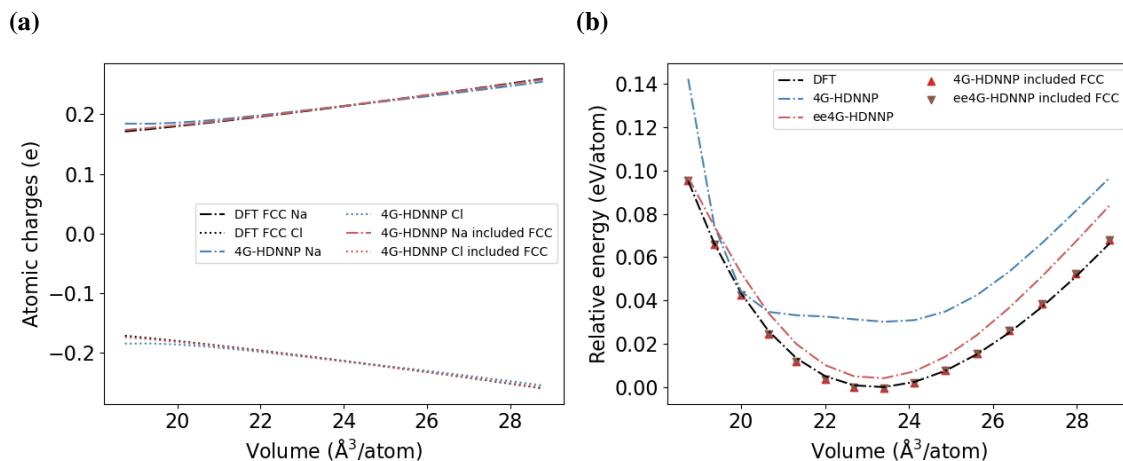


**Fig. 5.7:** Atomic charges (a) and Relative energies (b) versus normalized volume per atom for FCC crystal obtained from 4G-HDNNP, ee4G-HDNNP, both potentials constructed based on the data set including crystal structures and DFT. The energies are relative to the minimum of DFT energies.

cluster structures, by predicting the properties of the NaCl FCC bulk crystal. Fig. 5.7 (a) shows the changes of partial charges on Na and Cl atoms during isotropic compression or expansion. The charges on the Na and Cl atoms predicted by 4G-HDNNP based on the data set including additional crystal structures are able to reproduce the DFT Hirshfeld charges with very high accuracy. Remarkably, the charges predicted by the 4G-HDNNP based on the original cluster data set also give comparable accuracy to the data set with crystal structures, which underlines the excellent transferability of the Qeq scheme.

The relative energies obtained with DFT, 4G-HDNNP and ee4G-HDNNP corresponding to the isotropic deformation of a FCC crystal are plotted in Fig. 5.7 (b). The 4G- and ee4G-HDNNPs constructed on the data set including additional crystal structures match the DFT energy curve as indicated by the triangle symbols in the plot. However, the 4G-HDNNP constructed on the data set without including crystal structures fails to reproduce the curvature and minimum of the DFT energy curve while the ee4G-HDNNP predicts all these properties in acceptable agreement with DFT. The mean absolute error calculated from the ee4G-HDNNP is 8.462 meV/atom while the 4G-HDNNP has an error of 24.978 meV/atom.

The equilibrium lattice constant of the crystal and bulk modulus can be extracted by utilizing the Murnaghan equation of state [191]. The fitted DFT bulk modulus and equilibrium are 23.32 GPa and 5.706  $\text{\AA}$ . The ee4G-HDNNP predicts 25.79 GPa for the bulk modulus and 5.708  $\text{\AA}$  for the equilibrium bond length, which is in agreement with DFT results. On the other hand, the properties obtained by the 4G-HDNNP show larger deviations compared to DFT, which are 28.73 GPa and 5.602  $\text{\AA}$  respectively. This transferability test demonstrates the significant improvement provided by physical two-body

potentials, which explicitly take Pauli repulsive potentials and dispersion interactions into account.



## Part III

# Conclusion and Bibliography



# Chapter 6

## Summary and Perspectives

The development of machine learning potentials (MLPs) nowadays has reached an important milestone that enables large-scale atomistic simulations with nearly ab-initio accuracy at significantly reduced computational cost. Numerous applications of MLPs have been reported in chemistry, physics and materials science. The MLPs are classified into four different generations [16, 79], which give an overview for the historical development of MLPs over the past two decades.

First-generation MLPs have been introduced 25 years ago and they are only applicable to systems with a few degrees of freedom such as an molecule on a fixed slab. Starting from applications to high-dimensional systems based on second-generation MLPs, the development of MLPs has attracted a great deal of attention. Many models relying on the chemical locality combined with either predefined or learnable type descriptors have been proposed. The long-range interactions such as electrostatics can be described by third-generation MLPs, which rely on local environment dependent charges predicted by machine learning models. Apart from that, the dispersion interactions can be also included by using empirical corrections [75, 77, 192].

In recent years, fourth-generation MLPs have been proposed to describe non-local effects caused by long-range charge transfer and different total charge states, which overcome the long-standing challenge for previous generations of MLPs. A novel model, namely the fourth-generation high-dimensional neural network potential (4G-HDNNP), which is inspired by the charge equilibration using neural network technique (CENT) and the second-generation high-dimensional neural network potential (2G-HDNNP), is introduced in chapter 4 including the development of the conceptual approach and the technical details. A charge equilibration (Qeq) scheme is used to distribute the partial charges over the whole system according to the total charge. The environment-dependent atomic electronegativities, which are expressed by ANNs, and element-specific hardnesses are trained to reproduce the reference charges. Environment-dependent electronegativities, which are predicted by atomic neural networks. These Gaussian distributed charges are used to calculate long-range electrostatic energies and forces. Furthermore, the atomic charges also serve as non-local input for the short-range ANNs together with atom-centered symmetry func-

tions (ACSFs) to describe the local bonding. In this way, the short-range atomic energies are able to take non-local effects arising from the global redistribution of atomic charges into account.

The capabilities of 4G-HDNNPs have been demonstrated on a wide range of systems including an organic molecule, ionic and charged metal clusters, and bulk materials, which involve long-range charge transfer or multiple charge states. These results illustrate that the 4G-HDNNPs provide excellent agreement with the underlying DFT results in terms of charges, energies and forces. In contrast, previous generations of HDNNPs yield even qualitatively wrong results for these benchmark systems, which involve non-local effects arising from long-range charge transfer or multiple charge states. For instance, some equilibrium structures are missed by the 2G- and 3G-HDNNPs. On the other hand, the 4G-HDNNP is able to identify these structures in agreement with DFT. All these results illustrate that the 4G-HDNNP is generally applicable and enables replacing computationally demanding electronic structure methods for performing large-scale atomistic simulations to study complex problems.

Moreover, the accuracy and transferability of the 4G-HDNNP have been further enhanced by proposing the electrostatically embedded 4G-HDNNP (ee4G-HDNNP), which contains two essential modifications with respect to the 4G-HDNNP. The first change is to introduce a new kind of non-local electronic descriptors, which take the electrostatic potential arising from Gaussian charges within the local atomic environment into account. Just like the atomic charges in the 4G-HDNNP, these non-local descriptors serve as inputs for short-range ANNs to determine the atomic energies. Hence, the representation of atomic energies is more completed in terms of the distribution of atomic charges within the local environment, which considerably improve the description of overall PES. Furthermore, the transferability of the potential can be substantially increased by including physical pairwise potentials that account for Pauli repulsion, dipole-dipole, and dipole-quadruple vdW interactions.

The noticeable improvements of the ee4G-HDNNP compared to the 4G-HDNNP have been demonstrated on a data set containing both neutral and charged sodium chloride clusters with large structural diversity in chapter 5. The results reveal that the ee4G-HDNNP predicts the structure of minima and corresponding energetic orderings in excellent agreement with DFT, while the minima obtained by the 4G-HDNNP have larger structural deviations and only partially correct energetic orderings. Besides, the ee4G-HDNNP exhibits outstanding transferability to crystal structures compared to the 4G-HDNNP based on a data set only containing cluster structures. All these analyses confirm that the ee4G-HDNNP provides a significant improved PES, which offers a more accurate description of non-local electronic effects with excellent transferability to unknown structures. In terms of computational cost, the performance of 2G-, 4G-, and ee4G-HDNNPs for a NaCl FCC supercell with different number of atoms is displayed in Fig. 6.1. It shows that the additional computational effort caused by the ee4G-HDNNP relative to the 4G-HDNNP is negligible. On the other hand, the computational time of the local methods such as

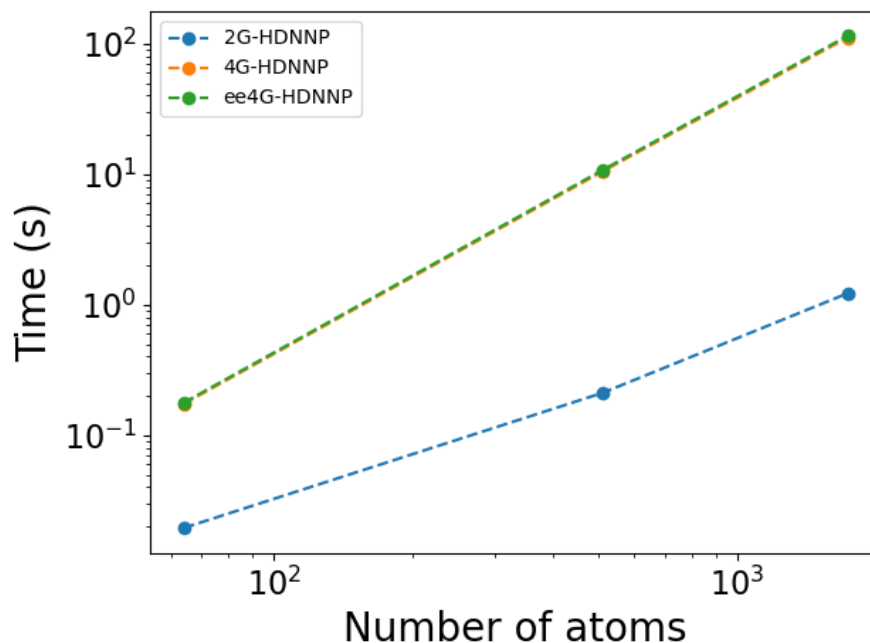


**Fig. 6.1:** Computational time spent on the energy and force calculations with the RuNner program for a NaCl FCC supercell with different number of atoms  $N_{\text{atoms}} = 64, 512, 1728$  using 2G-, 4G-, and ee4G-HDNNPs by four Intel<sup>®</sup> Xeon Gold 6240 CPU cores. The RuNner program was compiled with the OpenMP parallelization flag. The data points are calculated by taking the average of total run time for 100 identical structures and plotted on a logarithmic scale.

2G-HDNNP is significantly shorter than for 4G- and ee4G-HDNNPs. For example, the 2G-HDNNP takes only 1.22 s for the energy and force calculation of a single structure containing 1728 atoms while 4G- and ee4G-HDNNPs consume 111.36 s and 114.84 s, respectively.

The main bottle neck of computational speed in 4G- and ee4G-HDNNPs is the calculation of charges and their derivatives, which involves  $O(N^3)$  of the standard algorithm for solving the linear systems of equations. One of the solutions is to employ an iterative solver, which can effectively reduce the scaling to  $O(N \log N)$  with number of atoms  $N$ . Apart from that, the electrostatic energies and forces are currently computed using standard Ewald summation, which can be replaced by more efficient algorithms such as the fast multipole [163] and particle mesh Ewald methods [164]. These modifications are expected to considerably reduce the computational cost for the energy and force calculations using 4G- and ee4G-HDNNPs, which will allow to efficiently simulate systems with more than ten thousand atoms in the future. It can be foreseen that the ee4G-HDNNP will serve as a powerful tool to study interesting electrochemical phenomena such as the mechanisms and kinetics of interfacial electron transfer in the solid electrolyte interphase [193, 194].

For future work, the construction of two-body potentials in the framework of ee4G-HDNNPs requires further investigation. The coefficients of two-body potentials are currently determined by fitting the dissociation curve of different dimers, which generally improves the accuracy and transferability of 4G-HDNNPs. However, the introduction of such two-body potentials sometimes provides worse extrapolation for exceptional configurations, which contain strongly charged atoms with atomic environments that are not sampled well in the training set. For instance, the 4G-HDNNP reproduces more accurate DFT forces on  $\text{Na}_6\text{Cl}_7^-$  compared to the 4G-HDNNP+ $E_{2b}$  as shown in Fig. 5.4. This is attributed to the unrealistically large short-range contributions which remain after removing the strong covalent interactions provided by the pairwise potential. Open questions remain about how the introduction of such pairwise potentials with strong covalent bonding between two neutral atoms influences the accuracy and transferability of the potential. Due to time constraints, a detailed analysis will be conducted in the future.

In terms of further methodical developments, a general limitation of the Qeq scheme is that it always allows long-range charge transfer for all types of systems. However, this is only valid for conductor-like systems such as conjugated hydrocarbons and metals [195, 196]. This problem could yield large charge errors for the studies of bond dissociation at large distance. Some early attempts have been done to address the problem of unrealistic long-range charge transfer such as putting artificial constraints on fragment charges [197, 198] and increasing the impact of the electronegativity difference at long distances [199, 200]. Work in this direction to improve long-range charge transfer in the framework of 4G-HDNNPs will continue in the future. Apart from that, the costly solution of the system of linear equations in the Qeq scheme can be avoided by introducing effective local learnable atomic electronegativities. These electronegativities implicitly include the off-diagonal terms (i.e. the Coulomb interaction terms) in the matrix by iteratively updating through message passing neural networks [89]. In this simplification of the Qeq scheme, the charges can be calculated analytically without solving a system of linear equations and the efficiency is thus substantially increased.

In addition to the improvements of the Qeq scheme in terms of accuracy and efficiency, the framework of 4G-HDNNPs can be further extended to magnetic systems, where the model is currently unable to distinguish different electronic spin arrangements due to the lack of atomic spin information. A set of spin dependent atom-centered symmetry functions (SACSFs) [130], which take collinear atomic spins into account, have been recently proposed for the construction of HDNNPs to describe materials in different magnetic states. The possible extension of the 4G-HDNNP to magnetic systems can be done by predicting the atomic spins and employing SACSFs, which describe the arrangement of atomic spins within the local environment. These SACSFs serve as inputs for short-range ANNs together with other descriptors to predict atomic contributions arising from different magnetic states.

Fourth-generation MLPs are emerging as a tool for atomistic simulations and relevant developments are constantly reported in this field of research. For example, the non-local

---

effects arising from the changes of the electronic structure can be described by the position of the maximally localized Wannier centers (MLWFCs) [201, 202]. The MLWFCs, which are suggested to be local properties, and their electronic responses due to the applied electric field over the whole system are predicted by two different sets of neural networks. This electronic information provides an alternative way for constructing fourth-generation MLPs instead of using atomic charges, which depend on the chosen partitioning scheme.

Even though fourth-generation MLPs can describe non-local effects arising from long-range charge transfer and multiple charge states, explicit electronic degrees of freedoms are still missing. Another new direction in the field is to combine MLPs with information obtained from electronic structure methods. Further examples include the combination of neural networks with Hückel theory [203] or density functional tight binding [204] obtained by message passing neural networks as well as the representation of symmetry-adapted atomic orbital features [205]. In addition, highly accurate molecular electronic wave functions can be represented by deep neural networks relying on the baseline Hartree-Fock method [206]. Such direction of including more electronic information from ab-initio methods can be expected to continue in the coming years.

Due to the capabilities of fourth-generation MLPs, many studies of interesting phenomena involving global changes in the electronic structure, which cannot be described by previous generations of MLPs, become feasible. These encouraging developments leads to more general applicability of MLPs in different fields of science. In this thesis, the framework and algorithms of 4G- and ee4G-HDNNPs are presented, along with a detailed analysis for various benchmark systems and possible improvements to the methods. All these works would give valuable insights for the further development of next-generation MLPs, which provide an accurate description of non-local electronic effects and excellent transferability to unknown structures. The definition of a future fifth-generation of MLPs is still not clear. However, more promising developments of MLPs can be anticipated in this highly active field of research.



# Bibliography

- [1] M. Urban, J. Noga, S. J. Cole, and R. J. Bartlett, *J. Chem. Phys.* **83**, 4041 (1985).
- [2] J. A. Pople, J. S. Binkley, and R. Seeger, *Int. J. Quantum Chem.* **10**, 1 (1976).
- [3] G. D. Purvis III and R. J. Bartlett, *J. Chem. Phys.* **76**, 1910 (1982).
- [4] R. Krishnan and J. A. Pople, *Int. J. Quantum Chem.* **14**, 91 (1978).
- [5] T. Helgaker, S. Coriani, P. Jørgensen, K. Kristensen, J. Olsen, and K. Ruud, *Chem. Rev.* **112**, 543 (2012).
- [6] R. A. Friesner, *Annu. Rev. Phys. Chem.* **42**, 341 (1991).
- [7] B. J. Alder and T. E. Wainwright, *J. Chem. Phys.* **27**, 1208 (1957).
- [8] B. J. Alder and T. E. Wainwright, *J. Chem. Phys.* **31**, 459 (1959).
- [9] N. Metropolis, A. W. Rosenbluth, M. N. Rosenbluth, A. H. Teller, and E. Teller, *J. Chem. Phys.* **21**, 1087 (1953).
- [10] J. Tersoff, *Phys. Rev. Lett.* **61**, 2879 (1988).
- [11] J. Tersoff, *Phys. Rev. B* **39**, 5566 (1989).
- [12] A. C. Van Duin, S. Dasgupta, F. Lorant, and W. A. Goddard, *J. Phys. Chem. A* **105**, 9396 (2001).
- [13] A. D. MacKerell Jr, *J. Comput. Chem.* **25**, 1584 (2004).
- [14] J. A. Harrison, J. D. Schall, S. Maskey, P. T. Mikulski, M. T. Knippenberg, and B. H. Morrow, *Appl. Phys. Rev.* **5**, 031104 (2018).
- [15] F. Dommert, K. Wendler, R. Berger, L. Delle Site, and C. Holm, *ChemPhysChem* **13**, 1625 (2012).
- [16] J. Behler, *Chemical Reviews* **121**, 10037 (2021).
- [17] V. L. Deringer, A. P. Bartók, N. Bernstein, D. M. Wilkins, M. Ceriotti, and G. Csányi, *Chem. Rev.* **121**, 10073 (2021).

- [18] O. T. Unke, S. Chmiela, H. E. Sauceda, M. Gastegger, I. Poltavsky, K. T. Schütt, A. Tkatchenko, and K.-R. Müller, *Chem. Rev.* **121**, 10142 (2021).
- [19] R. S. Michalski, J. G. Carbonell, and T. M. Mitchell, *Machine learning: An artificial intelligence approach* (Springer Science & Business Media, 2013).
- [20] S. Shalev-Shwartz and S. Ben-David, *Understanding machine learning: From theory to algorithms* (Cambridge university press, 2014).
- [21] E. Alpaydin, *Introduction to Machine Learning* (MIT press, 2020).
- [22] A. J. Hey, S. Tansley, K. M. Tolle, *et al.*, *The fourth paradigm: data-intensive scientific discovery*, Vol. 1 (Microsoft research Redmond, WA, 2009).
- [23] C. M. Handley and P. L. A. Popelier, *J. Phys. Chem. A* **114**, 3371 (2010).
- [24] J. Behler, *Phys. Chem. Chem. Phys.* **13**, 17930 (2011).
- [25] J. Behler, *J. Chem. Phys.* **145**, 170901 (2016).
- [26] P. O. Dral, *J. Phys. Chem. Lett.* **11**, 2336 (2020).
- [27] V. L. Deringer, M. A. Caro, and G. Csányi, *Adv. Mater.* **31**, 1902765 (2019).
- [28] F. Noé, A. Tkatchenko, K.-R. Müller, and C. Clementi, *Ann. Rev. Phys. Chem.* **71**, 361 (2020).
- [29] T. Zubatiuk and O. Isayev, *Acc. Chem. Res.* **54**, 1575 (2021).
- [30] J. Zhang, Y.-K. Lei, Z. Zhang, J. Chang, M. Li, X. Han, L. Yang, Y. I. Yang, and Y. Q. Gao, *J. Phys. Chem. A* **124**, 6745 (2020).
- [31] P. Friederich, F. Häse, J. Proppe, and A. Aspuru-Guzik, *Nat. Mater.* **20**, 750 (2021).
- [32] A. Grisafi, J. Nigam, and M. Ceriotti, *Chem. Sci.* **12**, 2078 (2021).
- [33] E. Kocer, T. W. Ko, and J. Behler, *Annu. Rev. Phys. Chem.* **73**, 163 (2022).
- [34] T. W. Ko, J. A. Finkler, S. Goedecker, and J. Behler, *Nat. Commun.* **12**, 398 (2021).
- [35] T. B. Blank, S. D. Brown, A. W. Calhoun, and D. J. Doren, *J. Chem. Phys.* **103**, 4129 (1995).
- [36] K. T. No, B. H. Chang, S. Y. Kim, M. S. Jhon, and H. A. Scheraga, *Chem. Phys. Lett.* **271**, 152 (1997).
- [37] L. M. Raff, M. Malshe, M. Hagan, D. I. Doughan, M. G. Rockley, and R. Komanduri, *J. Chem. Phys.* **122**, 084104 (2005).
- [38] H. M. Le and L. M. Raff, *J. Chem. Phys.* **128**, 194310 (2008).

- [39] D. F. R. Brown, M. N. Gibbs, and D. C. Clary, *J. Chem. Phys.* **105**, 7597 (1996).
- [40] A. C. P. Bittencourt, F. V. Prudente, and J. D. M. Vianna, *Chem. Phys.* **297**, 153 (2004).
- [41] J. Behler, K. Reuter, and M. Scheffler, *Phys. Rev. B* **77**, 115421 (2008).
- [42] S. Manzhos and K. Yamashita, *Surf. Sci.* **604**, 554 (2010).
- [43] D. A. R. S. Latino, R. P. S. Fartaria, F. F. M. Freitas, J. A. de Sousa, and F. M. S. S. Fernandes, *J. Electroanal. Chem.* **624**, 109 (2008).
- [44] S. Manzhos and T. Carrington, Jr, *J. Chem. Phys.* **125**, 194105 (2006).
- [45] S. Manzhos and T. Carrington, Jr, *J. Chem. Phys.* **127**, 014103 (2007).
- [46] S. Manzhos and T. Carrington, Jr, *J. Chem. Phys.* **129**, 224104 (2008).
- [47] M. Malshe, R. Narulkar, L. M. Raff, M. Hagan, S. Bukkapatnam, P. M. Agrawal, and R. Komanduri, *J. Chem. Phys.* **130**, 184102 (2009).
- [48] B. Jiang and H. Guo, *J. Chem. Phys.* **139**, 054112 (2013).
- [49] A. E. Allen, G. Dusson, C. Ortner, and G. Csányi, *Mach. learn.: sci. technol.* **2**, 025017 (2021).
- [50] J. Behler and M. Parrinello, *Phys. Rev. Lett.* **98**, 146401 (2007).
- [51] M. S. Daw and M. I. Baskes, *Phys. Rev. B* **29**, 6443 (1984).
- [52] J. Behler, *J. Chem. Phys.* **134**, 074106 (2011).
- [53] A. P. Bartók, M. C. Payne, R. Kondor, and G. Csányi, *Phys. Rev. Lett.* **104**, 136403 (2010).
- [54] Z. Deng, C. Chen, X.-G. Li, and S. P. Ong, *npj Comput. Mater.* **5**, 75 (2019).
- [55] A. V. Shapeev, *Multiscale Model. Simul.* **14**, 1153 (2016).
- [56] R. Drautz, *Phys. Rev. B* **99**, 014104 (2019).
- [57] A. P. Bartók, R. Kondor, and G. Csányi, *Phys. Rev. B* **87**, 184115 (2013).
- [58] M. Rupp, A. Tkatchenko, K.-R. Müller, and O. A. Von Lilienfeld, *Phys. Rev. Lett.* **108**, 058301 (2012).
- [59] N. Artrith, A. Urban, and G. Ceder, *Phys. Rev. B* **96**, 014112 (2017).
- [60] J. Gilmer, S. S. Schoenholz, P. F. Riley, O. Vinyals, and G. E. Dahl, in *International conference on machine learning* (PMLR, 2017) pp. 1263–1272.

- [61] K. T. Schütt, F. Arbabzadah, S. Chmiela, K. R. Müller, and A. Tkatchenko, *Nat. Commun.* **8**, 1 (2017).
- [62] K. T. Schütt, H. E. Saucedo, P.-J. Kindermans, A. Tkatchenko, and K.-R. Müller, *J. Chem. Phys.* **148**, 241722 (2018).
- [63] R. Zubatyuk, J. S. Smith, J. Leszczynski, and O. Isayev, *Sci. Adv.* **5**, eaav6490 (2019).
- [64] N. L. Allinger, Y. H. Yuh, and J. H. Lii, *J. Am. Chem. Soc.* **111**, 8551 (1989).
- [65] A. K. Rappé, C. J. Casewit, K. Colwell, W. A. Goddard III, and W. M. Skiff, *J. Am. Chem. Soc.* **114**, 10024 (1992).
- [66] W. D. Cornell, P. Cieplak, C. I. Bayly, I. R. Gould, K. M. Merz, D. M. Ferguson, D. C. Spellmeyer, T. Fox, J. W. Caldwell, and P. A. Kollman, *J. Am. Chem. Soc.* **117**, 5179 (1995).
- [67] S. L. Mayo, B. D. Olafson, and W. A. Goddard, *J. Phys. Chem.* **94**, 8897 (1990).
- [68] S. Houlding, S. Liem, and P. Popelier, *Int. J. Quantum Chem.* **107**, 2817 (2007).
- [69] F. Pereira and J. Aires-de Sousa, *J. Cheminform.* **10**, 1 (2018).
- [70] A. E. Sifain, N. Lubbers, B. T. Nebgen, J. S. Smith, A. Y. Lokhov, O. Isayev, A. E. Roitberg, K. Barros, and S. Tretiak, *J. Phys. Chem. Lett.* **9**, 4495 (2018).
- [71] M. Veit, D. M. Wilkins, Y. Yang, R. A. DiStasio Jr, and M. Ceriotti, *J. Chem. Phys.* **153**, 024113 (2020).
- [72] N. Artrith, T. Morawietz, and J. Behler, *Phys. Rev. B* **83**, 153101 (2011).
- [73] T. Morawietz, V. Sharma, and J. Behler, *J. Chem. Phys.* **136**, 064103 (2012).
- [74] K. Yao, J. E. Herr, D. W. Toth, R. Mckintyre, and J. Parkhill, *Chem. Sci.* **9**, 2261 (2018).
- [75] S. Grimme, *J. Comput. Chem.* **27**, 1787 (2006).
- [76] O. T. Unke and M. Meuwly, *J. Chem. Theory Comput.* **15**, 3678 (2019).
- [77] S. Grimme, J. Antony, S. Ehrlich, and H. Krieg, *J. Chem. Phys.* **132**, 154104 (2010).
- [78] A. Stukowski, *Modell. Simul. Mater. Sci. Eng.* **18**, 015012 (2010).
- [79] T. W. Ko, J. A. Finkler, S. Goedecker, and J. Behler, *Acc. Chem. Res.* **54**, 808 (2021).

- [80] T. Hoshino, N. Papanikolaou, R. Zeller, P. Dederichs, M. Asato, T. Asada, and N. Stefanou, *Comp. Mat. Sci.* **14**, 56 (1999).
- [81] B. Parsaeifard, D. S. De, J. A. Finkler, and S. Goedecker, *Condens. Matter Phys.* **6**, 9 (2021).
- [82] S. A. Ghasemi, A. Hofstetter, S. Saha, and S. Goedecker, *Phys. Rev. B* **92**, 045131 (2015).
- [83] A. K. Rappe and W. A. Goddard, III, *J. Phys. Chem.* **95**, 3358 (1991).
- [84] S. Faraji, S. A. Ghasemi, S. Rostami, R. Rasoulkhani, B. Schaefer, S. Goedecker, and M. Amsler, *Phys. Rev. B* **95**, 104105 (2017).
- [85] R. Rasoulkhani, H. Tahmasbi, S. A. Ghasemi, S. Faraji, S. Rostami, and M. Amsler, *Phys. Rev. B* **96**, 064108 (2017).
- [86] X. Xie, K. A. Persson, and D. W. Small, *J. Chem. Theory Comput.* **16**, 4256 (2020).
- [87] O. T. Unke, S. Chmiela, M. Gastegger, K. T. Schütt, H. E. Sauceda, and K.-R. Müller, *Nat. Commun.* **12**, 1 (2021).
- [88] R. Zubatyuk, J. S. Smith, B. T. Nebgen, S. Tretiak, and O. Isayev, *Nat. Commun.* **12**, 1 (2021).
- [89] L. D. Jacobson, J. M. Stevenson, F. Ramezanghorbani, D. Ghoreishi, K. Leswing, E. D. Harder, and R. Abel, *J. Chem. Theory Comput.* **18**, 2354 (2022).
- [90] L. Scalfi, M. Salanne, and B. Rotenberg, *Annu. Rev. Phys. Chem.* **72**, 189 (2021).
- [91] M. Born and R. Oppenheimer, *Ann. Phys. (Berl.)* **389**, 457 (1927).
- [92] P. Hohenberg and W. Kohn, *Phys. Rev.* **136**, B864 (1964).
- [93] L. H. Thomas, in *Math. Proc. Camb. Philos. Soc.*, Vol. 23 (Cambridge University Press, 1927) pp. 542–548.
- [94] J. Demmel, *Concurr. Comput. Pract. Exp* **3**, 655 (1991).
- [95] J. Choi, J. Demmel, I. Dhillon, J. Dongarra, S. Ostrouchov, A. Petitet, K. Stanley, D. Walker, and R. C. Whaley, *Comput. Phys. Commun.* **97**, 1 (1996).
- [96] J. P. Perdew and K. Schmidt, in *AIP Conf. Proc.*, Vol. 577 (American Institute of Physics, 2001) pp. 1–20.
- [97] K. Burke, *J. Chem. Phys.* **136**, 150901 (2012).
- [98] N. Mardirossian and M. Head-Gordon, *Mol. Phys.* **115**, 2315 (2017).

- [99] J. P. Perdew, J. A. Chevary, S. H. Vosko, K. A. Jackson, M. R. Pederson, D. J. Singh, and C. Fiolhais, *Phys. Rev. B* **46**, 6671 (1992).
- [100] D. C. Langreth and M. Mehl, *Phys. Rev. B* **28**, 1809 (1983).
- [101] J. P. Perdew, *Phys. Rev. Lett.* **55**, 1665 (1985).
- [102] J. P. Perdew and W. Yue, *Phys. Rev. B* **33**, 8800 (1986).
- [103] A. D. Beck, *J. Chem. Phys.* **98**, 5648 (1993).
- [104] S. H. Vosko, L. Wilk, and M. Nusair, *Can. J. Phys.* **58**, 1200 (1980).
- [105] J. P. Perdew, K. Burke, and M. Ernzerhof, *Phys. Rev. Lett.* **77**, 3865 (1996).
- [106] A. D. Becke, *Phys. Rev. A* **38**, 3098 (1988).
- [107] C. Lee, W. Yang, and R. G. Parr, *Phys. Rev. B* **37**, 785 (1988).
- [108] W. Li, A. A. Jaroń-Becker, C. W. Hogle, V. Sharma, X. Zhou, A. Becker, H. C. Kapteyn, and M. M. Murnane, *Proc. Natl. Acad. Sci. U.S.A.* **107**, 20219 (2010).
- [109] R. S. Mulliken, *J. Chem. Phys.* **23**, 1833 (1955).
- [110] P.-O. Löwdin, *J. Chem. Phys.* **18**, 365 (1950).
- [111] C. Kern and M. Karplus, *J. Chem. Phys.* **40**, 1374 (1964).
- [112] L. C. Cusachs and P. Politzer, *Chem. Phys. Lett.* **1**, 529 (1968).
- [113] F. L. Hirshfeld, *Theor. Chim. Acta* **44**, 129 (1977).
- [114] J. S. Smith, O. Isayev, and A. E. Roitberg, *Chem. Sci.* **8**, 3192 (2017).
- [115] M. Gastegger, L. Schwiedrzik, M. Bittermann, F. Berzsényi, and P. Marquetand, *J. Chem. Phys.* **148**, 241709 (2018).
- [116] M. Liu and J. R. Kitchin, *J. Phys. Chem. C* **124**, 17811 (2020).
- [117] J. Weinreich, M. L. Paleico, and J. Behler, *J. Phys. Chem. C* **125**, 14897 (2021).
- [118] H. Ghorbanfekr, J. Behler, and F. M. Peeters, *J. Phys. Chem. Lett.* **11**, 7363 (2020).
- [119] M. L. Paleico and J. Behler, *J. Chem. Phys.* **153**, 054704 (2020).
- [120] M. Eckhoff and J. Behler, *J. Chem. Theory Comput.* **15**, 3793 (2019).
- [121] M. A. Strauss and H. A. Wegner, *Eur. J. Org. Chem.* **2019**, 295 (2019).
- [122] T. Morawietz, A. Singraber, C. Dellago, and J. Behler, *Proc. Natl. Acad. Sci. U.S.A.* **113**, 8368 (2016).

- [123] J. Yu, S. B. Sinnott, and S. R. Phillpot, *Phys. Rev. B* **75**, 085311 (2007).
- [124] T.-R. Shan, B. D. Devine, J. M. Hawkins, A. Asthagiri, S. R. Phillpot, S. B. Sinnott, *et al.*, *Phys. Rev. B* **82**, 235302 (2010).
- [125] N. Onofrio and T. W. Ko, *J. Phys. Chem. C* **123**, 9486 (2019).
- [126] D. Raymond, A. C. Van Duin, M. Baudin, and K. Hermansson, *Surf. Sci.* **602**, 1020 (2008).
- [127] T.-R. Shan, B. D. Devine, T. W. Kemper, S. B. Sinnott, S. R. Phillpot, *et al.*, *Phys. Rev. B* **81**, 125328 (2010).
- [128] K. Choudhary, T. Liang, A. Chernatynskiy, Z. Lu, A. Goyal, S. R. Phillpot, and S. B. Sinnott, *J. Condens. Matter Phys.* **27**, 015003 (2014).
- [129] K. Chenoweth, A. C. Van Duin, and W. A. Goddard, *J. Phys. Chem. A* **112**, 1040 (2008).
- [130] M. Eckhoff and J. Behler, *Npj Comput. Mater.* **7**, 1 (2021).
- [131] P. Ewald, *Ann. Phys. (Berl.)* **369**, 253 (1921).
- [132] H. A. Eivari, S. A. Ghasemi, H. Tahmasbi, S. Rostami, S. Faraji, R. Rasoulkhani, S. Goedecker, and M. Amsler, *Chem. Mater.* **29**, 8594 (2017).
- [133] H. Tahmasbi, S. Goedecker, and S. A. Ghasemi, *Phys. Rev. Mater.* **5**, 083806 (2021).
- [134] W. C. Swope, H. C. Andersen, P. H. Berens, and K. R. Wilson, *J. Chem. Phys.* **76**, 637 (1982).
- [135] W. F. Van Gunsteren and H. J. Berendsen, *Mol. Simul.* **1**, 173 (1988).
- [136] D. Frenkel and B. Smit, *Understanding molecular simulation: from algorithms to applications* (Elsevier, 2001).
- [137] S. Goedecker, *J. Chem. Phys.* **120**, 9911 (2004).
- [138] A. Warshel and W. W. Parson, *Q. Rev. Biophys.* **34**, 563 (2001).
- [139] F. Calvo and F. Spiegelmann, *J. Chem. Phys.* **112**, 2888 (2000).
- [140] G. Trégliã, B. Legrand, F. Ducastelle, A. Saúl, C. Gallis, I. Meunier, C. Mottet, and A. Senhaji, *Comput. Mater. Sci.* **15**, 196 (1999).
- [141] M. Amsler and S. Goedecker, *J. Chem. Phys.* **133**, 224104 (2010).
- [142] K. Binder, D. Heermann, L. Roelofs, A. J. Mallinckrodt, and S. McKay, *Comput. Phys.* **7**, 156 (1993).

- [143] D. Landau and K. Binder, *A guide to Monte Carlo simulations in statistical physics* (Cambridge university press, 2021).
- [144] S. Rostami, S. A. Ghasemi, and S. Goedecker, *Phys. Rev. Mater.* **5**, 123603 (2021).
- [145] E. Rahmatizad Khajehpasha, S. Goedecker, and S. A. Ghasemi, *J. Comput. Chem.* **42**, 699 (2021).
- [146] V. Blum, R. Gehrke, F. Hanke, P. Havu, V. Havu, X. Ren, K. Reuter, and M. Scheffler, *Comput. Phys. Commun.* **180**, 2175 (2009).
- [147] E. v. Lenthe, E.-J. Baerends, and J. G. Snijders, *J. Chem. Phys.* **99**, 4597 (1993).
- [148] J. D. Head and M. C. Zerner, *Chem. Phys. Lett.* **122**, 264 (1985).
- [149] D. J. Evans and B. L. Holian, *J. Chem. Phys.* **83**, 4069 (1985).
- [150] L. Genovese, B. Videau, M. Ospici, T. Deutsch, S. Goedecker, and J.-F. Méhaut, *C. R. Mécanique* **339**, 149 (2011).
- [151] T. M. Faro, G. P. Thim, and M. S. Skaf, *J. Chem. Phys.* **132**, 114509 (2010).
- [152] J. Zhang and M. Dolg, *Phys. Chem. Chem. Phys.* **17**, 24173 (2015).
- [153] D. Karaboga and B. Akay, *Artif. Intell. Rev.* **31**, 61 (2009).
- [154] J. Behler, “RuNNer – a program for constructing high-dimensional neural network potentials, Universität Göttingen 2020.” (Universität Göttingen, 2020).
- [155] J. Behler, *Int. J. Quantum Chem.* **115**, 1032 (2015).
- [156] J. Behler, *Angew. Chem. Int. Ed.* **56**, 12828 (2017).
- [157] D. Nguyen and B. Widrow, in *1990 IJCNN International Joint Conference on Neural Networks* (IEEE, 1990) pp. 21–26.
- [158] S. E. Schönborn, S. Goedecker, S. Roy, and A. R. Oganov, *J. Chem. Phys.* **130**, 144108 (2009).
- [159] I. Leven, H. Hao, S. Tan, X. Guan, K. A. Penrod, D. Akbarian, B. Evangelisti, M. J. Hossain, M. M. Islam, J. P. Koski, *et al.*, *J. Chem. Theory Comput.* (2021).
- [160] K. A. O’Hearn, A. Alperen, and H. M. Aktulga, *SIAM J. Sci. Comput.* **42**, C1 (2020).
- [161] B. A. Wells and A. L. Chaffee, *J. Chem. Theory Comput.* **11**, 3684 (2015).
- [162] J. W. Perram, H. G. Petersen, and S. W. De Leeuw, *Mol. Phys.* **65**, 875 (1988).
- [163] T. Amisaki, *J. Comput. Chem.* **21**, 1075 (2000).

- [164] T. Darden, D. York, and L. Pedersen, *J. Chem. Phys.* **98**, 10089 (1993).
- [165] T. R. Gingrich and M. Wilson, *Chem. Phys. Lett.* **500**, 178 (2010).
- [166] T. B. Blank and S. D. Brown, *J. Chemom.* **8**, 391 (1994).
- [167] P. P. Poier, L. Lagardère, J.-P. Piquemal, and F. Jensen, *J. Chem. Theory Comput.* **15**, 6213 (2019).
- [168] Q. Fan and G. V. Pfeiffer, *Chem. Phys. Lett.* **162**, 472 (1989).
- [169] L. Horný, N. D. Petracò, and H. F. Schaefer, *J. Am. Chem. Soc.* **124**, 14716 (2002).
- [170] L. Pan, B. Rao, A. Gupta, G. Das, and P. Ayyub, *J. Chem. Phys.* **119**, 7705 (2003).
- [171] A. S. Chaves, G. G. Rondina, M. J. Piotrowski, P. Tereshchuk, and J. L. Da Silva, *J. Phys. Chem. A* **118**, 10813 (2014).
- [172] C.-G. Li, Z.-G. Shen, Y.-F. Hu, Y.-N. Tang, W.-G. Chen, and B.-Z. Ren, *Sci. Rep.* **7**, 1 (2017).
- [173] M. L. McKee and A. Samokhvalov, *J. Phys. Chem. A* **121**, 5018 (2017).
- [174] J. A. Finkler and S. Goedecker, *J. Chem. Phys.* **152**, 164106 (2020).
- [175] Z.-J. Zhao, Z. Li, Y. Cui, H. Zhu, W. F. Schneider, W. N. Delgass, F. Ribeiro, and J. Greeley, *J. Catal.* **345**, 157 (2017).
- [176] Y. Cui, Z. Li, Z. Zhao, V. J. Cybulskis, K. D. Sabnis, C. W. Han, V. Ortolan, W. F. Schneider, J. Greeley, W. N. Delgass, *et al.*, *Catal. Sci. Technol.* **7**, 5257 (2017).
- [177] M. Haruta and M. Daté, *Appl. Catal. A: Gen.* **222**, 427 (2001).
- [178] L. Molina and B. Hammer, *Phys. Rev. B* **69**, 155424 (2004).
- [179] N. Artrith, B. Hiller, and J. Behler, *Phys. Status Solidi B* **250**, 1191 (2013).
- [180] K. Momma and F. Izumi, *J. Appl. Crystallogr.* **41**, 653 (2008).
- [181] P. E. Dolgirev, I. A. Kruglov, and A. R. Oganov, *AIP Adv.* **6**, 085318 (2016).
- [182] P. Rowe, G. Csányi, D. Alfè, and A. Michaelides, *Phys. Rev. B* **97**, 054303 (2018).
- [183] P. Rowe, V. L. Deringer, P. Gasparotto, G. Csányi, and A. Michaelides, *J. Chem. Phys.* **153**, 034702 (2020).
- [184] V. L. Deringer and G. Csányi, *Phys. Rev. B* **95**, 094203 (2017).
- [185] M. Tosi and F. Fumi, *J. Phys. Chem. Solids* **25**, 45 (1964).
- [186] J. Anwar, D. Frenkel, and M. G. Noro, *J. Chem. Phys.* **118**, 728 (2003).

- [187] R. Ramakrishnan, P. O. Dral, M. Rupp, and O. A. von Lilienfeld, *J. Chem. Theory Comput.* **11**, 2087 (2015).
- [188] P. O. Dral, A. Owens, A. Dral, and G. Csányi, *J. Chem. Phys.* **152**, 204110 (2020).
- [189] M. Fernandez, A. Bilić, and A. S. Barnard, *Nanotechnology* **28**, 38LT03 (2017).
- [190] G. Sun and P. Sautet, *J. Chem. Theory Comput.* **15**, 5614 (2019).
- [191] F. D. Murnaghan, *Proc. Natl. Acad. Sci. U.S.A.* **30**, 244 (1944).
- [192] E. Caldeweyher, S. Ehlert, A. Hansen, H. Neugebauer, S. Spicher, C. Bannwarth, and S. Grimme, *J. Chem. Phys.* **150**, 154122 (2019).
- [193] A. Wang, S. Kadam, H. Li, S. Shi, and Y. Qi, *npj Comput. Mater.* **4**, 1 (2018).
- [194] J. Kim, B. M. Savoie, and T. F. Miller III, *J. Phys. Chem. C* **125**, 4614 (2021).
- [195] T. Verstraelen, P. Ayers, V. Van Speybroeck, and M. Waroquier, *J. Chem. Phys.* **138**, 074108 (2013).
- [196] C. G. Staacke, S. Wengert, C. Kunkel, G. Csányi, K. Reuter, and J. T. Margraf, *Mach. learn.: sci. technol.* **3**, 015032 (2022).
- [197] S. Patel and C. L. Brooks III, *J. Comput. Chem.* **25**, 1 (2004).
- [198] G. Lee Warren, J. E. Davis, and S. Patel, *J. Chem. Phys.* **128**, 144110 (2008).
- [199] J. Chen and T. J. Martínez, *Chem. Phys. Lett.* **438**, 315 (2007).
- [200] J. Morales and T. J. Martínez, *J. Phys. Chem. A* **108**, 3076 (2004).
- [201] A. Gao and R. C. Remsing, *Nat. Commun.* **13**, 1 (2022).
- [202] L. Zhang, H. Wang, M. C. Muniz, A. Z. Panagiotopoulos, R. Car, and W. E. J. *J. Chem. Phys.* **156**, 124107 (2022).
- [203] T. Zubatiuk, B. Nebgen, N. Lubbers, J. S. Smith, R. Zubatyuk, G. Zhou, C. Koh, K. Barros, O. Isayev, and S. Tretiak, *J. Chem. Phys.* **154**, 244108 (2021).
- [204] H. Li, C. Collins, M. Tanha, G. J. Gordon, and D. J. Yaron, *J. Chem. Theory Comput.* **14**, 5764 (2018).
- [205] Z. Qiao, M. Welborn, A. Anandkumar, F. R. Manby, and T. F. Miller III, *J. Chem. Phys.* **153**, 124111 (2020).
- [206] J. Hermann, Z. Schätzle, and F. Noé, *Nat. Chem.* **12**, 891 (2020).

# Appendix

## A.1 Symmetry Functions Used for Constructing Neural Network Potentials

**Tab. A.1:** Symmetry functions for  $C_{10}H_2/C_{10}H_3^+$ . Reprinted (adapted) with permission from Ref. [34]. Copyright 2021 Springer Nature.

type	atom $i$	atom $j$	atom $k$	$\eta(1/a_0^2)$	$\lambda$	$\zeta$	$R_c(a_0)$	$R_s(a_0)$
2	H	H		0.0			8.0	0.0
2	H	H		0.006			8.0	0.0
2	H	H		0.011			8.0	0.0
2	H	H		0.018			8.0	0.0
2	H	H		0.026			8.0	0.0
2	H	H		0.035			8.0	0.0
2	C	H		0.0			8.0	0.0
2	C	H		0.013			8.0	0.0
2	C	H		0.029			8.0	0.0
2	C	H		0.054			8.0	0.0
2	C	H		0.093			8.0	0.0
2	C	H		0.161			8.0	0.0
2	H	C		0.0			8.0	0.0
2	H	C		0.013			8.0	0.0
2	H	C		0.029			8.0	0.0
2	H	C		0.054			8.0	0.0
2	H	C		0.093			8.0	0.0
2	H	C		0.161			8.0	0.0
2	C	C		0.0			8.0	0.0
2	C	C		0.01			8.0	0.0
2	C	C		0.023			8.0	0.0
2	C	C		0.041			8.0	0.0
2	C	C		0.065			8.0	0.0
2	C	C		0.103			8.0	0.0
3	C	C	C	0.0	1.0	1.0	8.0	
3	C	C	C	0.0	1.0	2.0	8.0	

type	atom $i$	atom $j$	atom $k$	$\eta(1/a_0^2)$	$\lambda$	$\zeta$	$R_c(a_0)$	$R_s(a_0)$
3	C	C	C	0.0	1.0	4.0	8.0	
3	C	C	C	0.0	1.0	8.0	8.0	
3	C	C	C	0.0	-1.0	1.0	8.0	
3	C	C	C	0.0	-1.0	2.0	8.0	
3	C	C	C	0.0	-1.0	4.0	8.0	
3	C	C	C	0.0	-1.0	8.0	8.0	
3	C	H	H	0.0	1.0	1.0	8.0	
3	C	H	H	0.0	1.0	2.0	8.0	
3	C	H	H	0.0	1.0	4.0	8.0	
3	C	H	H	0.0	1.0	8.0	8.0	
3	C	H	H	0.0	-1.0	1.0	8.0	
3	C	H	H	0.0	-1.0	2.0	8.0	
3	C	H	H	0.0	-1.0	4.0	8.0	
3	C	H	H	0.0	-1.0	8.0	8.0	
3	C	C	H	0.0	1.0	1.0	8.0	
3	C	C	H	0.0	1.0	2.0	8.0	
3	C	C	H	0.0	1.0	4.0	8.0	
3	C	C	H	0.0	1.0	8.0	8.0	
3	C	C	H	0.0	-1.0	1.0	8.0	
3	C	C	H	0.0	-1.0	2.0	8.0	
3	C	C	H	0.0	-1.0	4.0	8.0	
3	C	C	H	0.0	-1.0	8.0	8.0	
3	H	C	C	0.0	1.0	1.0	8.0	
3	H	C	C	0.0	1.0	2.0	8.0	
3	H	C	C	0.0	1.0	4.0	8.0	
3	H	C	C	0.0	1.0	8.0	8.0	
3	H	C	C	0.0	-1.0	1.0	8.0	
3	H	C	C	0.0	-1.0	2.0	8.0	
3	H	H	C	0.0	1.0	1.0	8.0	
3	H	H	C	0.0	1.0	2.0	8.0	
3	H	H	C	0.0	1.0	4.0	8.0	
3	H	H	C	0.0	1.0	8.0	8.0	
3	H	H	C	0.0	-1.0	1.0	8.0	
3	H	H	C	0.0	-1.0	2.0	8.0	

**Tab. A.2:** Symmetry functions for  $\text{Ag}^+/\text{Ag}^-$  clusters. Reprinted (adapted) with permission from Ref. [34]. Copyright 2021 Springer Nature.

type	atom $i$	atom $j$	atom $k$	$\eta(1/a_0^2)$	$\lambda$	$\zeta$	$R_c(a_0)$	$R_s(a_0)$
2	Ag	Ag		0.0			10.0	0.0
2	Ag	Ag		0.007			10.0	0.0

type	atom $i$	atom $j$	atom $k$	$\eta(1/a_0^2)$	$\lambda$	$\zeta$	$R_c(a_0)$	$R_s(a_0)$
2	Ag	Ag		0.014			10.0	0.0
2	Ag	Ag		0.025			10.0	0.0
2	Ag	Ag		0.04			10.0	0.0
2	Ag	Ag		0.062			10.0	0.0
3	Ag	Ag	Ag	0.0	1.0	1.0	10.0	
3	Ag	Ag	Ag	0.0	1.0	2.0	10.0	
3	Ag	Ag	Ag	0.0	1.0	4.0	10.0	
3	Ag	Ag	Ag	0.0	1.0	8.0	10.0	
3	Ag	Ag	Ag	0.0	-1.0	1.0	10.0	
3	Ag	Ag	Ag	0.0	-1.0	2.0	10.0	

**Tab. A.3:** Symmetry functions for  $\text{Na}_8\text{Cl}_8^+/\text{Na}_9\text{Cl}_8^+$  clusters. Reprinted (adapted) with permission from Ref. [34]. Copyright 2021 Springer Nature.

type	atom $i$	atom $j$	atom $k$	$\eta(1/a_0^2)$	$\lambda$	$\zeta$	$R_c(a_0)$	$R_s(a_0)$
2	Na	Na		0.0			10.0	0.0
2	Na	Na		0.001			10.0	0.0
2	Na	Na		0.002			10.0	0.0
2	Na	Na		0.003			10.0	0.0
2	Na	Na		0.004			10.0	0.0
2	Na	Na		0.005			10.0	0.0
2	Na	Cl		0.0			10.0	0.0
2	Na	Cl		0.003			10.0	0.0
2	Na	Cl		0.005			10.0	0.0
2	Na	Cl		0.007			10.0	0.0
2	Na	Cl		0.01			10.0	0.0
2	Na	Cl		0.013			10.0	0.0
2	Cl	Na		0.0			10.0	0.0
2	Cl	Na		0.003			10.0	0.0
2	Cl	Na		0.005			10.0	0.0
2	Cl	Na		0.007			10.0	0.0
2	Cl	Na		0.01			10.0	0.0
2	Cl	Na		0.013			10.0	0.0
2	Cl	Cl		0.0			10.0	0.0
2	Cl	Cl		0.001			10.0	0.0
2	Cl	Cl		0.002			10.0	0.0
2	Cl	Cl		0.003			10.0	0.0
2	Cl	Cl		0.004			10.0	0.0
2	Cl	Cl		0.005			10.0	0.0
3	Na	Na	Cl	0.0	1.0	1.0	10.0	
3	Na	Na	Cl	0.0	1.0	2.0	10.0	

type	atom $i$	atom $j$	atom $k$	$\eta(1/a_0^2)$	$\lambda$	$\zeta$	$R_c(a_0)$	$R_s(a_0)$
3	Na	Na	Cl	0.0	1.0	4.0	10.0	
3	Na	Na	Cl	0.0	1.0	8.0	10.0	
3	Na	Na	Cl	0.0	-1.0	1.0	10.0	
3	Na	Na	Cl	0.0	-1.0	2.0	10.0	
3	Na	Cl	Cl	0.0	1.0	1.0	10.0	
3	Na	Cl	Cl	0.0	1.0	2.0	10.0	
3	Na	Cl	Cl	0.0	-1.0	1.0	10.0	
3	Na	Cl	Cl	0.0	-1.0	2.0	10.0	
3	Na	Cl	Cl	0.0	-1.0	4.0	10.0	
3	Cl	Cl	Na	0.0	1.0	1.0	10.0	
3	Cl	Cl	Na	0.0	1.0	2.0	10.0	
3	Cl	Cl	Na	0.0	1.0	4.0	10.0	
3	Cl	Cl	Na	0.0	1.0	8.0	10.0	
3	Cl	Cl	Na	0.0	-1.0	1.0	10.0	
3	Cl	Na	Na	0.0	1.0	1.0	10.0	
3	Cl	Na	Na	0.0	1.0	2.0	10.0	
3	Cl	Na	Na	0.0	1.0	4.0	10.0	
3	Cl	Na	Na	0.0	-1.0	1.0	10.0	
3	Cl	Na	Na	0.0	-1.0	2.0	10.0	

**Tab. A.4:** Symmetry functions for Au<sub>2</sub>-MgO slabs. Reprinted (adapted) with permission from Ref. [34]. Copyright 2021 Springer Nature.

type	atom $i$	atom $j$	atom $k$	$\eta(1/a_0^2)$	$\lambda$	$\zeta$	$R_c(a_0)$	$R_s(a_0)$
2	Mg	Mg		0.0			8.0	0.0
2	Mg	Mg		0.001			8.0	0.0
2	Mg	Mg		0.002			8.0	0.0
2	Mg	Mg		0.003			8.0	0.0
2	Mg	Mg		0.004			8.0	0.0
2	Mg	Mg		0.005			8.0	0.0
2	O	Mg		0.0			8.0	0.0
2	O	Mg		0.004			8.0	0.0
2	O	Mg		0.007			8.0	0.0
2	O	Mg		0.01			8.0	0.0
2	O	Mg		0.014			8.0	0.0
2	O	Mg		0.018			8.0	0.0
2	Mg	O		0.0			8.0	0.0
2	Mg	O		0.004			8.0	0.0
2	Mg	O		0.007			8.0	0.0
2	Mg	O		0.01			8.0	0.0
2	Mg	O		0.014			8.0	0.0

type	atom $i$	atom $j$	atom $k$	$\eta(1/a_0^2)$	$\lambda$	$\zeta$	$R_c(a_0)$	$R_s(a_0)$
2	Mg	O		0.018			8.0	0.0
2	O	O		0.0			8.0	0.0
2	O	O		0.001			8.0	0.0
2	O	O		0.002			8.0	0.0
2	O	O		0.003			8.0	0.0
2	O	O		0.004			8.0	0.0
2	O	O		0.005			8.0	0.0
2	Mg	Au		0.0			8.0	0.0
2	Mg	Au		0.001			8.0	0.0
2	Mg	Au		0.002			8.0	0.0
2	Mg	Au		0.003			8.0	0.0
2	Mg	Au		0.004			8.0	0.0
2	Mg	Au		0.005			8.0	0.0
2	Au	Mg		0.0			8.0	0.0
2	Au	Mg		0.001			8.0	0.0
2	Au	Mg		0.002			8.0	0.0
2	Au	Mg		0.003			8.0	0.0
2	Au	Mg		0.004			8.0	0.0
2	Au	Mg		0.005			8.0	0.0
2	Au	O		0.0			8.0	0.0
2	Au	O		0.004			8.0	0.0
2	Au	O		0.008			8.0	0.0
2	Au	O		0.013			8.0	0.0
2	Au	O		0.018			8.0	0.0
2	Au	O		0.024			8.0	0.0
2	Au	Au		0.0			8.0	0.0
2	Au	Au		0.004			8.0	0.0
2	Au	Au		0.008			8.0	0.0
2	Au	Au		0.012			8.0	0.0
2	Au	Au		0.017			8.0	0.0
2	Au	Au		0.022			8.0	0.0
2	O	Al		0.0			8.0	0.0
2	O	Al		0.003			8.0	0.0
2	O	Al		0.005			8.0	0.0
2	O	Al		0.008			8.0	0.0
2	O	Al		0.011			8.0	0.0
2	O	Al		0.014			8.0	0.0
2	Al	O		0.0			8.0	0.0
2	Al	O		0.003			8.0	0.0
2	Al	O		0.005			8.0	0.0
2	Al	O		0.008			8.0	0.0
2	Al	O		0.011			8.0	0.0

type	atom $i$	atom $j$	atom $k$	$\eta(1/a_0^2)$	$\lambda$	$\zeta$	$R_c(a_0)$	$R_s(a_0)$
2	Al	O		0.014			8.0	0.0
2	Al	Mg		0.0			8.0	0.0
2	Al	Mg		0.001			8.0	0.0
2	Al	Mg		0.002			8.0	0.0
2	Al	Mg		0.003			8.0	0.0
2	Al	Mg		0.004			8.0	0.0
2	Al	Mg		0.005			8.0	0.0
2	Mg	Al		0.0			8.0	0.0
2	Mg	Al		0.001			8.0	0.0
2	Mg	Al		0.002			8.0	0.0
2	Mg	Al		0.003			8.0	0.0
2	Mg	Al		0.004			8.0	0.0
2	Mg	Al		0.005			8.0	0.0
3	Mg	Mg	Mg	0.0	1.0	1.0	8.0	
3	Mg	Mg	Mg	0.0	1.0	2.0	8.0	
3	Mg	Mg	Mg	0.0	1.0	4.0	8.0	
3	Mg	Mg	Mg	0.0	-1.0	1.0	8.0	
3	Mg	Mg	O	0.0	1.0	1.0	8.0	
3	Mg	Mg	O	0.0	1.0	2.0	8.0	
3	Mg	Mg	O	0.0	1.0	4.0	8.0	
3	Mg	Mg	O	0.0	1.0	8.0	8.0	
3	Mg	Mg	O	0.0	-1.0	1.0	8.0	
3	Mg	Mg	O	0.0	-1.0	2.0	8.0	
3	Mg	O	O	0.0	1.0	1.0	8.0	
3	Mg	O	O	0.0	1.0	2.0	8.0	
3	Mg	O	O	0.0	1.0	4.0	8.0	
3	Mg	O	O	0.0	-1.0	1.0	8.0	
3	Mg	O	O	0.0	-1.0	2.0	8.0	
3	Mg	O	O	0.0	-1.0	4.0	8.0	
3	Mg	O	Al	0.0	1.0	1.0	8.0	
3	Mg	O	Al	0.0	1.0	2.0	8.0	
3	Mg	O	Al	0.0	1.0	4.0	8.0	
3	Mg	O	Al	0.0	1.0	8.0	8.0	
3	Mg	O	Al	0.0	-1.0	1.0	8.0	
3	Mg	O	Au	0.0	1.0	1.0	8.0	
3	Mg	O	Au	0.0	1.0	2.0	8.0	
3	Mg	O	Au	0.0	1.0	4.0	8.0	
3	Mg	O	Au	0.0	1.0	8.0	8.0	
3	Mg	O	Au	0.0	-1.0	1.0	8.0	
3	Mg	O	Au	0.0	-1.0	2.0	8.0	
3	O	Mg	Mg	0.0	1.0	1.0	8.0	
3	O	Mg	Mg	0.0	1.0	2.0	8.0	

type	atom $i$	atom $j$	atom $k$	$\eta(1/a_0^2)$	$\lambda$	$\zeta$	$R_c(a_0)$	$R_s(a_0)$
3	O	Mg	Mg	0.0	1.0	4.0	8.0	
3	O	Mg	Mg	0.0	-1.0	1.0	8.0	
3	O	Mg	Mg	0.0	-1.0	2.0	8.0	
3	O	Mg	Mg	0.0	-1.0	4.0	8.0	
3	O	Mg	O	0.0	1.0	1.0	8.0	
3	O	Mg	O	0.0	1.0	2.0	8.0	
3	O	Mg	O	0.0	1.0	4.0	8.0	
3	O	Mg	O	0.0	1.0	8.0	8.0	
3	O	Mg	O	0.0	-1.0	1.0	8.0	
3	O	Mg	O	0.0	-1.0	2.0	8.0	
3	O	Mg	Al	0.0	1.0	1.0	8.0	
3	O	Mg	Al	0.0	1.0	2.0	8.0	
3	O	Mg	Al	0.0	1.0	4.0	8.0	
3	O	Mg	Al	0.0	-1.0	1.0	8.0	
3	O	Mg	Al	0.0	-1.0	2.0	8.0	
3	O	Mg	Al	0.0	-1.0	4.0	8.0	
3	O	Mg	Au	0.0	1.0	1.0	8.0	
3	O	Mg	Au	0.0	1.0	2.0	8.0	
3	O	Mg	Au	0.0	-1.0	1.0	8.0	
3	O	Mg	Au	0.0	-1.0	2.0	8.0	
3	O	O	O	0.0	1.0	1.0	8.0	
3	O	O	O	0.0	1.0	2.0	8.0	
3	O	O	O	0.0	-1.0	1.0	8.0	
3	O	O	Al	0.0	1.0	1.0	8.0	
3	O	O	Al	0.0	1.0	2.0	8.0	
3	O	O	Al	0.0	-1.0	1.0	8.0	
3	O	O	Al	0.0	-1.0	2.0	8.0	
3	Al	Mg	Mg	0.0	1.0	1.0	8.0	
3	Al	Mg	O	0.0	1.0	1.0	8.0	
3	Al	Mg	O	0.0	1.0	2.0	8.0	
3	Al	Mg	O	0.0	-1.0	1.0	8.0	
3	Al	O	O	0.0	1.0	1.0	8.0	
3	Al	O	O	0.0	1.0	2.0	8.0	
3	Al	O	O	0.0	-1.0	1.0	8.0	
3	Al	O	O	0.0	-1.0	2.0	8.0	
3	Au	Mg	Mg	0.0	1.0	1.0	8.0	
3	Au	Mg	Mg	0.0	1.0	2.0	8.0	
3	Au	Mg	O	0.0	1.0	1.0	8.0	
3	Au	Mg	O	0.0	1.0	2.0	8.0	
3	Au	Mg	O	0.0	-1.0	1.0	8.0	
3	Au	Mg	O	0.0	-1.0	2.0	8.0	
3	Au	O	O	0.0	1.0	1.0	8.0	

type	atom $i$	atom $j$	atom $k$	$\eta(1/a_0^2)$	$\lambda$	$\zeta$	$R_c(a_0)$	$R_s(a_0)$
3	Au	O	Au	0.0	1.0	-1.0	8.0	
3	Au	O	Au	0.0	1.0	-2.0	8.0	

**Tab. A.5:** Symmetry functions for NaCl clusters

type	atom $i$	atom $j$	atom $k$	$\eta(1/a_0^2)$	$\lambda$	$\zeta$	$R_c(a_0)$	$R_s(a_0)$
2	Na	Na		0.0			12.0	0.0
2	Na	Na		0.003			12.0	0.0
2	Na	Na		0.005			12.0	0.0
2	Na	Na		0.008			12.0	0.0
2	Na	Na		0.012			12.0	0.0
2	Na	Na		0.016			12.0	0.0
2	Na	Cl		0.0			12.0	0.0
2	Na	Cl		0.004			12.0	0.0
2	Na	Cl		0.008			12.0	0.0
2	Na	Cl		0.013			12.0	0.0
2	Na	Cl		0.019			12.0	0.0
2	Na	Cl		0.028			12.0	0.0
2	Cl	Na		0.0			12.0	0.0
2	Cl	Na		0.004			12.0	0.0
2	Cl	Na		0.008			12.0	0.0
2	Cl	Na		0.013			12.0	0.0
2	Cl	Na		0.019			12.0	0.0
2	Cl	Na		0.028			12.0	0.0
2	Cl	Cl		0.0			12.0	0.0
2	Cl	Cl		0.003			12.0	0.0
2	Cl	Cl		0.006			12.0	0.0
2	Cl	Cl		0.009			12.0	0.0
2	Cl	Cl		0.013			12.0	0.0
2	Cl	Cl		0.017			12.0	0.0
3	Na	Na	Cl	0.0	1.0	1.0	12.0	
3	Na	Na	Cl	0.0	1.0	2.0	12.0	
3	Na	Na	Cl	0.0	1.0	4.0	12.0	
3	Na	Na	Cl	0.0	1.0	8.0	12.0	
3	Na	Na	Cl	0.0	-1.0	1.0	12.0	
3	Na	Na	Cl	0.0	-1.0	2.0	12.0	
3	Na	Na	Cl	0.0	-1.0	4.0	12.0	
3	Na	Na	Cl	0.0	-1.0	8.0	12.0	
3	Na	Na	Na	0.0	1.0	1.0	12.0	
3	Na	Na	Na	0.0	1.0	2.0	12.0	
3	Na	Na	Na	0.0	1.0	4.0	12.0	

type	atom $i$	atom $j$	atom $k$	$\eta(1/a_0^2)$	$\lambda$	$\zeta$	$R_c(a_0)$	$R_s(a_0)$
3	Na	Na	Na	0.0	1.0	8.0	12.0	
3	Na	Na	Na	0.0	-1.0	1.0	12.0	
3	Na	Na	Na	0.0	-1.0	2.0	12.0	
3	Na	Na	Na	0.0	-1.0	4.0	12.0	
3	Na	Cl	Cl	0.0	1.0	1.0	12.0	
3	Na	Cl	Cl	0.0	1.0	2.0	12.0	
3	Na	Cl	Cl	0.0	1.0	4.0	12.0	
3	Na	Cl	Cl	0.0	1.0	8.0	12.0	
3	Na	Cl	Cl	0.0	-1.0	1.0	12.0	
3	Na	Cl	Cl	0.0	-1.0	2.0	12.0	
3	Na	Cl	Cl	0.0	-1.0	4.0	12.0	
3	Na	Cl	Cl	0.0	-1.0	8.0	12.0	
3	Cl	Cl	Cl	0.0	1.0	1.0	12.0	
3	Cl	Cl	Cl	0.0	1.0	2.0	12.0	
3	Cl	Cl	Cl	0.0	1.0	4.0	12.0	
3	Cl	Cl	Cl	0.0	1.0	8.0	12.0	
3	Cl	Cl	Cl	0.0	-1.0	1.0	12.0	
3	Cl	Cl	Cl	0.0	-1.0	2.0	12.0	
3	Cl	Cl	Cl	0.0	-1.0	4.0	12.0	
3	Cl	Cl	Na	0.0	1.0	1.0	12.0	
3	Cl	Cl	Na	0.0	1.0	2.0	12.0	
3	Cl	Cl	Na	0.0	1.0	4.0	12.0	
3	Cl	Cl	Na	0.0	1.0	8.0	12.0	
3	Cl	Cl	Na	0.0	-1.0	1.0	12.0	
3	Cl	Cl	Na	0.0	-1.0	2.0	12.0	
3	Cl	Cl	Na	0.0	-1.0	4.0	12.0	
3	Cl	Cl	Na	0.0	-1.0	8.0	12.0	
3	Cl	Na	Na	0.0	1.0	1.0	12.0	
3	Cl	Na	Na	0.0	1.0	2.0	12.0	
3	Cl	Na	Na	0.0	1.0	4.0	12.0	
3	Cl	Na	Na	0.0	1.0	8.0	12.0	
3	Cl	Na	Na	0.0	-1.0	1.0	12.0	
3	Cl	Na	Na	0.0	-1.0	2.0	12.0	
3	Cl	Na	Na	0.0	-1.0	4.0	12.0	
3	Cl	Na	Na	0.0	-1.0	8.0	12.0	

## A.2 Learning Curves of HDNNPs

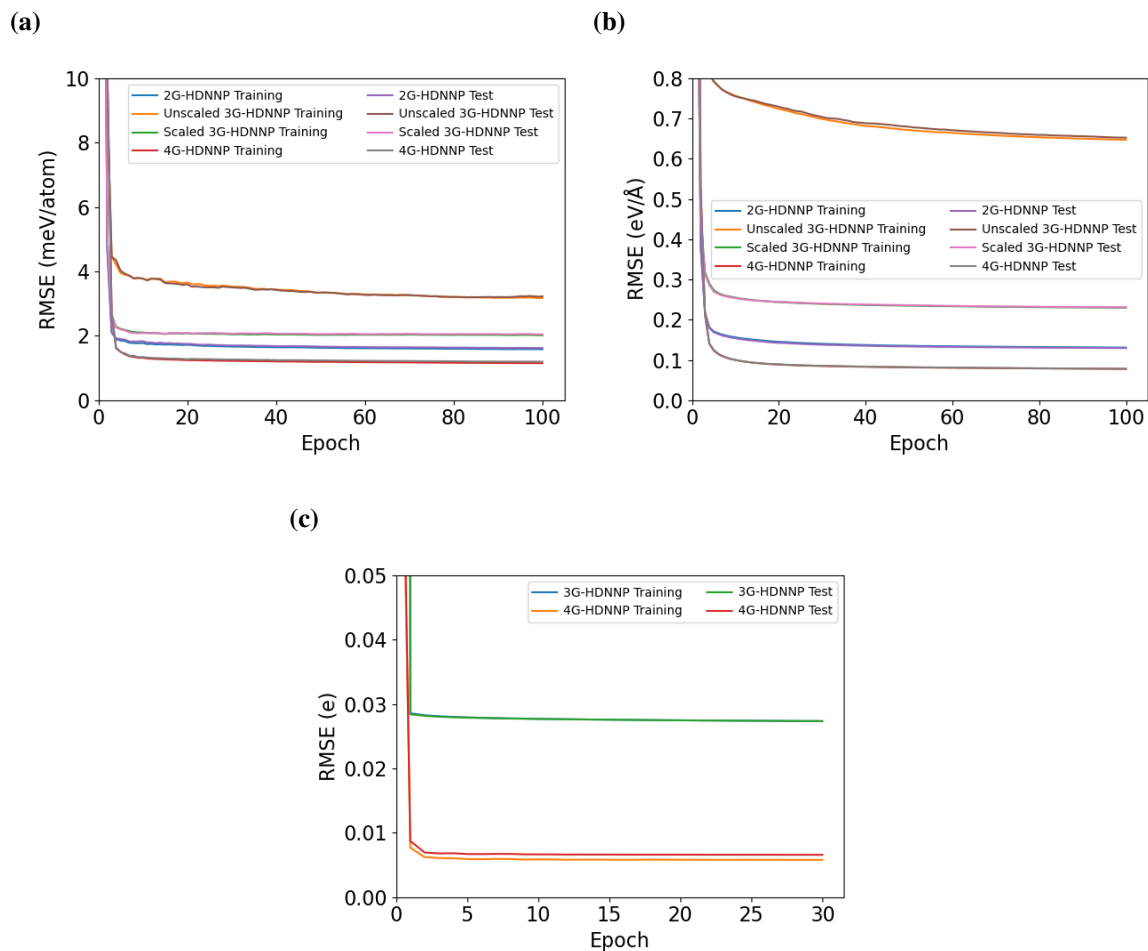


**Fig. A.2:** Training and test error of binding energies (a), force components (b) and atomic charges (c) during the training of different generations of HDNNPs for  $C_{10}H_2/C_{10}H_3^+$ .

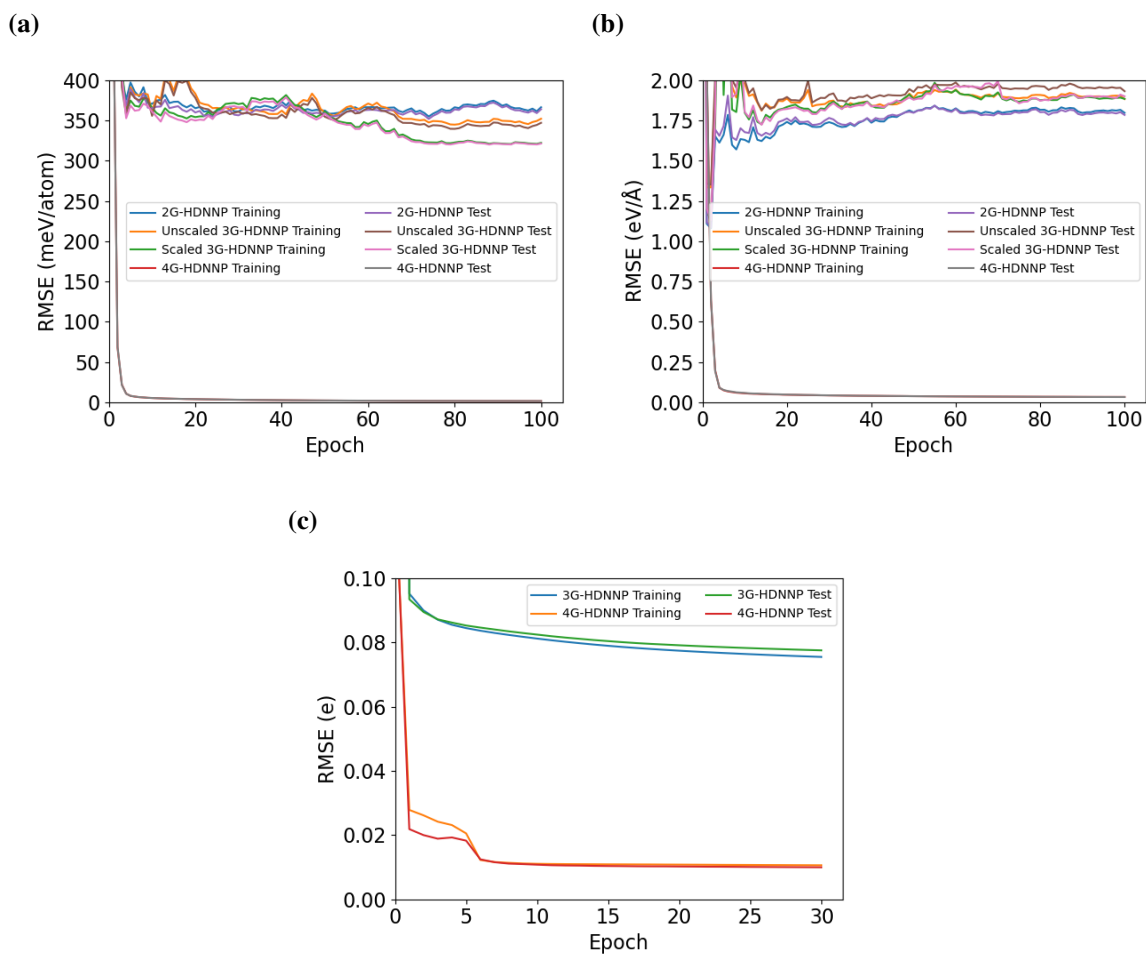


**Fig. A.3:** Training and test error of binding energies (a), force components (b) and atomic charges (c) during the training of different generations of HDNNPs for  $\text{Ag}_3^+/\text{Ag}_3^-$ .

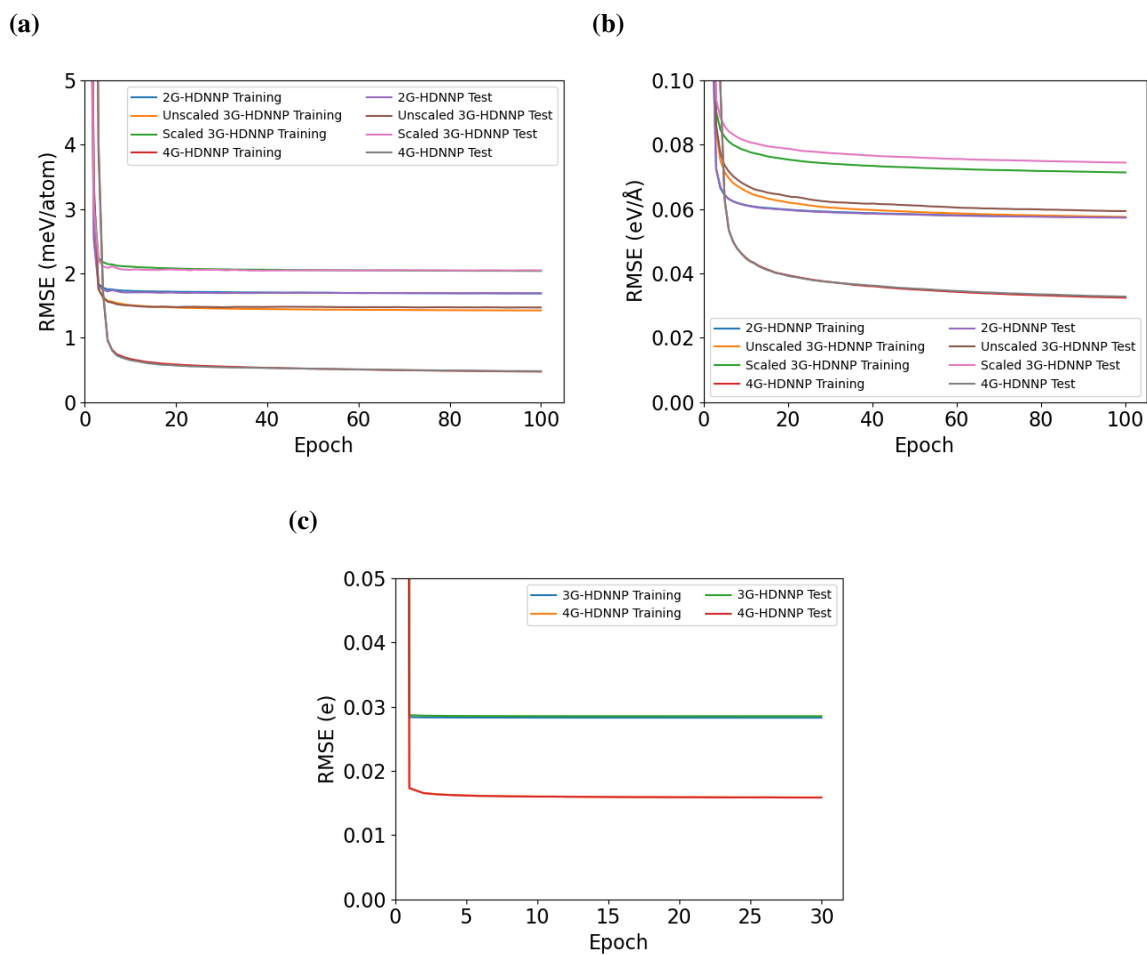


**Fig. A.4:** Training and test error of binding energies (a), force components (b) and atomic charges (c) during the training of different generations of HDNNPs for  $\text{Na}_8\text{Cl}_8^+/\text{Na}_9\text{Cl}_8^+$ .

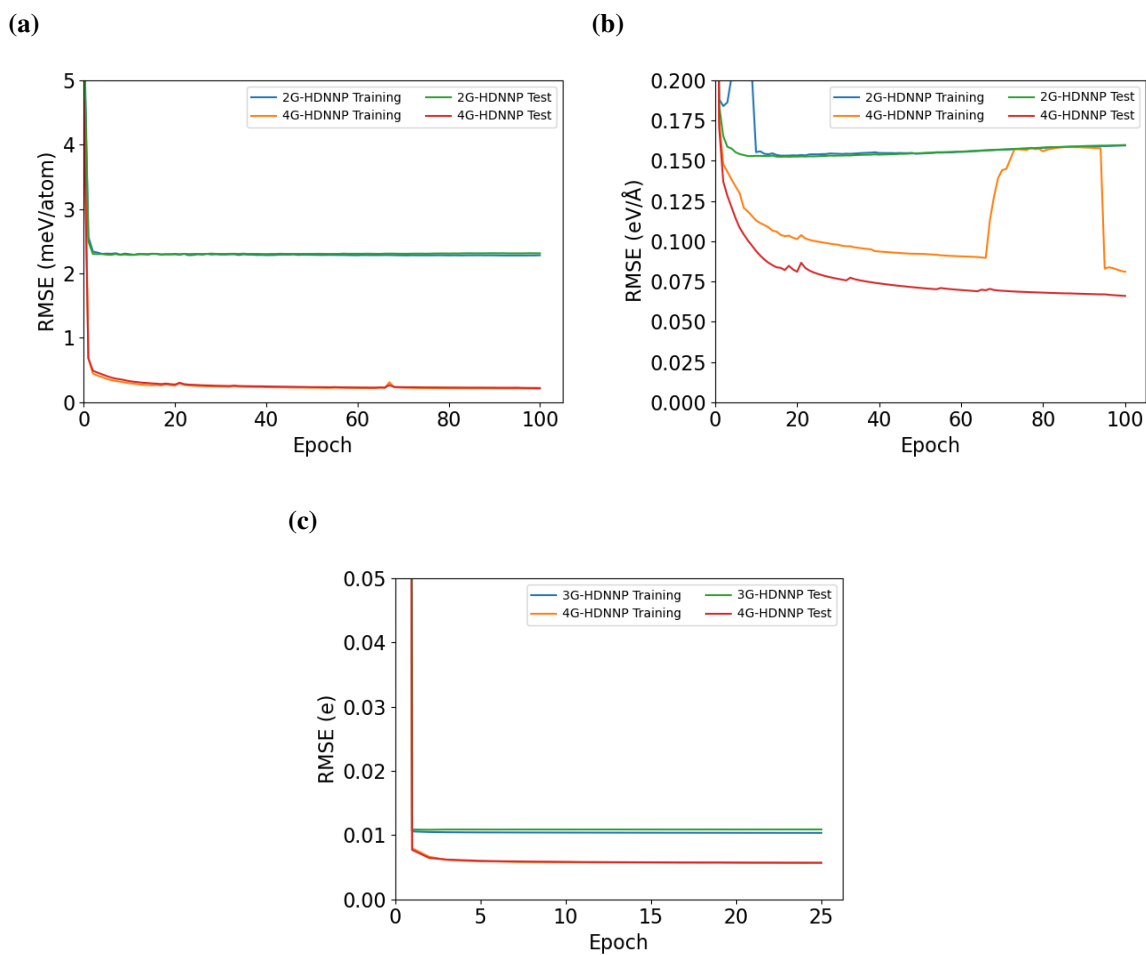


**Fig. A.5:** Training and test error of binding energies (a), force components (b) and atomic charges (c) during the training of different generations of HDNNPs for Au<sub>2</sub>-MgO.

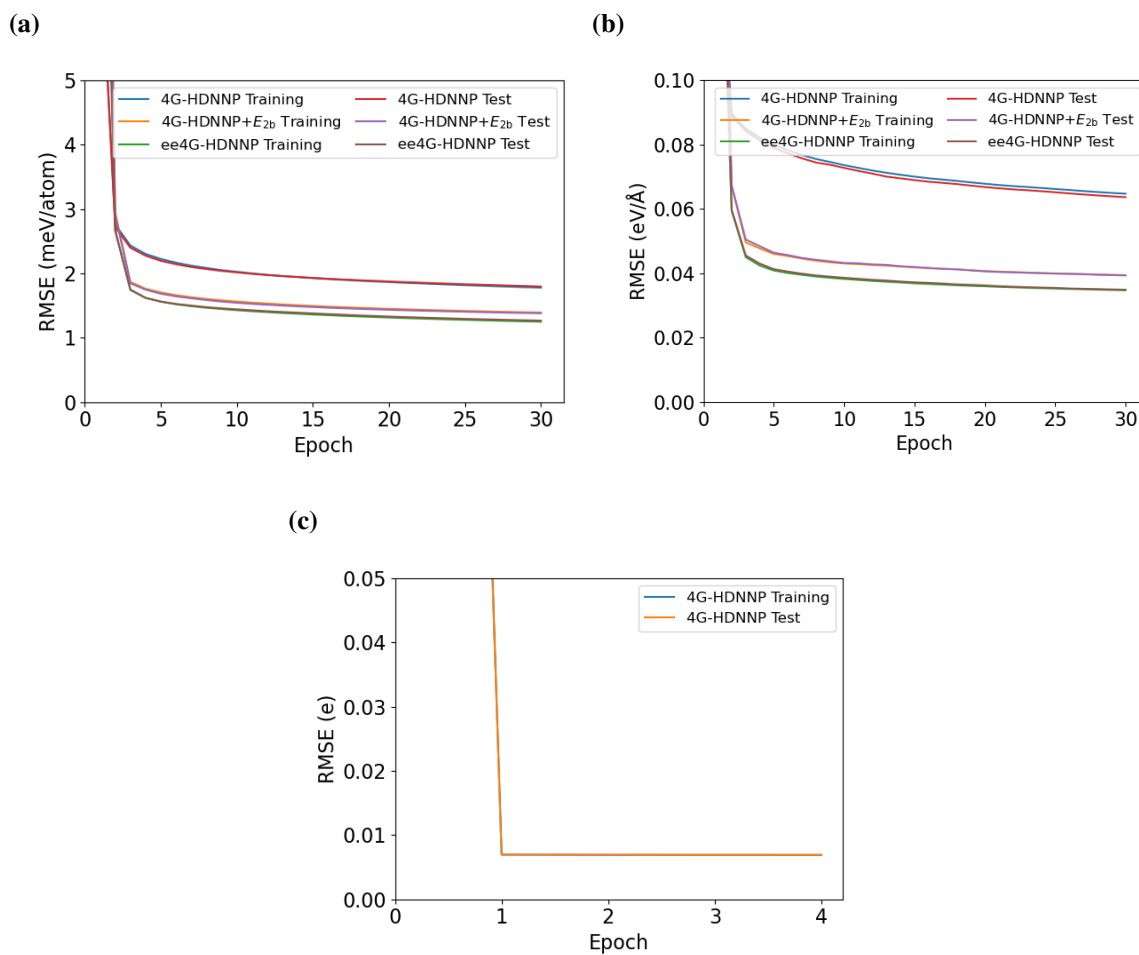


**Fig. A.6:** Training and test error of binding energies (a), force components (b) and atomic charges (c) during the training of different generations of HDNNPs for NaCl clusters.

## A.3 Two-Body Potentials of Dimers for Sodium Chloride

The fitting of the two-body potentials in eq. 5.2 for the construction of ee4G-HDNNP and 4G-HDNNP+ $E_{2b}$  was performed using Python (version: 3.7.11) with the SciPy (version: 1.6.2) library. The reference DFT dissociation curve of a neutral dimer was generated by evenly sampling from 2.94 to 11.23 Bohr with a stepsize of 0.105 Bohr. The fitted two-body potentials and DFT reference curves are plotted in Fig. A.7 and the corresponding parameters are reported in Tab. A.6. It is noted that the pairwise interaction energy between Na and Cl is trained to the difference between DFT total energy and Coulomb energy  $E_{elec}$ .

**Tab. A.6:** Parameters of the two-body potentials for the construction of 4G-HDNNP+ $E_{2b}$  and ee4G-HDNNP.

pair	A [Ha]	B [1/Bohr]	$\mu$ [Bohr]	C [Ha Bohr <sup>6</sup> ]	D [Ha Bohr <sup>8</sup> ]
Na-Na	2.997	1.860	3.379	4276.635	0.0
Na-Cl	1.778	1.293	2.529	0.0	0.0
Cl-Cl	1.713	2.106	3.624	4592.649	0.0

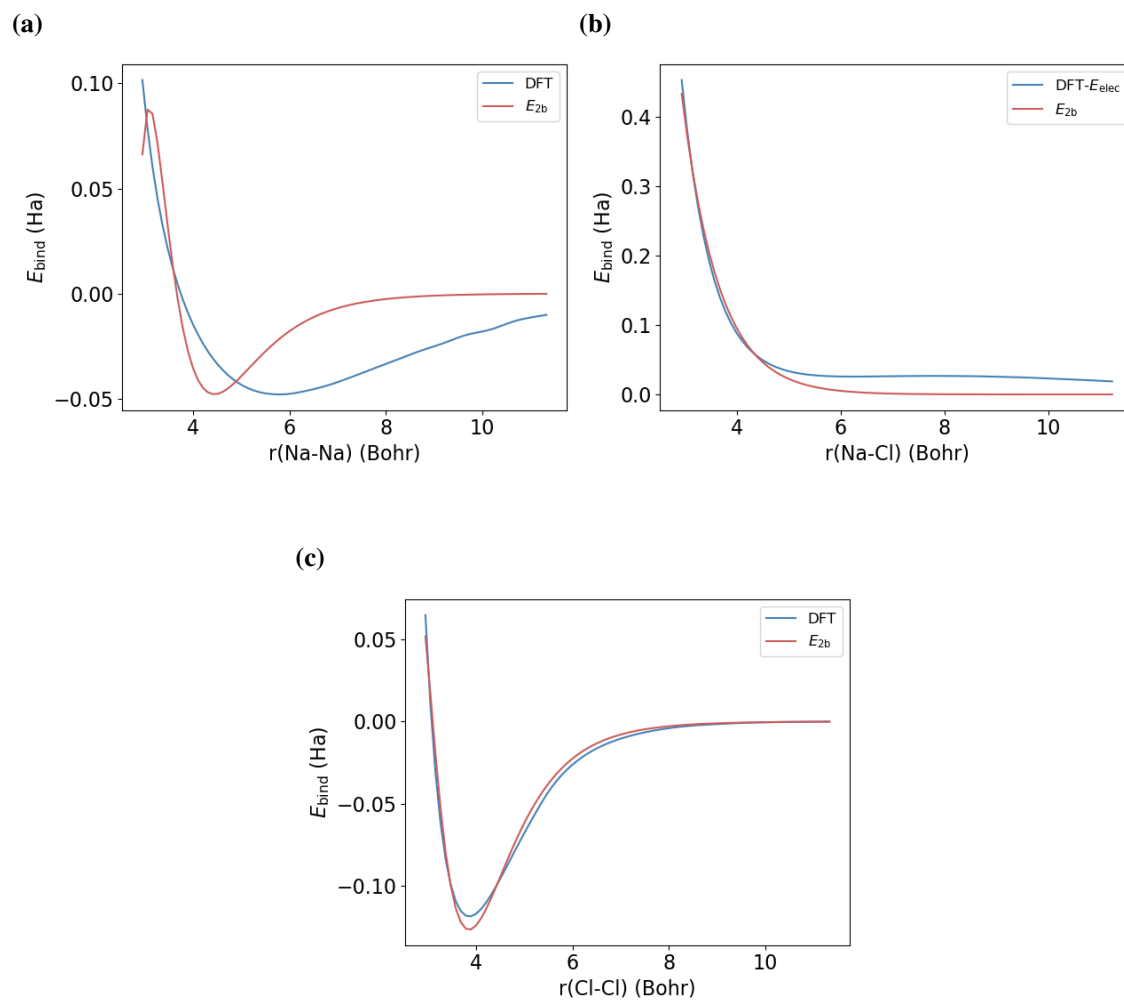


**Fig. A.7:** Binding energy curves of Na-Na (a), Na-Cl (b) and Cl-Cl (c) predicted by DFT and two-body potentials in 4G-HDNNP+ $E_{2b}$  and ee4G-HDNNP. The binding energy of Na-Cl is trained to the remaining part after removing the Coulomb energy  $E_{\text{elec}}$  from DFT energy.